# BRNO UNIVERSITY OF TECHNOLOGY
VYSOKÉ UČENÍ TECHNICKÉ V BRNĚ

## FACULTY OF MECHANICAL ENGINEERING
FAKULTA STROJNÍHO INŽENÝRSTVÍ

## INSTITUTE OF PHYSICAL ENGINEERING
ÚSTAV FYZIKÁLNÍHO INŽENÝRSTVÍ

## CORRELATION AND SPIRAL MICROSCOPY USING A SPATIAL LIGHT MODULATION
KORELAČNÍ A SPIRÁLNÍ MIKROSKOPIE S PROSTOROVOU MODULACÍ SVĚTLA

**DOCTORAL THESIS**
DIZERTAČNÍ PRÁCE

**AUTHOR**                     Ing. Petr Bouchal
AUTOR PRÁCE

**SUPERVISOR**             prof. RNDr. Jiří Petráček, Dr.
ŠKOLITEL

**BRNO 2016**

**Abstract**

The doctoral thesis presents a review of the main research results obtained in the course of doctoral studies. In the introductory part, the motivation and technical support for the planned research are discussed in connection with research activities of the group of Experimental Biophotonics at the Institute of Physical Engineering, Brno University of Technology.

The scientific part of the doctoral thesis is divided into two main parts devoted to new imaging concepts and modifications of current experiments to extend their application potential. Achieved results support the research development in the areas of correlation and spiral microscopy, utilizing a spatial light modulation as a key experimental technique. Among the new imaging concepts, the correlation imaging is examined under conditions of partial spatial and temporal coherence of light. Subsequently, the principles of singular optics and nondiffracting propagation of light are advantageously implemented in correlation, holographic and optical microscopy, resulting in advanced imaging techniques and holographic reconstructions. Specifically, the vortex and nondiffracting beams and the self-imaging effects are successfully deployed using either optical or digital tools and gradually applied to 3D spiral imaging ensuring the edge contrast enhancement or axial localization of microobjects by the rotating point spread function. The results obtained by the theoretical analysis and the experimental testing of the proposed imaging modalities are also presented.

In the technical part of the doctoral thesis, up-to-date imaging configurations aided by a spatial light modulator are optimized, allowing the wide-field correlation imaging and achromatic high-resolution imaging by a programmable diffractive lens. In the correlation imaging, the enhanced field of view is achieved by deploying a relay optical system in standard experiments, while achromatic correction of diffractive lenses is implemented by a specially designed refractive corrector. Using birefringence of liquid crystal molecules of light modulating devices, a new phase-shifting technique is proposed and tested in polarization adapted Mirau interferometer. Acquired experimental know-how is fully exploited in the design of multimodal microscope working with different imaging modes implemented using an add-on module connected to standard microscope.

## Abstrakt

Dizertační práce je uceleným shrnutím výsledků dosažených v průběhu doktorského studia. V úvodní části práce je představena motivace, odborné a technické zázemí a grantová podpora realizovaného výzkumu. Popsány jsou také dosažené výsledky a jejich význam pro skupinu Experimentální biofotoniky, Ústavu fyzikálního inženýrství, Vysokého učení technického v Brně.

Vědecká část práce je rozdělena do dvou hlavních bloků, které se postupně zabývají návrhem nových zobrazovacích koncepcí a technickou modifikací stávajících zobrazovacích systému v praktických aplikacích. Dosažené vědecké výsledky podporují vývoj v oblastech korelační a spirální mikroskopie s prostorovou modulací světla.

V části zabývající se návrhem nových zobrazovacích koncepcí je provedena studie korelačního zobrazení v podmínkách proměnné časové a prostorové koherence. Následně jsou zkoumány možnosti praktického využití vírových a nedifrakčních svazků v oblastech korelační, holografické a optické mikroskopie. Interference vírových svazků a samozobrazení nedifrakčních svazků je postupně využito k dosažení 3D zobrazení s hranovým kontrastem a rotující bodovou rozptylovou funkcí. Pokročilé zobrazovací metody jsou úspěšně zavedeny optickou cestou ale i digitální modifikací holografických záznamů. Výsledky teoretických modelů a numerických simulací jsou doprovázeny praktickým vyhodnocením navržených zobrazovacích principů.

V technicky zaměřené části jsou navrženy nové způsoby zavedení prostorové modulace světla, které umožňují rozšíření zorného pole v experimentech korelačního zobrazení a dosažení achromatizace při zobrazení pomocí programovatelných difraktivních prvků. Rozšíření zorného pole v korelačních experimentech umožňuje přizpůsobovací optický systém vložený do standardní zobrazovací sestavy. Achromatizace difraktivního zobrazení je zajištěna použitím speciálně navrženého refraktivního korektoru. V navazující části je navržena nová metoda krokování fáze, která pracuje s dvojlomností kapalných krystalů využívaných v systémech pro prostorovou modulaci světla. Použití metody je experimentálně demonstrováno v polarizačně modifikovaném Mirau interferometru. Získané technické zkušenosti jsou využity v praktickém návrhu a realizaci multimodálního zobrazovacího systému s prostorovou modulací světla.

**Keywords**

digital holography, correlation and spiral microscopy, spatial light modulation, vortex and nondiffracting beams, three-dimensional and quantitative imaging

**Klíčová slova**

digitální holografie, korelační a spirální mikroskopie, prostorová modulace světla, vírové a nedifrakční svazky, trojrozměrné a kvantitativní zobrazení

**Bibliographic citation**

BOUCHAL, P. *Correlation and spiral microscopy using a spatial light modulation.* Brno: Brno University of Technology, Faculty of Mechanical Engineering, 1–74, 2016. Supervisor: prof. RNDr. Jiří Petráček, Dr.

I declare that this thesis has been composed by myself under the guidance of my supervisor and that it has not been submitted, in whole or in part, in any previous application for a degree. Any secondary sources and contributions from colleagues in the collaboration are explicitly referenced in the text.

<div align="right">

. . . . . . . . . . . . . . . . . . . .

Petr Bouchal

</div>

**Acknowledgements**

x

# Contents

# 1. Topics and meaning of the doctoral thesis

The doctoral thesis is focused on advanced imaging techniques that connect theoretical concepts of traditional and modern optics with methods of digital signal processing and optoelectronic light shaping technologies. The developed imaging techniques are based on the principles of diffractive optics, Fourier optics and digital holography, which are further supported by nondiffracting and self-imaging phenomena [1–3] and recent discoveries in singular optics [4]. The proposed and realized imaging methods operate with the intentionally created nondiffracting and vortex beams enabling specific experiments on image contrast enhancement, quantitative phase imaging or axial localization of microobjects. As a basic experimental tool, a liquid crystal on silicon Spatial Light Modulator (SLM) has been used to create the special states of light and to modify the spatial spectrum of optical signal. The doctoral thesis has been built on the foundations previously established in the bachelor and diploma thesis [5,6]. Its main goal is to deepen the theoretical and experimental background of the SLM aided imaging and to propose original applications of the SLM technology in fluorescence microscopy, spiral microscopy, incoherent correlation holography, quantitative phase imaging and 3D localization of microscopic objects. The topics developed in the doctoral thesis are closely related to the traditional research established at the Institute of Physical Engineering, the Faculty of Mechanical Engineering, Brno University of Technology (IPE BUT). Specifically, the experiments realized in the doctoral thesis provide support and new ideas for Coherence Controlled Holographic Microscopy (CCHM) [7], that has been invented at the IPE BUT and its applications have permanently emerged at the forefront of a systematic biomedical research [8–10]. When implementing novel experiments of the SLM aided microscopy, an effective cooperation between the IPE BUT and the Department of Optics of the Palacky University in Olomouc (UP) has been established, benefiting from specific know-how of both institutions developed in the fields of holographic microscopy and light shaping technology, respectively. Topicality and interdisciplinary impact of the SLM imaging initiated a joint research programme of both institutions, which became a part of the Center of Digital Optics (CDO) supported by the Technology Agency of the Czech Republic (TA CR). The CDO has been established for a period of eight years and currently it represents a well–functioning Center of excellence with the participation of two academic institutions (IPE BUT and UP) and three major companies operating in the area of Moravia (Meopta-optika, s.r.o., PRAMACOM-HT, s r.o. and ZEBR, s.r.o. ). The methods developed throughout the doctoral thesis formed a basis for one of four CDO working packages, called *"Imaging supported by a spatial light modulation."* Outcomes of the doctoral thesis were used not only in the applied research but they also positively influenced a cooperation of the IPE BUT and the UP in the field of basic research. The research activities resulted in the joint project *"Advances in incoherent holographic microscopy using photonic modeling and principles of singular optics"*, supported by the Grant Agency of the Czech Republic (GA CR). Receiving support from the projects of TA CR and GA CR, a new laboratory has been equipped at the IPE BUT, allowing for the cutting-edge experiments in the field of SLM microscopy [11].

The doctoral thesis is divided into three distinctive parts providing an overview of the current state of the art in the field of SLM imaging and presenting the main outcomes of both basic and applied research. In the first part, basic principles and experimental aspects of the SLM technology are discussed and applications in the optical and holo-

graphic microscopy and the incoherent correlation imaging outlined. In further parts, the concepts and experiments are specified having a significant impact on the research carried out in the doctoral thesis. The elaborated imaging techniques have been selected taking into account a complexity of experiments, technical means of the phase modulation and overall benefits of the SLM technology in optical microscopy and incoherent correlation holography. The particular attention has been paid to the Fresnel incoherent correlation holography and the conceptual and technical modifications of this method. As important outcomes of the research, the basic and advanced models of the incoherent correlation imaging operating with a monochromatic or broadband light were proposed and elaborated. Interest has also been focused on the utilization of vortex and nondiffracting beams in the experimental techniques of microscopy. Within an applied research, the experiments based on the special beams and the self-imaging phenomenon have been successfully used for a selective edge contrast enhancement and a precise axial localization of microscopic objects. In the final part of the doctoral thesis, new technical improvements of the experiments are presented providing an increased optical performance of the imaging methods investigated. In the incoherent correlation imaging, the modified experiments using relay lenses were designed resulting in a perfect overlapping of interfering waves and a significant extension of the field of view. To support the SLM operation in lens-like applications using a broadband light, a refractive afocal optical system was designed and realized, enabling an achromatic correction of the diffractive dispersion. To develop novel techniques of the quantitative phase imaging, birefringent properties of the liquid crystal devices were tested. The polarization sensitive Mirau interferometry was proposed using all-optical motionless phase-shifting by a liquid crystal variable retarder. As a result of applied research, a versatile microscope controlled by the SLM was designed, whose concept was tested using the methods examined throughout the doctoral thesis.

# 2. Objectives and main outcomes

The doctoral thesis is focused on the advanced imaging methods benefiting from connections between recent discoveries of modern optics and sophisticated techniques for light shaping and signal processing. Due to the ongoing technological progress, a powerful experimental background has been created in the SLM aided digital imaging, that has opened new pathways for systematic research with a wide range of applications. The predetermined research plans of the doctoral thesis can be specified as follows:

- Creation of computational models of the incoherent correlation holography describing a two-step image formation and allowing to examine an influence of the partial temporal coherence of light and the diffractive dispersion.

- Design and implementation of the original experimental configurations for the SLM aided common-path interferometry, working with both coherent and spatially incoherent light.

- Incorporation of nondiffracting and vortex beams, self-imaging phenomena and principles of singular optics into the advanced imaging techniques of optical microscopy and digital holography.

- Implementation of new experiments of the quantitative phase imaging using the SLM as an active element and the development of efficient techniques for the point spread function (PSF) engineering.

- Optimization of the developed imaging techniques to design the functional prototype of a versatile microscope implemented by commercially available and customized optical components.

The doctoral thesis succeeded in meeting the challenges outlined and the original concepts and experiments for the SLM aided imaging were designed and implemented. As a basic imaging technique, the common-path incoherent correlation microscopy using the SLM as a diffractive beam splitter was examined both theoretically and experimentally. The experimental setup was modeled mathematically using the paraxial approximation of wave optics, and the optical performance and the resolution limits of the imaging were determined assuming a monochromatic spatially incoherent light [13]. For a broadband light illumination, a concept of the coherence induced aperture was proposed to analyze a comprehensive impact of experimental parameters, temporal coherence of light and diffractive dispersion on the achievable image resolution [14,15]. A hybrid coherence mode of the correlation imaging, explored in [13], was originally combined with spiral phase singularities of light to realize a selective edge contrast enhancement in three-dimensional incoherent vortex imaging [16]. Based on the research of the vortex and nondiffracting beams, new techniques of the axial localization of microscopic objects were developed and advantageously adapted to the imaging methods of digital holographic microscopy [17,18]. Using interference of the nondiffracting beams, the self-imaging phenomena were deployed in the axial localization of microparticles in imaging methods of optical microscopy. As the main advantage of the methods, the aberration resistance was studied and demonstrated experimentally [19,20].

Beyond the planned research devoted to the SLM aided imaging, the techniques of the quantitative phase imaging based on a polarization sensitive phase-shifting were also

developed. Research in this field resulted in the experiment, which represents a polarization modification of Mirau interferometry. The quantitative phase reconstruction was performed by a birefringent Liquid Crystal Variable Retarder (LCVR) ensuring an anisotropic phase-shifting of the orthogonally polarized beams [21]. The accuracy of the optical path difference reconstruction, achieved in experiments, was better than 1/200 wavelength.

All concepts elaborated in the doctoral thesis were implemented experimentally. The functionality of the experiments was systematically examined using appropriate testing objects, such as resolution targets, fluorescent and transparent specimens, polystyrene beads or calibration reflective surfaces for phase reconstruction techniques. To optimize operation of the systems, significant technical improvements were proposed providing an increased optical performance. Technical modifications of experiments with major benefits for applications can be summarized as follows:

- The basic setup for the incoherent correlation holography was supplemented by relay lenses to eliminate a spatial separation of signal and reference waves, resulting in a strong reduction of the field of view. By the relay lenses, a perfect overlapping of the interfering waves was ensured in the entire field of view of the used microscope objective [22].

- A refractive afocal optical system was designed and manufactured in Meopta-optika, s.r.o., enabling an achromatic correction of a diffractive dispersion of the SLM in imaging applications [23]. With the dispersion corrector, light with a low temporal coherence of light can be used in the incoherent correlation imaging, so that spectral filters with a very narrow bandwidth are no longer necessary. The utility model and the Czech and European patents were applied to protect design of the afocal dispersion corrector [25].

- A significant technical simplification of the experiments enabling an axial localization of microparticles by rotating vortex structures was proposed and verified. In the enhanced setup, an expensive SLM operating in a 4-f system was replaced by special diffractive masks, embedded directly into the microscope objective. Design and testing of the spiral masks were done in the doctoral thesis and production was carried out in a cooperation with the Institute of Scientific Instruments Brno (ISI Brno) by electron beam lithography.

- The custom polarization modification of a commercial Mirau interference objective was proposed to realize the polarization sensitive phase-shifting by a LCVR. Using this technique, an original setup enabling quantitative phase imaging with the nanometer precision was implemented [21].

The presented research topics and outputs of the doctoral thesis have been found to be actual and perspective for further elaboration and have become a part of the projects focused on both basic (GA CR) and applied research (TA CR).

The most important results of the doctoral thesis were published in the prestigious physical and optical journals (New Journal of Physics IF 3.558, 1×, [14]; Optics Express, IF 3.488, 4×, [13,18,20,23]; Optics Letters IF 3.292, 2×, [16,21]; Journal of the European Optical Society–Rapid Publications IF 1.231, 1×, [22]), presented at the international conferences (poster presentations 3×, oral presentation 1×) and the workshops of the

4

CDO TA CR (oral presentations 3x). The results of the doctoral thesis were used as the basis of the comprehensive research report summarizing the activities of the Work Package No. 4 of the CDO TA CR (60 pages, [24]). The results of the doctoral thesis also contributed to the presentation of the IPE BUT in 2 papers published in Czech journals (*"Jemná mechanika a optika"* [11] and *"Československý časopis pro fyziku"* [12]). Activities of the doctoral thesis focused on applied research supported application of the utility model and the Czech and European patents [25].

# 3. Theoretical and experimental methods and laboratory equipment

The doctoral thesis is focused on advanced imaging methods profiting from recent discoveries of singular, diffractive and digital optics and utilizing versatile technologies for light shaping. Basic theoretical background of the doctoral thesis has been created by a systematic study of scientific publications in relevant areas of optics. In subsequent research, the original imaging techniques were developed and the improvements of some up-to-date experiments proposed. As basic tools of the theoretical research, both accurate and approximate computational models were used, supplemented by numerical simulations preferably prepared in Matlab. In a direct contact with the experiments, digital techniques were elaborated, enabling the control of optoelectronic devices and measurement processes. The control of some peripheral units was ensured through a LabView interface or using a commercial software. A special attention was also paid to the numerical methods for signal processing and digital image reconstruction applied to experimental data acquired in the setups for correlation holography or quantitative phase imaging.

The experiments were carried out in a new laboratory established at the IPE BUT. It was equipped under the support of GA CR and TA CR projects. Due to a close collaboration between the IPE BUT and the UP, the Laboratory of digital optics [26] (Department of Optics, UP in Olomouc) was available for experiments of the doctoral thesis, which were involved in the scientific program of the joint GA CR and TA CR projects. As a key technology constituting the basis of almost all experiments, a spatial light modulation was used. In general, it represents a controllable transformation of fundamental characteristics of light, such as amplitude, phase or polarization state. Nowadays, diverse technologies are available, enabling the design of versatile light shaping devices based on digitally driven optoelectronic systems. In metrology, a Piezoelectric Deformable Mirror (PDM) or a Micromachined Membrane Deformable Mirror (MMDM) have often been used [27,28]. In imaging applications, the SLMs profiting from electro-optical properties of liquid crystals have been successfully deployed. In the experiments carried out in the doctoral thesis, the liquid crystal technology has been exclusively used for both phase and polarization modulation of light. The modulation systems with considerable variability of operations are available on the market. For a homogeneous phase retardation of light beams, the LCVR may be employed, working with the accuracy better than 1/200 wavelength [29]. In optical or correlation holographic imaging, a lens-like quadratic wavefront modulation is required. In advanced experiments, it has been advantageously carried out using a liquid crystal lens with the ring-shaped electrodes. The focal length of the lens is adjustable in a range from 0.3m to infinity. Unfortunately, the lens is commercially unavailable, although it has appeared in the list of the products of the Flexible Optical B. V. [30]. Currently, the SLMs are most commonly used modulation devices that allow accurate amplitude or phase changes of light in individual pixels of a liquid crystal display [31,32]. Due to a complexity of operation, the SLMs were deployed in a multitude of applications and can be considered as typical light modulating systems. In the experiments based on a polarization sensitive phase-shifting, the LCVRs Thorlabs and Arcoptix providing a constant phase retardation were successfully used [29,33]. In imaging applications requiring a spatially variable phase modulation, the reflective SLM Hamamatsu X10468–01, operating in a phase-only mode, was utilized [32]. These devices are available

in both the IPE BUT and the UP laboratories. To control the SLM effectively, techniques for making Computer Generated Holograms (CGHs) have been developed as a part of the doctoral thesis. The CGH represents a bitmap, which is encoded into the electric signals transferred from the PC to the active display of the SLM. The electric voltage applied to the individual pixels of the display induces different orientation of liquid crystal molecules resulting in changes of the refractive index. Modulation of the refractive index can be used for local changes of the polarization state, which are converted to amplitude variations of light by means of the polarizer and analyzer. In current experiments, the refractive index modulation is more often utilized for a spatially variable phase retardation of the single polarization component of light, enabling a versatile wavefront shaping.

In the implemented experiments, the SLM was controlled by the CGHs created in Matlab using principles of diffractive, Fourier and singular optics. In some cases, a complex modulation, involving both amplitude and phase changes of light, was required. Performing the precisely controlled complex modulation of light by means of a phase-only SLM is difficult. To achieve it, special iterative algorithms for the CGH generation were used, or alternatively, a phase-only modulation was combined with a spatial filtering of light in the Fourier domain.

# 4. Review of current state of the art

In advanced imaging experiments including incoherent correlation imaging, SLM aided optical imaging or holographic microscopy, a precise amplitude and phase transformation of light is required that can be implemented either in illuminating or imaging parts of the setup. High imaging performance can only be achieved in optimized systems conventionally designed using refractive, reflective or diffractive optical elements. In these systems, the diffraction limits of the image quality can even be reached. Unfortunately, the variability of imaging modes is very low, because the parameters of optical elements are fixed. The diversity of functions of the imaging systems can be markedly enhanced using the SLM technology that enables a precise real time shaping of light driven by the PC. Using the SLM, previously unavailable methods for light modulation have become realizable through sophisticatedly designed CGHs controlling the SLM operation. In this way, the versatile methods of light shaping have opened new pathways for developing advanced imaging techniques and their applications. In recent years, the SLM technology has prevailed in a variety of optical experiments shown schematically in Fig. 1.
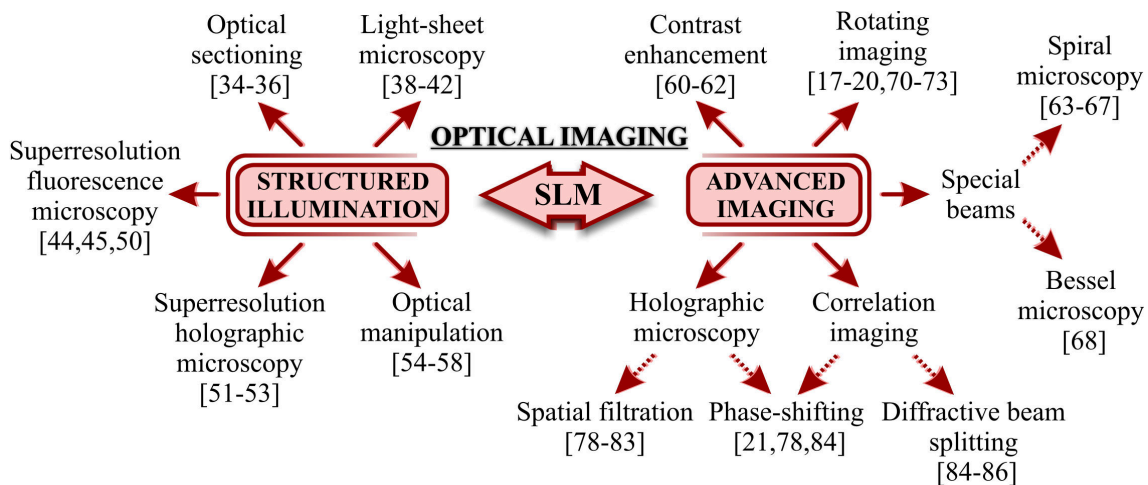


**Figure 1:** Utilization of the SLM in structured illumination and advanced imaging techniques of optical, fluorescence and holographic microscopy.

When used in illuminating parts of optical systems, the SLMs allow to realize various forms of the structured illumination. It is most often implemented in fluorescence microscopy and digital holographic microscopy to achieve the superresolution and the true three-dimensional imaging based on optical sectioning. Projecting a grating pattern on the specimen and then shifting the grating image laterally, the optical sectioning was successfully demonstrated in both fluorescence and bright-field microscopy [34,35]. In the initial experiments, the grating patterns were moved mechanically. Subsequently, the mechanical scanning was advantageously replaced by the techniques of spatial light modulation. Using the SLM operation, variable gratings can be created and simultaneously moved across the sample by simply changing the CGHs sent from the PC to the active display of the device. By this technique, fluorescence endomicroscopy with structured illumination was proposed [36]. In fluorescence microscopy, the depth sectioning capability became available through a local fluorescence activation. This type of structured illumination has been called "light sheets" due to the excitation of the specimen in narrow slices

9

perpendicular to the optical axis. Focusing of the excitation beams to the required slices was achieved by cylindrical lenses [37]. In some experiments, nondiffracting and Airy beams generated by the SLM were used instead of the beams focused by the cylindrical lenses [38–41]. To eliminate effects of strongly scattering media or system aberrations, the imaging performance of light sheet microscopy was further improved using adaptive wavefront correction [42]. Moire effect was successfully used to optimize the image resolution in fluorescence microscopy [43]. It was achieved by projecting the grating patterns with varying azimuthal orientation on the specimen. Generation of the Moire patterns by the SLM was also tested [44] and applicability of the technique demonstrated by living cell experiments [45].

Special attention was paid to the superresolution methods, which are of great importance in fluorescence microscopy [46–48]. The Nobel Prize in Chemistry 2014 was awarded jointly to E. Betzig, S. W. Hell and W. E. Moerner for the development of super-resolved fluorescence microscopy [49]. The method elaborated by Nobel Laureates is known as the Stimulated Emission Depletion (STED) microscopy [46]. In this technique, the superresolution images are created by the selective deactivation of fluorophores caused by the depletion beam. Fluorescence is then excited in the area smaller than the diffraction image spot of the used optical system and the diffraction resolution limit is thus exceeded. In the STED microscopy, optical vortices possessing an annular intensity profile and a helical wavefront are advantageously used in the role of depletion beams. The generation of vortex beams is typically performed by a SLM together with adaptive compensation of aberrations [50].

In the holographic microscopy, the SLM is mainly used for the resolution enhancement applying the synthetic aperture methods [51–53]. By the processing of sub-holograms recorded with different angles of illuminating beams, the synthetic aperture hologram is created. It contains higher frequencies of the spatial spectrum than the related single hologram so that the image reconstruction results in the resolution enhancement. Significant applications of the SLM were also found in optical manipulation. Exploiting versatility of the SLM, optical traps originally created by tight focusing of laser beams [54] were successfully implemented using the real-time phase modulation. In this way, a dynamic laser tweezer providing controllable multiple optical traps was designed and realized [55]. The SLM was also applied to the shaping of special light beams, which allowed controllable rotation, moving or sorting of microscopic objects [56–58].

The SLM was also effectively utilized in the imaging parts of the experimental systems, where it ensured dynamic control and optimization of experimental parameters, adaptive compensation of aberrations, phase modulation of light beams or realization of holographic records under both coherent and incoherent illumination [59]. The main benefits of the SLM aided imaging systems lie in the possibility of introducing new techniques of the phase contrast imaging. In imaging through weakly scattering media, the SLM based modifications of the Zernike phase contrast, dark-field imaging and differential interference contrast were demonstrated. Inserting the SLM into the setup and using proper Fourier filtering methods, the favorable common-path configuration possessing an exceptional resistance against mechanical instabilities became applicable in imaging systems [60–62]. Using the special CGHs displayed on the SLM, various imaging techniques may be operatively combined, reaching an optimal optical performance under given experimental conditions. With the CGHs based on the principles of singular optics, the phase contrast methods were further enriched by spiral phase contrast microscopy [63], enabling

both isotropic and anisotropic edge contrast enhancement of amplitude and phase objects [64–66] or quantitative phase imaging [67]. By similar methods for preparation of the CGHs, Bessel beam microscopy working with nondiffracting beams was proposed and experimentally tested [68]. Recently, optical vortex structures were utilized for three-dimensional imaging applicable to fluorescence microscopy [69]. The imaging method works with a Double-Helix Point Spread Function (DH PSF) arising from interference of optical vortices generated by the SLM. The DH PSF consists of two bright lobes that change their angular orientation due to defocusing. Evaluating the angular rotation of the DH PSF, the axial position of the related object point can be determined with high accuracy. During the past years, several methods of implementation of the DH PSF were proposed, in which a superposition of Laguerre–Gaussian beams [70] or azimuthal and radial discretization of a spiral vortex mask were utilized [71–73]. Combining highly efficient generation of the DH PSF with fluorescence superresolution methods [46–48], a powerful microscope was built that was able to superresolve extended biological structures by localizing single blinking molecules in three dimensions with nanoscale precision [74]. Recently, application of the DH PSF beyond fluorescence microscopy was also demonstrated [20]. In the proposed technique, the defocusing rotation of the DH PSF was achieved due to interference of nondiffracting vortex modes resulting in self-imaging effects. As benefits of the method, an extended axial region exploitable for localization of microobjects and resistance against aberrations were confirmed in the experiments. As the nondiffracting beams were implemented using a high-pass filtering, visualization and localization of weakly scattering phase objects was possible even in a transmission imaging enabling dark field observation [20].

In the vortex imaging working with the rotating DH PSF, three-dimensional objects can be observed provided that are composed of a collection of mutually well separated microscopic emitters. To get full information about volume objects emitting radiation from continuously distributed sources, methods of holographic recording can be applied. Exploiting the benefits of the current optoelectronics technology, methods of digital holography were developed enabling numerical processing of digital holograms acquired in off-axis or in-line configurations. In off-axis digital holography, single hologram recorded with a suitable carrier frequency is processed by Fourier filtering to suppress DC and twin-image terms [8]. In preferred in-line holography providing improved space-bandwidth product [75], multiple holograms must be recorded and processed by the phase-shifting technique [76] to obtain the faithful image unaffected by unwanted holographic terms. In digital holography, quantitative phase imaging was also successfully demonstrated using the phase-shifting conveniently implemented by a SLM. The phase shifts of the reference wave required by the phase-shifting are simply made, when a setup with different optical paths for the signal and reference waves is used [77]. Unfortunately, such setup is highly sensitive to vibrations. To avoid strong requirements on mechanical stability of the system, an exceptionally robust common-path configuration is used in experiments of in-line holography. Resistance against vibrations is then ensured by passing the interfering waves through the same optical path, but implementation of the phase-shifting is more challenging. In the available techniques, Fourier filtering has been usually combined with light shaping technologies to create precise phase shifts of the reference wave. In Spatial Light Interference Microscopy (SLIM) [78], instantaneous Spatial Light Interference Microscopy (iSLIM) [79] or modified Gabor holography [80], the reference wave was created by filtering the spatial spectrum of the specimen. The required phase shifts

were then imposed on the reference wave by a SLM placed at the Fourier plane. Similar phase-shifting methods were also used in a point diffraction interferometer deployed in metrological applications [81,82]. In holographic and interferometric experiments based on the common-path configuration, the SLM was also effectively used as a diffractive beam splitter. Its operation then allowed splitting of each input wave to the signal and reference waves and their independent shaping carried out together with the phase-shifting [83].

Diffractive splitting and shaping of light waves, made operatively by the SLM, were used in the design of experiments of the incoherent correlation holography [84,85]. The holographic experiments realized with spatially incoherent light opened new pathways for development of incoherent holographic microscopy applicable to imaging of three-dimensional fluorescent samples [86]. In recent years, this promising area of microscopy has been widely developed and considerable progress has been made in both new imaging principles and technical improvement of experiments. Using wave optics modeling originally proposed to optimize experiments working with nearly monochromatic spatially incoherent light, a hybrid coherence regime and a violation of the Lagrange invariant were revealed [13]. Based on these special characteristics of the correlation holographic imaging unavailable in conventional optical imaging systems, a way to overcome the diffraction resolution limit was found and experimentally verified [87–89]. A spatial separation of interfering waves, drastically reducing the field of view in original experiments, was removed by additional relay lenses properly inserted into the setup. In this way, a perfect overlapping of interfering waves was achieved and the field of view significantly extended [22]. To optimize low light experiments, the basic simulation model of the correlation imaging valid for monochromatic light was further developed for broadband light [14,15]. In rigorous analysis, temporal coherence of light, optical path difference of interfering waves and diffractive dispersion of the SLM were examined and their influence on the image resolution was found. It was shown that the sub-diffraction resolution of the incoherent correlation imaging can be achieved even with a low temporal coherence of light, provided that the diffractive dispersion of the SLM is eliminated [14]. With the achromatic correction of the SLM dispersion [23], the concept of incoherent correlation microscopy using broadband light was proposed, providing improved signal to noise ratio and high resolution of the reconstructed image. Application potential of the incoherent correlation imaging was further extended by incorporating optical vortices, which gave rise to advanced imaging modes enabling the spiral imaging and the anisotropic edge contrast enhancement of three-dimensional objects [16]. Vortex and nondiffracting beams were also used to implement the DH PSF in the incoherent correlation imaging and digital holographic microscopy. With this modification, the precise axial localization of microparticles based on defocusing rotation of the image became possible also in the methods of holographic microscopy using either coherent or incoherent illumination [17,18].

In the common-path configurations of digital holography, the phase-shifting is achieved by the spatial filtering of light passing through the sample. In such a process, an independent reference wave is not provided. In holographic microscopy and holographic metrology, the systems operating with the reference wave unaffected by the specimen are highly desirable. The reference wave that did not pass through the sample was advantageously obtained in the systems utilizing Mirau or Michelson interference objectives, where the phase-shifting was performed using a piezoelectric transducer [90]. Recently, the birefringence properties of the LCVR were utilized for all-optical motion-less phase-shifting implemented in polarization sensitive Mirau interferometer [21]. The technique

was based on a polarization adapted Mirau objective and it took all the advantages of previously known methods working with the orthogonally polarized beams [91–93]. Using this method, the precise quantitative phase measurements were demonstrated with the accuracy better than 1/200 wavelength [21]. The polarization phase-shifting represents a promising approach for deployment of more versatile liquid crystal devices in the common-path interference systems.

A detailed overview of imaging and metrological applications of the SLM was published in the research report of the CDO TA CR [24].

# 5. Outcomes of basic research

The doctoral thesis is focused on both fundamental and technical problems of advanced imaging. The thesis is divided into parts devoted to basic and applied research, where the achieved results and activities are discussed separately.

The main outputs of basic research were obtained by examining new principles of incoherent correlation holography and digital holographic microscopy. New imaging concepts were developed theoretically and tested experimentally, based on recent discoveries of singular and nondiffracting optics. The special beams used in experiments were introduced by principles of spatial light modulation and advanced light shaping. The realized experiments were controlled by the SLM as a versatile tool providing a real time amplitude, phase or polarization modulation of incident light.

The examined techniques of digital imaging can be considered as a two-stage process. Acquisition of experimental data performed in the optical stage is followed by the signal processing and digital image reconstruction. Using a SLM during the data acquisition, imaging variability was significantly enhanced. It allowed multitude of imaging modes, which were introduced either optically or digitally. The proposed and experimentally tested imaging modes are summarized in Fig. 2. In basic configurations, the
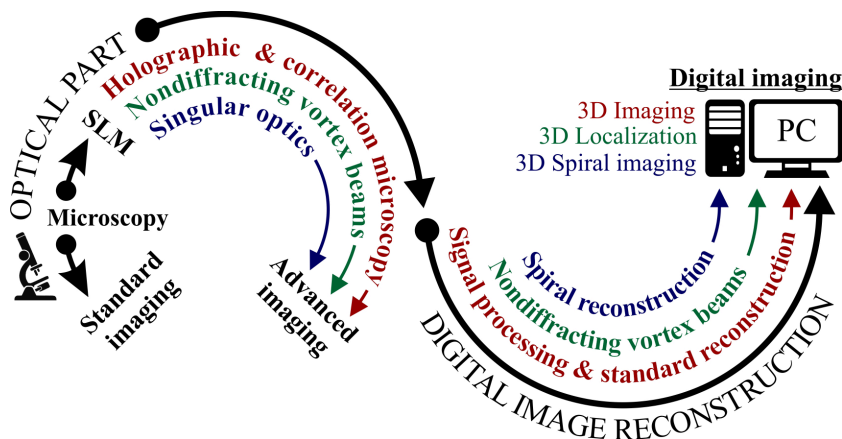


**Figure 2:** Imaging modes available in the SLM aided incoherent correlation holography and digital holographic microscopy. Variability of imaging is achieved by versatile light shaping and advanced data processing carried out in optical and digital parts of the developed methods.

SLM was used as a tube lens with a variable focal length. It enabled adaptive refocusing in a conventional bright-field microscope. The bright-field microscope can be advantageously transformed into a common-path interferometer provided the SLM is operated as a diffractive beam-splitting and phase-shifting device. By dividing each incident wave into two spatially coherent waves, experiments of correlation imaging and incoherent holographic microscopy were introduced. The acquisition of correlation records was accompanied by a precise phase-shifting so that a faithful image reconstruction of fluorescent and incoherently illuminated objects became possible. Principles of singular optics were transferred into the correlation imaging either by optical or digital modifications of the basic experiment. The proposed spiral correlation imaging provided anisotropic edge contrast enhancement of three-dimensional objects. The self-imaging of nondiffracting vortex beams was successfully deployed in a DH PSF engineering. The DH PSF was

implemented both optically and digitally and utilized for a three-dimensional localization of microparticles in optical microscopy, digital holography and incoherent correlation imaging.

## 5.1. Incoherent correlation imaging

Incoherent correlation microscopy is a new method for recording digital holograms under incoherent illumination. Unlike the competitive techniques of incoherent holography [94,95], the SLM aided correlation imaging is a non-scanning and motionless method opening new applications in outdoor holography and fluorescence holographic microscopy [84,86]. The incoherent correlation imaging effectively combines optical microscopy and exceptionally stable common-path interferometry. In a basic experimental configuration, the SLM is placed at the output of a standard microscope, while interferometric beams are created by various methods of diffractive [16,84,88] or birefringent beam splitting [85]. A typical optical arrangement demonstrating principles of both correlation record acquisition and numerical image reconstruction are shown in Fig. 3.
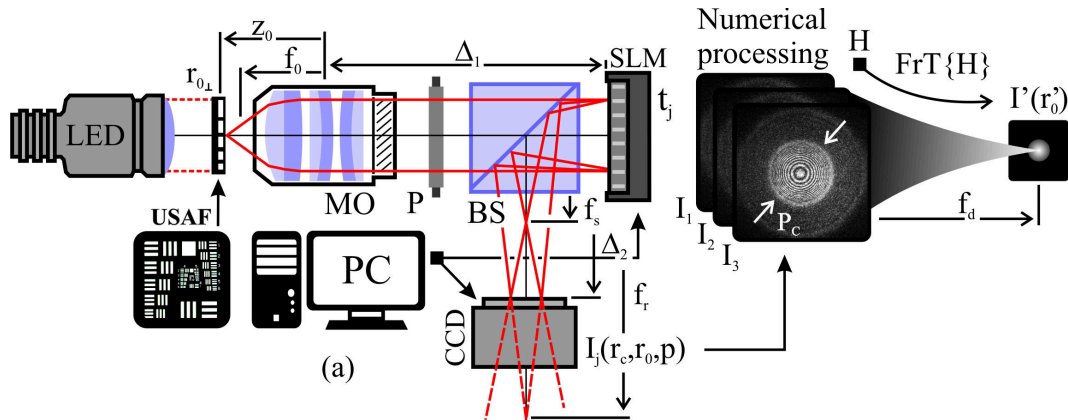


**Figure 3:** Scheme of incoherent correlation microscopy, incorporating both optical and digital stages of imaging process: LED-light emitting diode, MO-microscope objective, P-polarizer, BS-beam splitter, SLM-spatial light modulator, CCD-charged coupled device.

Contrary to a standard bright-field imaging, the sample is illuminated by a collimated incoherent light source. It reminds conditions of Köhler illumination with a closed condenser diaphragm. In the fluorescence correlation imaging, any additional demands are not imposed on the illumination part of the setup, so that a standard excitation module and its accessories are applicable. The correlation imaging is based on the fact that every point source, either scattering or emitting light, is self-spatially coherent. In the imaging process, light scattered or emitted by the sample is captured by infinity corrected microscope objective (MO) and directed through a linear polarizer (P) and a beam splitter (BS) towards a SLM. Each wave impinging on the SLM is divided into two interfering waves, provided the polarizer P is optimally adjusted. The created waves correspond to mutually coherent signal and reference waves, respectively. At the CCD plane, the records of the sample are formed by incoherent addition of point holograms related to individual object points. The correlation imaging benefits from a common-path geometry ensuring an exceptional stability of interference patterns and minimal optical path difference. On

the other hand, a faithful image reconstruction is not available by a single exposure and both DC term and holographic twin-image have to be eliminated by processing of multiple phase-shifted recordings [76,84].

Optical performance of the correlation imaging was theoretically elaborated at different levels. With increasing demands on complexity of experiments, the imaging performance was successively studied in paraxial and wave models working with both monochromatic and broadband spatially incoherent light. In the proposed models, the available optical limits were assessed and optimal experimental configurations explored. The developed computational models and their outcomes can be categorized as follows:

- Paraxial model of the correlation imaging using monochromatic spatially incoherent light - description of hologram recording and image reconstruction, - calculation of the lateral and longitudinal magnification, - exploration of a hybrid coherence regime of the imaging [6,13], - explanation of the Lagrange invariant violation.

- Scalar wave model of the correlation imaging using monochromatic spatially incoherent light - explanation of the diffraction limited image formation, - calculation of the three dimensional PSF, - optimization of experiments for monochromatic light, - determination of the resolution limits and explanation of the sub-diffraction resolution [6,13].

- Second-order coherence model of the correlation imaging using broadband light - image reconstruction in conditions of reduced temporal coherence of light, - optimization of experiments for broadband light [14,15], - description of resolution limits of dispersion-free systems operating with broadband light.

A deeper elaboration of the correlation imaging is at the forefront of interest of running TA CR and GA CR projects, where spatial coherence effects and aberration robustness of the method will be tested and assessed both theoretically and experimentally.

### 5.1.1. Monochromatic incoherent correlation imaging

By the models developed in the doctoral thesis, the early experimental configurations proposed in [85,96] were found to be unfavorable for a high resolution imaging. In the digital imaging realized by means of the correlation records, the resolution of the used microscope objective was strongly deteriorated. By novel system adjustments originally established in [13], the diffraction resolution limits were achieved in digitally reconstructed image. Furthermore, clarification of the connection between optical and digital stages of the imaging [13] stimulated research resulting in advanced experiments on overcoming of the diffraction resolution limits [87,88].

The basic model of the correlation imaging was developed for the monochromatic spatially incoherent light. Under these conditions, light waves originating from individual object points are mutually uncorrelated. Since the signal and reference waves are created by splitting light from the same object point, their interference may occur regardless of the optical path difference. Assumption of the monochromatic spatially incoherent light simplifies simulation of experiments, while maintaining reliable information about the principle of the image formation and the role of experimental parameters.

In the developed computational model, the recording and digital image reconstruction of a single point source can be examined. The implemented algorithms enable simulation

of the point correlation records and analysis of the three-dimensional PSF. In the performed calculations, a single point source located near the front focal plane of the MO is considered. Light captured by the MO is then nearly collimated and directed through the imaging system towards the SLM. At the SLM, mutually coherent signal and reference waves are created by amplitude splitting of incident light. The wavefronts of signal and reference waves are independently shaped and constant phase shifts are successively imposed on the signal wave. Subsequently, a coherent superposition of both waves is calculated at the CCD plane. In the interference field, both the three-dimensional position of the object point and the phase shift of the signal wave are encoded. By processing the phase shifted records, the PSF of the system is established, providing comprehensive information about optical quality of the examined experimental configuration.

**Point spread function of the incoherent correlation imaging**

In conventional optical microscopy, the PSF is created by direct imaging of a single point source. The situation is different in the correlation imaging. The PSF is formed in two steps including holographic recording and digital reconstruction of the point image. In this case, the relationship between the shape of the PSF and the experimental parameters is more complex and an advanced simulation model is required to assess the quality of the imaging.

In the developed computational model, the PSF is calculated for an arbitrary point of the field of view. Its position is given by the Dirac delta-function $\delta(\mathbf{r} - \mathbf{r}_0)$, where $\mathbf{r}_0 \equiv (\mathbf{r}_{0_\perp}, z_0)$ and $z_0$ denotes an axial distance measured from the MO (Fig. 3). Because the object point is located near the front focal plane of the MO, the emitted spherical wave is collimated by the MO and directed towards the SLM. The complex amplitude $u_0$ of the wave impinging on the SLM depends not only on the position vector of the source $\mathbf{r}_0$, but also on the parameters $f_0$ and $\Delta_1$ representing the focal length of the MO and the distance between the MO and the SLM, respectively. At an active area of the SLM, the CGHs with the transmission function

$$t_j = T_s \exp(i\theta_j) + T_r, \quad j = 1, 2, 3, \tag{1}$$

are successively addressed. The SLM is operated as a phase shaper, which simultaneously splits the energy of the input wave into two mutually coherent waves, signal and reference waves. The wavefronts of the signal and reference waves are independently shaped by the factors $T_s$ and $T_r$ representing transmission functions of lenses with the focal lengths $f_s$ and $f_r$, respectively. During the phase modulation, constant phase shifts $\theta_j$ are simultaneously imposed on the signal wave. It enables implementation of the phase-shifting procedure that results in a faithful image reconstruction. Under common conditions, the propagation of light fields between the SLM and the CCD can be described by the Fresnel transform FrT. The complex amplitude of light captured by the CCD is then given as

$$u_j = u_s \exp(i\theta_j) + u_r, \quad j = 1, 2, 3, \tag{2}$$

where $u_s = \text{FrT}\{u_0 T_s\}$ and $u_r = \text{FrT}\{u_0 T_r\}$. In the paraxial approximation, the interfering waves are described as paraboloidal waves. To simulate interference patterns created by the signal and reference waves at the CCD, an area of spatial overlapping of the waves $P_c(\mathbf{r}_{c_\perp})$ must be determined in dependence on the transverse CCD coordinates $\mathbf{r}_{c_\perp}$. In

implemented algorithms, the aperture function $P_c$ is calculated by ray tracing procedures. The phase-shifted interference patterns representing point holograms recorded in spatially incoherent light can then be written as

$$I_j = P_c|u_j|^2, \quad j = 1, 2, 3, \tag{3}$$

where $u_j$ is given by (2). The area of spatial overlapping of interfering waves has a complicated dependence on the focal lengths $f_0$, $f_s$ and $f_r$ and the distances $\Delta_1$ and $\Delta_2$ determining position of the MO and the CCD with respect to the SLM, respectively. In a basic configuration of the experiments shown in Fig. 3, the area of overlapping of interfering waves is a critical parameter. A full overlapping of interfering beams is achieved only for the points located on the optical axis of the system and the size of the interference area rapidly decreases with increasing field of view. The image reconstruction is therefore possible only in a very small area of the field of view of the MO used. In the doctoral thesis, the experiments were modified to maintain a full spatial overlapping of interfering beams in the entire field of view of the MO and to retain optimal image resolution in peripheral parts of the sample [22]. Enhancement of the system is based on the use of relay optics and will be further discussed in the section devoted to applied research. The size of effective interference area is completely determined by the geometric overlapping of beams only when quasi-monochromatic light is used. When using broadband light, effects associated with partial temporal coherence must be considered. In this case, the point correlation records are bounded by a coherence aperture, whose size depends on the coherence length of light, the optical path difference of interfering waves and dispersive effects. In the doctoral thesis, these issues were examined in terms of both theoretical and applied research [14,15,23].

By processing the phase-shifted correlation records $I_j$, both the DC term $|u_s|^2 + |u_r|^2$ and the twin image $u_s^* u_r$ are effectively removed. The desirable holographic term $H \propto u_s u_r^*$ is then used for reconstruction of a faithful image. The complex point hologram $H$ represents the transmission function of a diffractive lens carrying information about amplitude and spatial position of the relevant object point. By the numerical reconstruction of all point records made collectively, three-dimensional amplitude objects can be imaged. In the developed simulation model, both the point hologram $H$ and its reconstruction were described analytically in a dependence on the experimental parameters [5,6,13]. It allowed to interpret the hologram reconstruction as imaging by a virtual lens. A lateral position of the optical axis of the lens and its focal length $f_d$ were used as parameters clearly indicating the spatial position $\mathbf{r}_0$ of the relevant object point.

The complex amplitude of the point image $u'$ is obtained by the Fresnel transform of the point hologram, $u' = \text{FrT}\{H\}$. If the geometry of the experiment does not meet the conditions required by the Fresnel diffraction, the image reconstruction is performed by using the Kirchhoff diffraction integral. The image intensity $I' = |u'|^2$ depends on the lateral and longitudinal coordinates $\mathbf{r}'_\perp$ and $z'$, respectively, and provides the three-dimensional PSF of the incoherent correlation imaging. By examining the PSF, the connection between optical and digital stages of the imaging can be revealed and parameters of the experimental setup optimized. In the basic simulation model of the correlation imaging, the paraxial imaging concept was developed that enables to determine the coordinates of the digital image $(\mathbf{r_0}'_\perp, z'_0)$ in dependence on the object point coordinates $(\mathbf{r_0}_\perp, z_0)$. The lateral and longitudinal magnifications then can be defined as $m = |\mathbf{r}'_{0_\perp}|/|\mathbf{r}_{0_\perp}|$ and $\alpha = dz'_0/dz_0$, respectively. When the point records are realized by aberration-free optics,

the PSF can be used to explore the diffraction imaging limits. The lateral size of the diffraction image spot $\Delta r'$ is then proportional to the ratio of the wavelength $\lambda$ and the image numerical aperture $NA'$, $\Delta r' \propto \lambda/NA'$. If the quasi-monochromatic light is used, the numerical aperture $NA'$ is determined as a ratio of the lateral size of the overlapping area $P_c$ of the interfering waves and the focal length of the virtual diffractive lens $f_d$. Due to a violation of the Lagrange invariant discovered in the doctoral thesis [13], the object space resolution is related to the image space resolution in different way than in the optical imaging with direct image detection. As will be shown below, this property of the correlation imaging can be used to overcome the diffraction resolution limit.
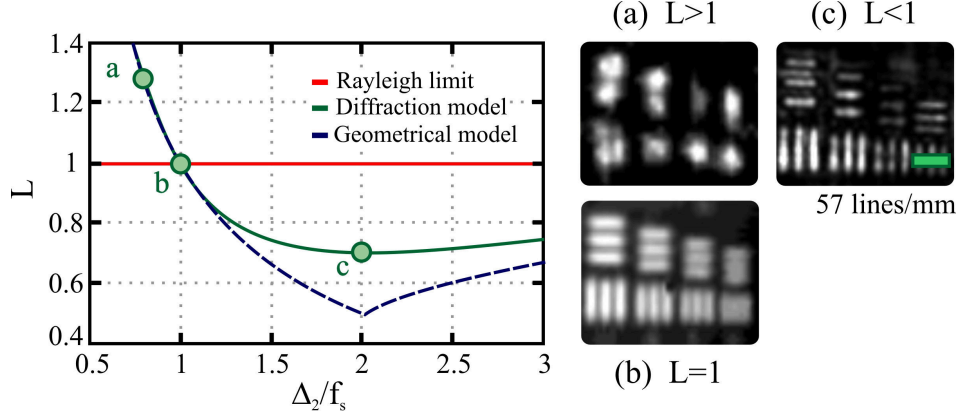
## Superresolution in the incoherent correlation imaging

In conventional optical imaging systems, the Lagrange invariant can be used to express the lateral magnification as a ratio between the object and image space numerical apertures, $m = NA/NA'$. Applying the Rayleigh criterion to the diffraction limited imaging, two image spots of the same intensity can be regarded as resolved, if the distance of the intensity maxima is equal to the radius of the Airy pattern, $\Delta r' \propto \lambda/NA'$. Since the related distance in the object space is given as $\Delta r = \Delta r'/m = \lambda/NA$, the object space resolution is also diffraction limited. In the incoherent correlation imaging, the Lagrange invariant is not inherently fulfilled and the lateral resolution $m$ can be changed independently from the numerical apertures $NA$ and $NA'$. This effect can result to a significant deterioration of the resolution of the used MO, when the system is not properly configured. Initial experiments suffered from this deficiency [85,96]. An optimal configuration retaining diffraction limited imaging was found theoretically and tested experimentally in [13]. The obtained results motivated further research focused on the Lagrange invariant violation [97,98]. The research resulted in the design of two different experiments, in which the resolution beyond the diffraction limit of the MO was even demonstrated [87,88]. Both superresolution configurations differ in wavefront geometry of the signal and reference waves, but identically benefit from the broken interdependence between the lateral magnification and the numerical apertures of the optical system [13,97,98]. In the first system adjustment [87], the violation of the Lagrange invariant was tested for a plane reference wave ($f_r \to \infty$). In this configuration, the lateral magnification vary with the CCD position, $m \equiv m(\Delta_2)$, while the image space numerical aperture $NA'$ remains unchanged regardless of $\Delta_2$ [13]. If the lateral magnification $m(\Delta_2)$ and the size of the diffraction image pattern $\Delta r'$ are known, the size of the related object space pattern can be determined as $\Delta r = \Delta r'/m(\Delta_2)$. To quantify a degree of the superresolution, the coefficient $L = \Delta r/\Delta r_0$ may be used, where $\Delta r_0 = \lambda/NA_0$ and $NA_0$ denotes the numerical aperture of the MO. As is obvious, the coefficient $L$ compares the size of the object spots obtained in the incoherent correlation imaging and the direct optical imaging, respectively. For a detailed discussion of different system adjustments, the superresolution coefficient can be appropriately rewritten as

$$L = \frac{NA_0}{|m(\Delta_2)|NA'}. \tag{4}$$

The lateral magnification of the correlation imaging increases linearly with $\Delta_2$, while $NA'$ remains constant [13]. The coefficient $L$ gradually decreases with increasing $\Delta_2$. For sufficiently large magnifications its value $L < 1$ is achieved that indicates the superresolution in the incoherent correlation imaging. This preferred CCD positioning does not

work without limitations since $NA'$ remains constant only in a restricted range of distances $\Delta_2$, given by the condition $\Delta_2 \leq 2f_s$. The minimal value of $L$ is obtained for $\Delta_2 = 2f_s$, because at the CCD positions $\Delta_2 > 2f_s$, the image numerical aperture $NA'$ decreases with $\Delta_2$. Using basic experimental parameters, the coefficient $L$ can be expressed in the form



**Figure 4:** Dependence of the coefficient $L$ on the relative CCD position $\Delta_2/f_s$ with areas of the deteriorated imaging ($\Delta_2/f_s < 1$) and the superresolution ($\Delta_2/f_s > 1$). The snapshots (a) and (c) demonstrate degraded and enhanced resolution of the incoherent correlation imaging in comparison with the direct optical imaging (b).

$$L = \begin{cases} f_s/\Delta_2 & \text{for} \quad \Delta_2 \leq 2f_s, \\ R_p|\Delta_2 - f_s|/(\Delta_2 R_c) & \text{for} \quad \Delta_2 > 2f_s, \end{cases} \tag{5}$$

where $R_p$ and $R_c$ denote the radii of the active SLM area and the overlapping area of the signal and reference waves at the CCD, respectively. Dependence of the coefficient $L$ on the ratio $\Delta_2/f_s$ is illustrated by the dashed blue line in Fig. 4. As is obvious from (5) and Fig. 4, the coefficient $L > 1$ is obtained at the CCD positions $\Delta_2/f_s < 1$. It indicates a deterioration of the resolution of the used MO. At the CCD position $\Delta_2/f_s = 1$, the diffraction limit of the optical imaging is reached also in the incoherent correlation imaging. The superresolution is available for $\Delta_2/f_s > 1$. The best resolution is achieved when $\Delta_2/f_s = 2$, so that the distance between the SLM and the CCD is two times larger than the focal length of a diffractive lens addressed on the SLM. In this case the superresolution with factor 2 is reached, meaning that the object space diffraction spot is twice less in the incoherent correlation imaging than in the optical imaging realized by the MO. The dependence of the superresolution coefficient $L$ on $\Delta_2/f_s$ was also examined in the advanced model, where the ray tracing was replaced by the wave propagation (solid green line in Fig. 4). In this approach, the best superresolution state corresponds to $L \approx 1/\sqrt{2}$.

In experiments, the resolution limits were examined using a low magnification MO (achromatic doublet, $NA_0 = 0.15$, $f_0 = 150$ mm). The signal and reference waves were shaped by the diffractive lenses with the focal length $f_s = 750$ mm and $f_r \to \infty$, displayed on the SLM. Experimental results obtained with the USAF resolution target are shown in Fig. 4. The images of the resolution target reconstructed from the holograms recorded at the CCD positions $\Delta_2/f_s < 1$ and $\Delta_2/f_s = 2$ are compared with a direct optical image detected at $\Delta_2/f_s = 1$ (points a, b and c on the solid green line in Fig. 4). In the direct imaging, the SLM was used as a tube lens with the focal length $f_s = 750$ mm.

21

As is obvious, the snapshot (c) obtained from the holograms recorded at the optimal CCD position (point c on the solid green line) has apparently higher resolution than the snapshot (b) corresponding to the direct imaging. Just resolved spatial frequencies were determined as 57 and 40 lines/mm for snapshots (c) and (b), respectively. The ratio $40/57$ fits well with the best theoretical value of the superresolution coefficient $L \approx 1/\sqrt{2}$ obtained in the advanced wave model. In the snapshot (a), which corresponds to the inappropriate CCD position (point a on the solid green line), the image is significantly degraded ($L > 1$) and the resolution of the test features is completely lost. A thorough experimental study on the incoherent correlation imaging with the resolution beyond the diffraction limit was published in [87].

The demonstrated superresolution technique was based on increasing the lateral magnification, while maintaining the image numerical aperture constant. In [88], another way of the Lagrange invariant violation was proposed to reach the superresolution. In this method, the spherical signal and reference waves and the CCD position were adapted to each other to achieve the best image resolution, $\Delta_{2opt} = 2f_s f_r/(f_s + f_r)$. The resolution enhancement is then evaluated by the coefficient $M = NA'/NA'_d$, where $NA'$ denotes the numerical aperture of the reconstructed hologram representing a virtual lens with the focal length $f_d = |(\Delta_2 - f_s)(f_r - \Delta_2)|/|f_s - f_r|$ and $NA'_d$ is the image numerical aperture of a conventional imaging system composed of the MO and the tube lens with the focal length equal to $\Delta_{2opt}$. The tube lens is realized by the SLM and its image numerical aperture is given as $NA'_d = R_c/\Delta_{2opt}$, where $R_c$ is the radius of the active area of the SLM. At the CCD positions with $M > 1$, the numerical aperture of the hologram $NA'$ is higher than the numerical aperture of the conventional imaging lens $NA'_d$ and the resolution beyond the diffraction limit is reached. The theoretical dependence of the coefficient $M$ on the relative CCD position $\Delta_2/\Delta_{2opt}$ is shown in Fig. 5. The CCD setting $\Delta_2/\Delta_{2opt} = 1$ results in $M = 2$ indicating the highest level of the superresolution. The resolution enhancement is the same as in the previously examined case with the plane reference wave [87].
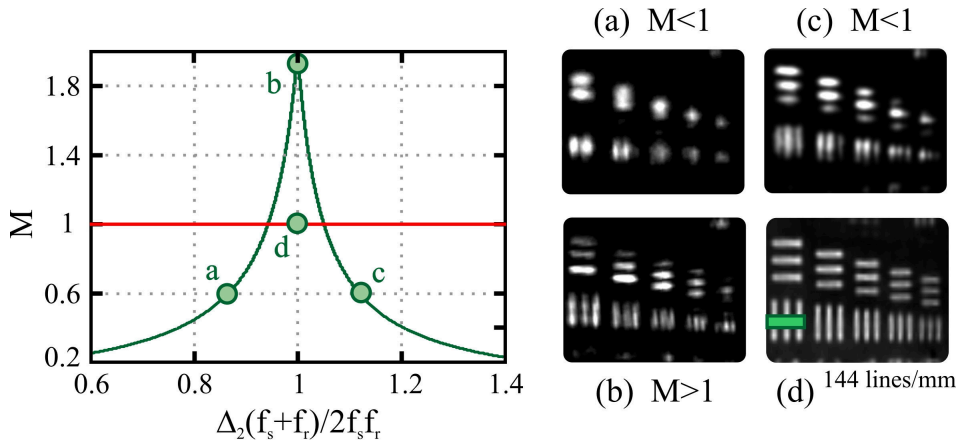


**Figure 5:** Dependence of the coefficient $M$ on the relative CCD position $\Delta_2/\Delta_{2opt}$ with the indicated superresolution imaging (point b on the green line). The snapshots (a), (b) and (c) reconstructed from the records at the relevant positions of the theoretical green curve do not confirm theoretically predicted resolution enhancement of the optical image created by the MO and the SLM tube lens (snapshot (d)).

In the experiments, the MO Melles Griot ($NA_0 = 0.28$, $f_0 = 20$ mm) and the SLM diffractive lenses with the focal lengths $f_s = 470$ mm and $f_r = 523$ mm were used. The

correlation records were captured under system adjustments related to the points a, b and c of the theoretical green curve in Fig. 5. The snapshots (a), (b) and (c) obtained by the numerical reconstruction of the correlation records were compared with the optical image (d), created by the MO and the tube lens displayed on the SLM. In accordance with the theory, the best reconstructed image was obtained in the position b providing the highest numerical aperture $NA'$, but the predicted resolution enhancement of the optical image was not proven. Up to now, the resolution enhancement based on the increased image numerical aperture of the holographic lens has been demonstrated only in [88], where rather artificial experimental conditions were used. The MO was replaced by a low aperture lens ($NA_0 = 0.02$, $f_0 = 250$ mm) and the superresolution effect demonstrated on a resolution target with 10 lines/mm. The results of the doctoral thesis indicate that the system working with the spherical reference wave is more sensitive to aberrations, which prevent to achieve superresolution in real experimental conditions. Such problems will be further addressed in subsequent research.

### 5.1.2. Broadband incoherent correlation imaging

The basic computational models of the incoherent correlation imaging were developed on the assumption that a monochromatic spatially incoherent light is used [13,84]. To ensure such conditions, the narrow bandpass filters must be used in experiments. It is restrictive for practical applicability of the method. In the seminal paper on the incoherent correlation imaging [84], the hologram recording under spectral bandwidth $\Delta\lambda = 60$ nm was realized, demonstrating a great potential of the method for experiments prepared with reduced temporal coherence of light. The performed experiments were not supported by an adequate theory and in the ongoing research, the configurations optimized for monochromatic light were unjustifiably used. In the doctoral thesis it was revealed, that the parameters used in monochromatic experiments must be further optimized, when broadband light is used. The development of an advanced computational model valid for broadband light and considering effects of partial temporal coherence and dispersion became an important theoretical task of the doctoral thesis. It was successfully solved by exploiting the second-order coherence theory. In the proposed model, a close relationship among the temporal coherence of light, the optical path difference of interfering waves and the attainable image resolution was examined and interpreted by original concept of the coherence induced aperture. Within these theoretical concepts, new experiments were designed and tested that enable to reach the monochromatic resolution limits even if a broadband light is used [14,15].

To achieve the theoretical resolution limits in the broadband light, technical problems associated with the dispersion effects were also solved. The main attention was focused on an extremely strong diffractive dispersion of the SLM, which was effectively compensated by an afocal refractive corrector providing an achromatic quadratic phase modulation through a visible spectral range [23]. Design and experimental testing of the corrector is presented in a separate part of the doctoral thesis, devoted to applied research outcomes.

In an accordance with the previous sections of the doctoral thesis, the broadband model of the incoherent correlation imaging is discussed for a single point imaging. It enables to examine the point correlation records and the three-dimensional PSF under influence of the partial temporal coherence of light and the optical path difference of interfering waves.

In the calculations, the point correlation record is obtained by interference of signal and reference waves $\overline{u}_s$ and $\overline{u}_r$. They can be written as

$$\overline{u}_m(t) = a_m \mathrm{FT}\left\{v(\nu)\exp[i\Phi_m(\mathbf{r_0}, \mathbf{r_c}, \nu)]\right\}, \quad m = s, r, \tag{6}$$

where FT denotes the Fourier transform, $v$ is a random spectral component of light with the frequency $\nu$ and $a_s$ and $a_r$ denote amplitudes of the signal and reference waves, respectively. The phase factors $\Phi_s$ and $\Phi_r$ are given as $\Phi_m = 2\pi\nu D_m/c$, $m = s, r$, where $c$ represents the speed of light in vacuo and $D_s$ and $D_r$ are optical paths of the signal and reference waves between object and detector points specified by the position vectors $\mathbf{r}_0$ and $\mathbf{r}_c$, respectively. Intensity of the point correlation record is obtained by the time averaging,

$$\overline{I}_j = \langle|\overline{u}_s(t)\exp(i\theta_j) + \overline{u}_r(t + \tau)|^2\rangle, \quad j = 1, 2, 3, \tag{7}$$

where $\tau$ is a time delay between the signal and reference wave and $\theta_j$ denotes the constant phase shifts imposed on the signal wave. As the Fourier components of light that belong to different frequencies are uncorrelated, we can write

$$\langle|v(\nu)v^*(\nu')|^2\rangle = \delta(\nu - \nu')|g(\nu)|^2. \tag{8}$$

Here, $\delta$ and $g$ denote the Dirac delta function and the power spectrum of the light source. Assuming that the interfering waves have no initial time delay ($\tau = 0$), the broadband point correlation records can be written in the form

$$\overline{I}_j = \int_{-\infty}^{\infty} |g(\nu)|^2 I_j(\nu) d\nu, \tag{9}$$

where $I_j(\nu)$ represent the monochromatic point correlation records, created for individual spectral constituents. The fringe modulation of the records $I_j(\nu)$ depends on the frequency $\nu$ and the optical path difference $\Delta D = D_s - D_r$,

$$I_j(\nu) = a_s^2 + a_r^2 + 2a_s a_r \cos(2\pi\nu\Delta D/c + \theta_j). \tag{10}$$

Performing the integration (9), the overall correlation records $\overline{I}_j$ are obtained. Their interference oscillations are dampened by an envelope created due to the partial temporal coherence of light (Fig. 7). Therefore, the envelope will be called the coherence induced aperture. Its width depends on the coherence length of light and the optical path difference of interfering waves. After the phase-shifting procedure, the point hologram is obtained that corresponds to a virtual diffractive lens bounded by the coherence induced aperture. The partial temporal coherence then directly determines the image numerical aperture $NA'$ and hence the diffraction resolution of the reconstructed image. For an infinite coherence length of light, the coherence induced aperture extends to infinity and the reconstructed virtual lens is bounded geometrically by the overlapping area of interfering beams. In this case, the monochromatic resolution limits are reached. As shown in the doctoral thesis, there is another theoretical way how to achieve an infinite coherence aperture even when a broadband light is used. It is based on the reduction of the optical path difference, which goes to zero in the limiting case. In optimally designed experiments, the optical path difference is minimized and the monochromatic resolution preserved also in the broadband light. In applications using broadband light, dispersion

of optical components have a negative effect on the imaging performance. In order to achieve the physical resolution limits of the broadband imaging, dispersion effects must be eliminated. This problem can be solved by appropriate technical means, so that the nondispersive simulation model is meaningful for evaluating optical performance of the broadband correlation imaging.

In the nondispersive model, the optical path difference $\Delta D$ is independent of the frequency $\nu$. Assuming the Gaussian power spectrum of the source, the integration (9) can be performed analytically and the point correlation records $\bar{I}_j$ processed by the phase-shifting [76,84]. As a result, the point hologram $H$ used in the image reconstruction is obtained,

$$H = a_s a_r A_c \exp(i\Delta\Phi), \tag{11}$$

where $\Delta\Phi$ is a quadratic phase function that retains information about the spatial position of the recorded object point. The point hologram is bounded by the envelope $A_c$ appearing due to the partial temporal coherence. When the light source with the Gaussian power spectrum is applied, the coherence induced aperture can be written as

$$A_c = \exp(-\pi\Delta D^2/2L_c^2). \tag{12}$$

The coherence aperture depends on the coherence length $L_c$ and the optical path difference of the interfering waves $\Delta D$, respectively. The width of the aperture can be determined through a dependence of $\Delta D$ on the lateral coordinates $\mathbf{r}_{c\perp}$.
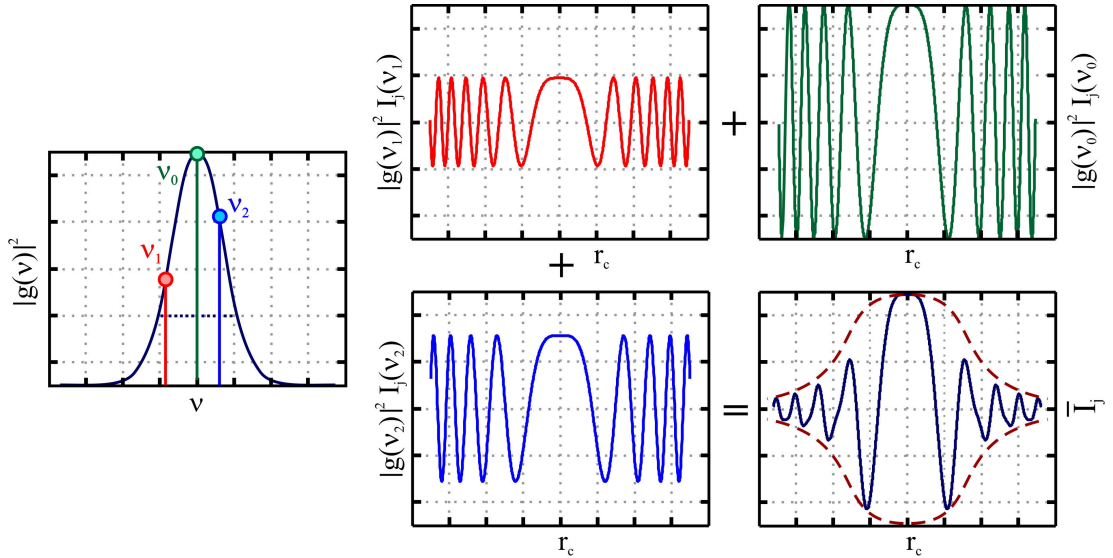


**Figure 6:** Graphical illustration of a spatial bounding of the broadband correlation record: superposition of the monochromatic records (red, green and blue patterns) creates a spatial envelope called coherence induced aperture (red dashed line), which dampens the final record in its peripheral region.

Formation of the coherence aperture is graphically illustrated in Fig. 6. In the monochromatic correlation imaging, the coherence length of light is infinite and the coherence aperture also extends to infinity. In this case, the interference oscillations of the correlation records remain undamped in the entire area of the geometric overlapping of the signal and reference waves (red, green and blue monochromatic records in Fig. 6). In the broadband

25

incoherent correlation imaging, the situation is changed. The overall correlation records $\overline{I}_j$ are obtained by the integral (9), in which the monochromatic records $I_j(\nu)$ are superposed with the weighting function given by the power spectrum of the source $|g(\nu)|^2$. Due to a frequency dependence, the maxima of the interference oscillations are mutually shifted in the individual monochromatic records. This effect is particularly apparent in peripheral areas, where interference patterns strongly affect each other (Fig. 6). This mechanism dampens the interference fringes of the final correlation record $\overline{I}_j$ and gives rise to the coherence aperture, which reduces both numerical aperture of the reconstructed point hologram and the resolution of the image.

The results provided by the nondispersive theoretical model were assessed experimentally in the configurations with a low dispersion sensitivity. In these experiments, the MO Melles Griot ($NA_0 = 0.28$, $f_0 = 20$ mm), the spherical signal wave ($f_s = 400$ mm) and a plane reference wave were used, while the CCD position was varied. The effects caused by the reduced temporal coherence were examined using both the point correlation records and the reconstructions of the USAF resolution target. The experimental results are presented in Fig. 7. The point correlation records captured at the CCD position
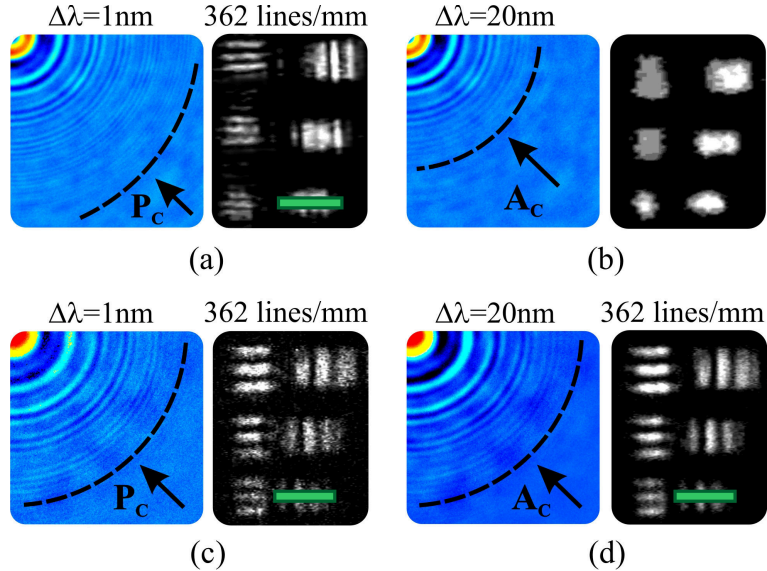


**Figure 7:** Image of the USAF resolution target reconstructed from monochromatic ($\Delta\lambda = 1$ nm) and broadband ($\Delta\lambda = 20$ nm) correlation records captured in the setup optimized for (a),(b) monochromatic and (c),(d) broadband light. The quality of the monochromatic image (c) is maintained even in the broadband image (d), provided the experimental system is optimally adjusted.

optimal for monochromatic light ($\Delta_2 = 800$ mm) are shown in Figs. 7a,b. When nearly monochromatic light was used ($\Delta\lambda = 1$ nm), the correlation record with interference oscillations apparent in the entire overlapping area of the signal and reference beams was obtained (area $P_c$ in Fig. 7a). When a broader spectral filter was used ($\Delta\lambda = 20$ nm), the interference fringes were strongly damped due to the partial temporal coherence of light. The interference pattern then emerged only in a significantly reduced area defined by the coherence aperture (area $A_c$ in Fig. 7b). Reduction of the hologram aperture due to the partial temporal coherence resulted in a deterioration of the image resolution. As is evident, the image of the resolution target reconstructed with $\Delta\lambda = 20$ nm

(Fig. 7b) is significantly degraded compared to the snapshot obtained for $\Delta\lambda = 1$ nm (Fig. 7a). By the theoretical nondispersive model, an optimal CCD position can be found provided the spectral bandwidth of light is specified. For $\Delta\lambda = 20$ nm, the CCD position $\Delta_2 = 1650$ mm was determined. In this setting, the optical path difference is almost zero so that the coherence aperture is extended to the same area as in the monochromatic light (area $A_c$ in Fig. 7d). In this case, the image quality of the resolution target achieved in monochromatic light ($\Delta\lambda = 1$ nm, Fig. 7c) is preserved also in broadband light ($\Delta\lambda = 20$ nm, Fig. 7d).

## 5.2. Spiral and Bessel beam imaging

A significant part of the doctoral thesis is focused on the development of holographic microscopy and methods of advanced imaging based on the recent discoveries of singular and nondiffracting optics. A spatial attention was devoted to optical vortices and non-diffracting Bessel beams that were deployed in techniques of the correlation imaging and digital holography. In the developed methods, the optical vortices and the nondiffracting beams were implemented by the SLM or established numerically by advanced data processing. The vortex phase structures and the self-imaging effects of nondiffracting beams were optimized in imaging applications and applied to the edge contrast enhancement in the spiral incoherent correlation imaging and utilized for three-dimensional localization of microscopic objects by the DH PSF.

### 5.2.1. Edge enhancement in spiral correlation imaging

The spiral imaging is a novel technique of microscopy utilizing optical vortices for the edge contrast enhancement of weakly scattering specimens [63]. The spiral microscopy is inherently sensitive to phase gradients and reminds the Nomarski phase contrast imaging by common characteristics. In the spiral imaging, the contrast enhancement is achieved by interference of optical vortices representing images of individual object points, so that spatially coherent light is required.

In [16], the principles of the spiral microscopy were successfully implemented in the correlation holographic imaging, working with spatially incoherent light. The method benefited from a hybrid coherence regime of the correlation imaging, in which the incoherently recorded holograms were coherently reconstructed [13]. By interference of optical vortices with the helical wavefront, the anisotropic edge contrast enhancement of three-dimensional amplitude objects was successfully realized [16]. The optical vortices utilized in the spiral correlation imaging can be implemented either optically or digitally.

In optical implementation of the spiral correlation imaging, the individual point holograms are created by interference of the spherical signal wave and the vortex reference wave. The waves are created by the SLM in the standard optical arrangement shown in Fig. 3. The modulation function displayed on the SLM is still given by (1) but a spiral phase is imposed on the reference wave,

$$t_j = T_s \exp(i\theta_j) + T_r \exp(il\varphi), \quad j = 1, 2, 3, \tag{13}$$

where $l$ is integer called the topological charge and $\varphi$ denotes the azimuthal cylindrical coordinate. To achieve the best lateral resolution, the topological charge $l = 1$ is used in experiments. By interference of the phase-shifted spherical signal waves with the vortex

reference wave, three spiral patterns shown in Fig. 9b are created for each point of a three-dimensional object. By processing the point spiral records, the vortex hologram representing a virtual diffractive lens with the helical phase is obtained [13,16]. Reconstruction of the point vortex hologram is performed by the Fresnel transform. Instead of the Airy pattern appearing in the standard correlation imaging, the vortex image is created, whose complex amplitude $u'_v$ can be expressed by the Bessel function of the first kind and $l$-th order,

$$u'_v(r') \propto J_l(r') \exp(il\varphi'), \tag{14}$$

where $(r', \varphi')$ are the cylindrical coordinates and the axial object point was assumed for simplicity.
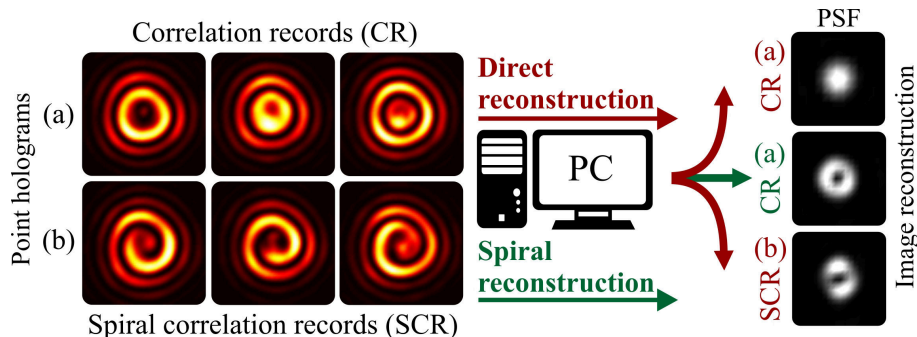
In the digital implementation of the spiral correlation imaging, the vortex PSF (14) is obtained by a spiral reconstruction of the standard records created by the interference of spherical waves. The spiral reconstruction consists of two independent steps. In the first step, the standard hologram reconstruction is carried out providing the complex amplitude $u'$ of the point image. In the following processing, the spatial spectrum of the image is modulated by a spiral phase mask in a virtual 4-f Fourier system. The process can be symbolically written as $u'_v = \text{iFT}\{\exp(il\varphi) \cdot \text{FT}(u')\}$, where FT and iFT denote the direct and inverse Fourier transform, respectively.
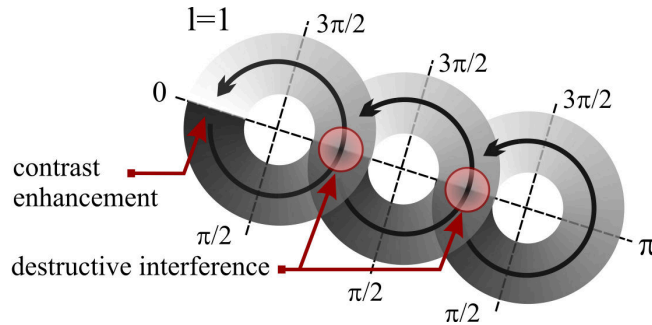


**Figure 8:** Principle of the edge contrast enhancement in the spiral correlation imaging. The edge enhancement is achieved by a destructive interference of the vortex PSFs appearing at the areas, where the object transparency is homogenous.

The point images (14) representing the vortex PSF are created for each point of the recorded object. In the isoplanatic area, the resulting image is obtained as a convolution of the vortex PSF and the transparency function of the object. By a destructive interference of the individual vortex images, the edge contrast enhancement is achieved. This effect is illustrated in Fig. 8. When the vortex images with an odd topological charge are created for object points lying in a homogeneously transparent area of the sample, the neighboring vortices acquire a phase difference $l\pi$. It results in their destructive interference and a local darkening of the image. In places of amplitude and phase gradients, the conditions of the destructive vortex interference are disrupted and the bright transition zones appear in the image. In this way, rapid changes in the object transparency are highlighted by a local increase of the image intensity.

Experimental results obtained in the optically and digitally implemented spiral correlation imaging are demonstrated in Fig. 9. In the left panel, the point correlation records CR are shown (row (a)), which were obtained by interference of the spherical signal and

**Figure 9:** Illustration of optical and digital implementation of the spiral correlation imaging. The standard point correlation records CR (top row (a)) can be processed by direct or spiral reconstruction resulting in the Airy pattern (red CR (a) PSF) or the doughnut vortex spot (green CR (a) PSF). The direct reconstruction of the spiral correlation records SCR prepared with a vortex reference wave (bottom row (b)) results in the doughnut vortex image (red SCR (b) PSF).

reference waves. The spiral point correlation records SCR (row (b)) were captured, when the spherical signal wave and the vortex reference wave with the topological charge $l = 1$ were used. The variability of the method is further enhanced by a possibility to apply the direct reconstruction (red arrows) or the spiral reconstruction (green arrow) of the correlation records. When standard point records CR are directly reconstructed, the Airy pattern is obtained (right panel in Fig. 9, red CR (a) PSF). Applying the direct reconstruction algorithm to spiral SCR point records, the doughnut spiral PSF appears (right panel in Fig. 9, red SCR (b) PSF). In this case, the vortex structure was generated optically by a spiral phase modulation of the vortex reference wave. Preferably, the nearly perfect vortex images can be created by the spiral reconstruction of the standard point records CR (right panel in Fig. 9, green CR (a) PSF), providing the edge contrast enhancement digitally. As is obvious, both the standard and spiral correlation imaging can be realized by processing the same experimental data.

Experimental results demonstrating the principle and application potential of the spiral correlation imaging are shown in Figs. 9, 10 and 11. In all experiments, a low aperture MO ($NA_0 = 0.15$, $f_0 = 150$ mm) and the spherical and reference waves with $f_s = 470$ mm and $f_r = 523$ mm were used. Optionally, a helical phase with the topological charge $l = 1$ was imposed on the reference wave. The CCD was fixed at the distance $\Delta_2 = 495$ mm behind the SLM. In Fig. 10, the results of the spiral correlation imaging are compared to the standard images. In the top row, the images of the USAF resolution target are shown, which were obtained by standard correlation imaging (left) and optically (middle) and digitally (right) implemented spiral imaging. In the bottom row, the direct optical image of a flea (left) is compared to the standard correlation image (middle) and the spiral image exhibiting edge contrast enhancement (right).

Modifying basic experiments of spiral microscopy [63], the anisotropic edge contrast enhancement was also demonstrated. It was achieved in several approaches, in which the anisotropic spiral phase mask was implemented [64] or lateral shifting [65] and central phase controlling of the mask [66] were performed. In the doctoral thesis, the anisotropic edge enhancement was successfully verified also in the digitally implemented spiral correlation imaging. The experimental results obtained are presented in Fig. 11, where a blank circular aperture was used as a test object. The snapshots in the top row (from
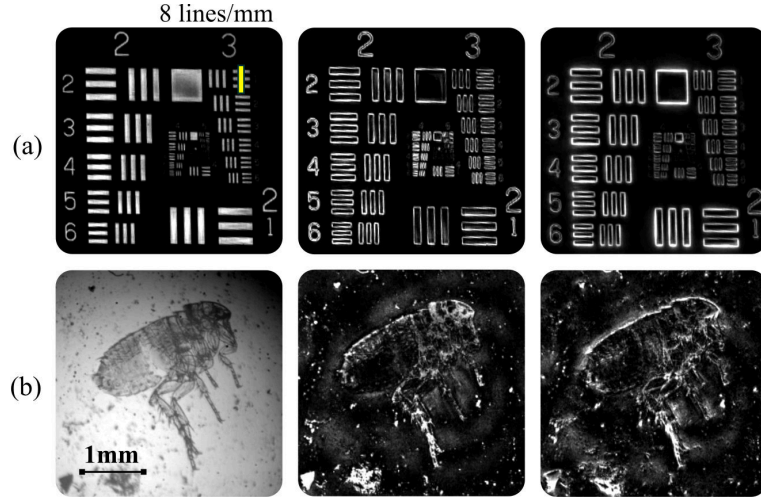
**Figure 10:** Snapshots demonstrating spiral correlation imaging. (a) Images of the USAF resolution target obtained by standard correlation imaging using spherical signal and reference waves (left) and optical (middle) and digital (right) spiral correlation imaging. (b) Images of the flea obtained by optical imaging (left) and standard (middle) and spiral (right) correlation imaging.
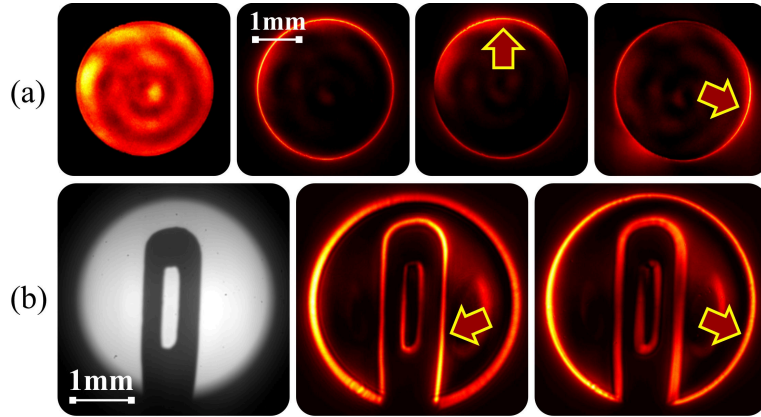


**Figure 11:** Demonstration of the anisotropic three-dimensional spiral correlation imaging. (a) Images of a circular aperture (from left to right): standard correlation imaging, isotropic edge contrast enhancement, anisotropic edge contrast enhancement in two different directions indicated by arrows. (b) Edge contrast enhancement in three-dimensional spiral imaging demonstrated by a needle placed in front of the circular aperture (from left to right): optical image, needle in focus, circular aperture in focus.

left to right) demonstrate the standard reconstruction of the aperture, the isotropic edge contrast enhancement and the anisotropic edge enhancement performed in two different directions (preferred directions indicated by arrows).

A successful combination of the correlation holography with the spiral imaging allowed the first demonstration of the edge contrast enhancement in three-dimensional imaging [16]. Results of the experiment are shown in the bottom row of Fig. 11. As a simple three-dimensional object, a needle placed in front of a circular aperture was used. A direct optical image (left) is compared to the snapshots demonstrating the edge contrast enhancement in the images, where the needle (middle) and the aperture (right)

are in focus. The refocusing indicated by arrows was achieved by processing the same correlations records.

### 5.2.2. Axial localization by rotating Bessel beams

Bessel beams are best known nondiffracting beams called by the function describing their lateral profile. Their intrinsic properties provide a wide variety of unique effects, such as self-imaging and self-healing, which were utilized in multitude of applications including light-sheet microscopy [38–40], optical coherence tomography [99] or optical trapping [56–58]. In enumerated applications, the nondiffracting Bessel beams are deployed exclusively in illumination part of the imaging systems. Recently, the methods of Bessel beam microscopy [68] and interferometry [100] emerged, paving a way for new imaging and metrological applications of nondiffracting effects. The doctoral thesis complements these methods by the nondiffracting vortex imaging working with a rotating PSF, which is suitable for a precise axial localization and tracking of particles. The experiments of three-dimensional localization are important for both biophotonic research and engineering, where enable either cell tracking and observation of cell cycles [101] or applications in microfluidics and particle image velocimetry [102].

The methods of axial localization and tracking of particles were thoroughly studied in the last decade and several techniques providing a full volume information about observed samples were proposed. In optical microscopy, an astigmatic imaging was successfully deployed [103]. By the astigmatic PSF, the objects located in front and behind the best focus plane can be recognized and their axial position determined by processing the defocused images [103,104]. In advanced experiments, a vortex imaging was advantageously utilized, in which the depth information was determined from a defocusing rotation of the PSF [69]. In most localization experiments, the DH PSF is used. Its intensity spot is composed of two bright lobes, whose angular position is changed during defocusing. Recently, various modifications of the basic experiment of the rotating imaging [69] emerged, employing both radial and azimuthal sampling of a spiral phase mask [71–73]. The axial localization by the DH PSF has become a significant technique, which allowed the superresolution imaging in three-dimensional fluorescence microscopy [74].

Digital holographic microscopy has also been successfully applied to single particle localization and tracking [105]. Utilizing the benefits of digital holography, some limitations of the optical rotating imaging were exceeded. In the rotating lens imaging, particle localization is possible only in a narrow region given by the depth of focus of the MO. In techniques of digital holography, a three-dimensional image is numerically reconstructed from a two dimensional holographic record. Therefore, the particles distributed throughout the volume can be localized by the single CCD snapshot. Because the holographic reconstruction does not result in a true three-dimensional image, the reconstructed signal must be further processed to obtain precise positions of the individual particles. In recent years, different algorithms were proposed for analysis of the microparticle holograms. In common implementations, the holographic records are successively reconstructed in a number of planes, being placed repeatedly with a small step behind the hologram. In the next stage, the algorithms based on peak searching [106], quantification of the image sharpness [107], deconvolution [108] or inverse problem approach [109,110] are applied to determine the positions of the recorded objects. Unfortunately, these approaches

suffer from various constraints, such as weak depth accuracy and time-consuming operation [109,110].

**Rotating vortex imaging in digital holography**

In the doctoral thesis, the original methods of the axial localization were developed, in which the benefits of the conventional optical and holographic techniques were utilized and their drawbacks eliminated. Particularly, the localization range was significantly extended compared to the optical rotating imaging by exploiting the principles of digital holography. In addition, multiple reconstructions previously used in the holographic methods were eliminated in the proposed holographic vortex imaging. Here, the axial positions of all point emitters of a volume sample were determined by the angular rotation of their asymmetrical images provided by a single hologram reconstruction. Two digitally based techniques were proposed for generation of the rotating DH PSF. In both methods, the nondiffracting Bessel beams were utilized. By exploiting the complex amplitude instead of the intensity, the required rotational asymmetry of the vortex point images was achieved even in a single nondiffracting beam [18]. In an alternative method, a superposition of two or more nondiffracting beams was created during the spiral reconstruction of standard holograms [17]. Due to the interference of the nondiffracting beams, the DH PSF was implemented, whose rotation can be utilized for the axial localization of point-like objects. The localization methods developed in the doctoral thesis impose no special demands on the optical systems used. They can be implemented by purely digital tools without technical modification of the conventional experiments of digital holography, working with both spatially coherent and incoherent light.
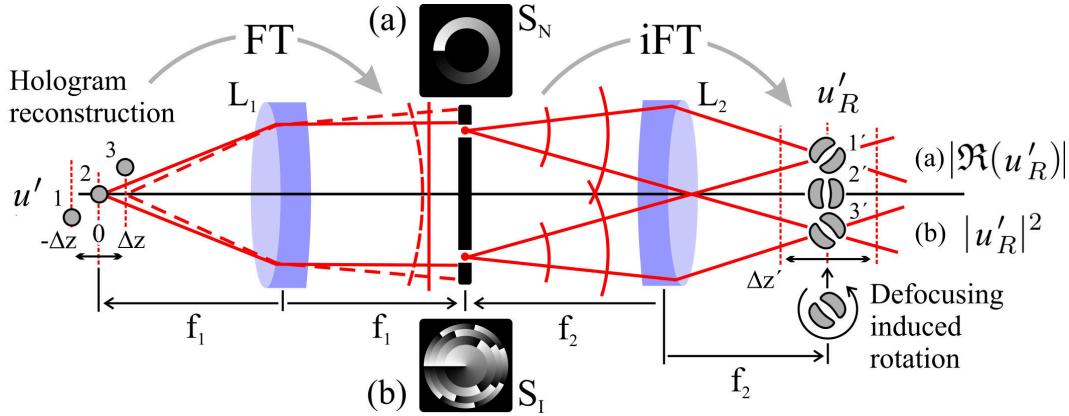


**Figure 12:** Implementation of the rotating DH PSF in methods of digital holography and correlation imaging. Spatial spectrum of the reconstructed image is digitally modulated in a virtual 4-f system composed of lenses $L_1$ and $L_2$. By the spiral phase modulation, single nondiffracting vortex beam (a) or superposition of nondiffracting vortex modes (b) are created, providing the asymmetrical rotating point images either in the complex amplitude $|\Re\{u'_R\}|$ or the image intensity $|u'_R|^2$.

The digital implementation of the rotating DH PSF is obvious from Fig. 12 illustrating virtual optical system used in the post-processing of standard holographic images [17,18]. The complex amplitude of the image obtained by the hologram reconstruction is further processed by the Fourier transform. In optical analogy shown in Fig. 12, the holographic image is placed near the front focal plane of the virtual Fourier lens $L_1$. Behind the

Fourier transforming lens, the digital spiral filter is applied to the spatial spectrum of the holographic image. When the digital filter $S_N$ is used and the inverse Fourier transform performed by the virtual lens $L_2$, single nondiffracting beam is generated, whose intensity spot has a rotational symmetry. Because the reconstruction is carried out digitally, the real part of the complex amplitude providing an asymmetrical beam spot is advantageously processed (Fig. 12a). Alternatively, the DH PSF can be introduced employing the spiral filter of more complex topology, $S_I$. In this case, a superposition of the nondiffracting modes is created behind the lens $L_2$. Provided the convenient parameters of the filter are used, the nondiffracting modes cooperate properly in the image plane and the rotating DH PSF is created by their interference (Fig. 12b). The complex amplitude of the rotating image produced by the single vortex beam or the superposition of vortices can be written in the same form,

$$u'_R = \mathrm{iFT}\{S_j \cdot \mathrm{FT}(u')\}, \quad j = I, N, \tag{15}$$

where $u'$ is a complex amplitude of the standard hologram reconstruction and $S_j$ denotes transparency of the spiral masks used for generation of the vortex modes.

**Rotating imaging with single nondiffracting vortex beam**

In the numerical extension of the standard holographic reconstruction, the axial localization is achieved by rotation of a single nondiffracting vortex beam caused by defocusing in the object space. The vortex beam is generated by the spiral phase modulation performed by a thin annular digital filter placed at the intermediate plane of the virtual 4-f system (Fig. 12a). In simplifying calculations demonstrating principle of the method, the transparency of the spiral filter can be written by the Dirac delta function

$$S_N = \delta(F - F_0)\exp(il\varphi), \tag{16}$$

where $(F, \varphi)$ are the cylindrical coordinates at the Fourier plane, $F_0$ is the radius of the thin annular filter and $l$ denotes the topological charge of the spiral phase modulation. Substituting (16) into (15) and using $u'$ related to the axial object point, the complex amplitude of the rotating image is obtained as

$$u'_R \propto J_l \exp(il\varphi' + i\Phi). \tag{17}$$

Equation (17) has a formal analogy with the single nondiffracting vortex beam, whose intensity spot remains invariant under defocusing. The phase changes with the defocusing shift in the object space $\Delta z_0$ through the term $\Phi \equiv \Phi(\Delta z_0)$. To determine the position of the point object, an asymmetrical image must be created, whose angular rotation indicates the defocusing shift $\Delta z_0$. The required asymmetry is not available in the intensity but in the real part of the complex amplitude $u'_R$. In order to work with positive values, the absolute value of the real part is used,

$$\left|\Re(u'_R)\right| \propto \left|J_l \cos(l\varphi' + \Phi)\right|. \tag{18}$$

The image spot (18) is obtained by multiplying the symmetrical Bessel function of the first kind and $l$-th order by the cosine function depending on the defocusing. As a result, the doughnut profile determined by the Bessel function with the azimuthal cosine modulation

is obtained. In the azimuthal direction, $2l$ bright maxima appear, whose angular position changes due to the object space defocusing $\Delta z_0$. A continuous change of position of the point object thus leads to the rotation of its image. By evaluating the angular rotation of the image, the position of the corresponding point object is determined with the high accuracy. In experiments, the topological charge $l = 1$ is most widely used providing a two-lobe image corresponding to the DH PSF.
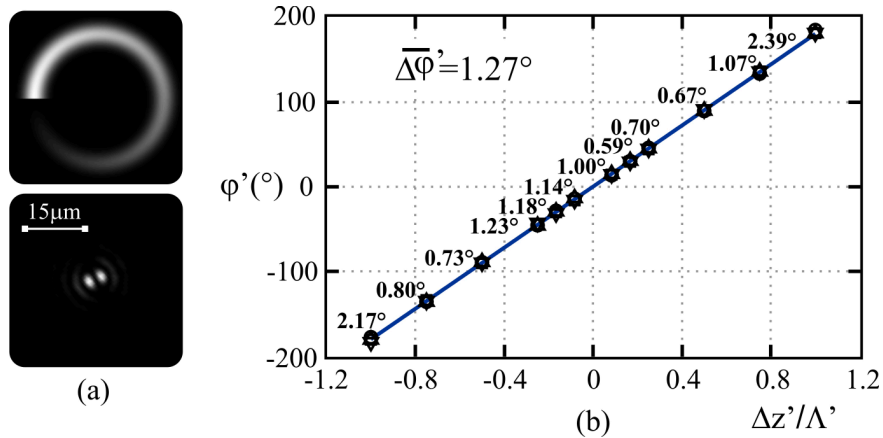


**Figure 13:** Experimental results of the axial localization using single nondiffracting vortex beam. (a) Spiral mask with $l = 1$ (top) and the numerically implemented DH PSF (bottom), created from the real part of the beam complex amplitude. (b) Evaluation of the localization accuracy $\overline{\Delta\varphi}'$ in the axial range $\langle -\Lambda', \Lambda' \rangle$ given by the rotation period $\Lambda'$ of the DH PSF.

In the experiments, both accuracy and applicability of the proposed method were examined, using a single mode optical fiber and polystyrene and fluorescent beads as samples. The accuracy of the method was tested with the single mode optical fiber used as a point-like object. The optical fiber was placed in front of the MO Olympus ($NA_0 = 0.25$, $f_0 = 18$ mm), while the point hologram was captured in the recording configuration with plane reference and spherical signal waves ($f_r \to \infty$, $f_s = 400$ mm) and the CCD at the position $\Delta_2 = 600$ mm. The DH PSF was created digitally using the spiral phase filter with $l = 1$. The dependence of the rotation angle of the DH PSF on the relative defocusing $\Delta z'/\Lambda'$ was measured using successive reconstructions of the point hologram at the different depths. Here, $\Delta z'$ represents the image space defocusing and $\Lambda'$ is the rotation period of the DH PSF. The spiral phase mask and experimentally created DH PSF are shown in Fig. 13a. Comparison of the measured angular rotation with its theoretical values is presented in Fig. 13b. The experiment was evaluated using a standard deviation of the measured rotation angle $\overline{\Delta\varphi}$. By processing the measured data, the standard deviation $\overline{\Delta\varphi} = 1.27°$ was obtained. For the used numerical aperture $NA_0 = 0.25$ and the determined standard deviation of angle evaluation $\overline{\Delta\varphi}$, the accuracy of the axial localization 1 $\mu$m was estimated.

Applicability of the method was assessed in a modified configuration, where the MO Melles Griot ($NA_0 = 0.55$, $f_0 = 4$ mm) was utilized. As the point objects to be localized, the fluorescent and polystyrene beads were used. In the fluorescence experiment, the fixed fluorescent beads (Invitrogen, diameter 5 $\mu$m) were defocused by a precisely controlled displacement and the expected image rotation was examined. In the advanced experiments, the axial localization and particle tracking were tested. The polystyrene beads (diameter
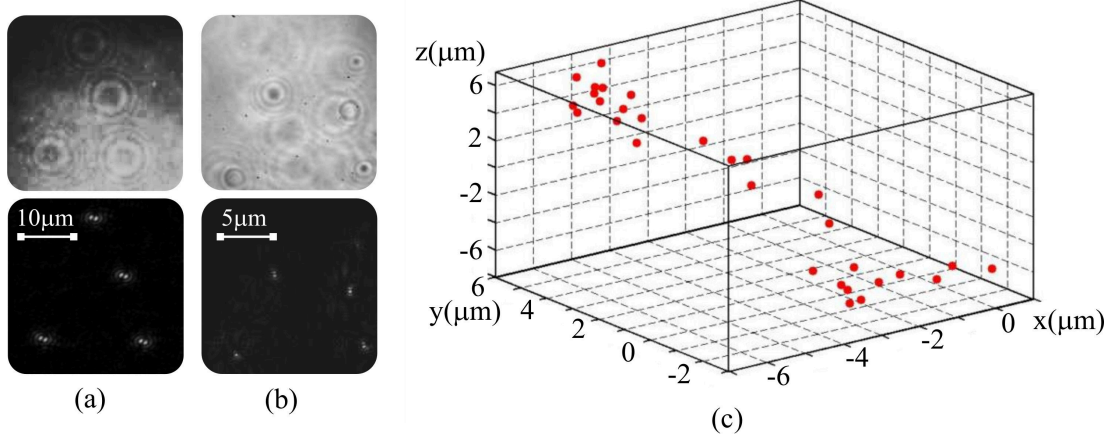
**Figure 14:** Three-dimensional localization and tracking of microscopic particles based on the rotation of a single nondiffracting vortex beam. (a) Hologram of fixed 5 $\mu$m fluorescent beads (top) and its reconstruction providing the DH PSFs of the individual beads (bottom). (b) The same as in (a) but for 0.5 $\mu$m polystyrene beads moving by Brownian motion. (c) Three-dimensional trajectory of a selected polystyrene bead. Individual positions were reconstructed from holograms recorded with the frame frequency 10 Hz.

0.5 $\mu$m) moving by the Brownian motion were used as sample and the holograms recorded on the CCD. The holograms and their reconstructions providing the DH PSFs for individual beads are shown in Figs. 14a,b. In the experiment with the polystyrene beads, the rotation of the DH PSF was utilized for a precise axial localization and tracking of a selected particle. As the result, the trajectory of the selected polystyrene bead was created, with the accuracy in unites of micrometers in all three dimensions (Fig. 14c). Individual holograms contributing to the particle tracking experiment were captured with the frame frequency 10 Hz.

**Self-imaging of nondiffracting vortices in digital holography**

Axial localization of the particles can also be accomplished by intensity processing of the reconstructed vortex image. In this case, two or more vortex beams are required, whose interference creates asymmetrical image rotating under defocusing. A superposition of optical vortices provides new options, which can be utilized in complex and innovative techniques of the PSF engineering. A cooperation of the nondiffracting vortex beams resulting into the effect known as self-imaging can be extremely advantageous for the localization experiments. In order to achieve the self-imaging, the special spiral mask is used in a virtual 4-f system during post-processing of the standardly reconstructed image (Fig. 12b). The transparency of the spiral mask can be written as

$$S_I(F, \varphi) = \begin{cases} \sum_{n=1}^{N} \exp(il_n\varphi), \text{ for } R\sqrt{\frac{n-1}{N}} < F < R\sqrt{\frac{n}{N}}, \ n = 1, 2, ...N, \\ 0, \text{ for } F > R, \end{cases} \tag{19}$$

where $(F, \varphi)$ are the cylindrical coordinates at the focal plane of the lens $L_1$ and $R$ is the maximal radius of the mask. The radius of the mask is divided into $N$ radial zones, where the spiral phase modulation with the topological charge $l_n$ assigned to the $n$-th zone is introduced. Substituting (19) into (15), the complex amplitude of the rotating image $u_R'$

is obtained, corresponding to a coherent superposition of the individual nondiffracting vortex modes

$$u'_R \propto \sum_{n=1}^{N} J_{l_n} \exp(il_n \varphi' + i\Phi_n), \tag{20}$$

where $J_{l_n}$ is the Bessel function of the first kind and $l_n$-th order and $\Phi_n \equiv \Phi_n(\Delta z_0)$ is a phase factor depending on the object space defocusing $\Delta z_0$. By calculating the image intensity $I'_R = |u'_R|^2$ using (20), the rotating PSF is obtained,

$$I'_R = \sum_{n=1}^{N} J_{l_n}^2 + 2 \sum_{n=1, n<n'}^{N} \sum_{n'=n+1}^{N} J_{l_n} J_{l_{n'}} \cos(\Omega_{n,n'}), \tag{21}$$

where

$$\Omega_{n,n'} = [(l_n - l'_n)\varphi' + (\Phi_n - \Phi'_n)]. \tag{22}$$

The total intensity $I'_R$ is composed of the annular intensity spots of the individual vortex beams given by $J_{l_n}^2$ and the interference terms depending on the phase factors $\Omega_{n,n'}$. The symmetrical annular spots are azimuthally modulated by the cosine functions creating bright maxima. Since the cosine arguments depend on $\Delta z_0$ through $\Phi_n$, the bright maxima rotate along the rings, if defocusing occurs in the object space. The total azimuthal modulation of the rings arises due to cooperation of many interference terms, created by the pairs of interfering beams with the indices $n$ and $n'$. Thus, the image rotation is applicable to the axial localization only when the individual interference patterns rotate with the same angular velocity. Under these conditions, a rigid rotation of the resulting azimuthally modulated image is guaranteed. The rigid rotation of the image is inherently achieved provided the parameters of the nondiffracting vortex beams satisfy the self-imaging condition and the topological charge of the $n$-th vortex mode is given by $l_n = l_0 + n\Delta l$, where $l_0$ is an arbitrary integer and $\Delta l = l_{n+1} - l_n$ denotes the difference of the topological charges between two neighboring modes. In the design of the spiral mask (19), the modulation areas are divided into Fresnel zones generating nondiffracting beams, whose interference results in the self-imaging effect. The number of the zones $N$ together with $l_0$ and $\Delta l$ can be used as free parameters enabling shaping of the image spot and controlling the angular velocity of the image rotation caused by the defocusing.

The self-imaging is a well known effect accompanying propagation and interference of the nondiffracting beams [3]. Conventionally, the self-imaging manifests itself by a repeated reconstruction of the lateral profile of the light field during its free-space propagation. In the proposed method of the axial localization, the phase of nondiffracting modes is changed by the object space defocusing instead of the free-space propagation. It results in the defocusing induced self-imaging occurring at a fixed CCD plane. In this case, the self-imaging is externally manifested by the angular rotation of an asymmetrical image spot.

The proposed method was assessed experimentally in the system for incoherent correlation imaging. Experiments were performed in the setup using the MO Melles Griot ($NA_0 = 0.28$, $f_0 = 20$ mm), plane reference and spherical signal waves ($f_r \to \infty$, $f_s = 750$ mm) and a CCD at the position $\Delta_2 = 950$ mm. The point-like source was substituted by a single mode optical fiber, while the rotating PSFs were created by the
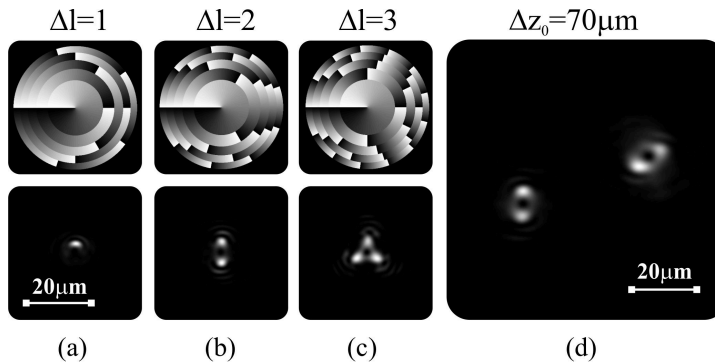
**Figure 15:** Experimental demonstration of the axial localization in the incoherent correlation imaging with the rotating PSF obtained by the self-imaging of nondiffracting vortex modes. Spiral mask (top) and reconstructed PSF (bottom) for the superposition of $N = 5$ vortex modes and the difference of the topological charges (a) $\Delta l = 1$, (b) $\Delta l = 2$ and (c) $\Delta l = 3$. (d) Determination of the mutual axial distance of two point sources ($\Delta z_0 = 70$ $\mu$m) from the relative angular rotation of the DH PSFs.

spiral masks with the parameters $N = 5$, $l_0 = 0, -1, -2$ and $\Delta l = 1, 2, 3$, respectively. Results obtained are presented in Fig. 15. When the mask with $\Delta l = 1$ was applied, a single-lobe corkscrew PSF was obtained (Fig. 15a). The DH PSF and the rotating PSF with three bright lobes were created using the mask with $\Delta l = 2$ and $\Delta l = 3$, respectively (Figs. 15b,c). Defocusing sensitivity of the rotating PSF was tested with the mask $\Delta l = 2$. In the experiment, two point-like sources were separated both laterally and axially and their holograms recorded. During the reconstruction, the DH PSFs with different angular rotations were created depending on the axial positions of the relevant sources. Determining the relative angular rotation of the DH PSFs, the axial separation distance of the point-like sources $\Delta z_0 = 70$ $\mu$m was found (Fig. 15d).

**Self-imaging of nondiffracting vortices in optical microscopy**

In the seminal work called *"Depth from diffracted rotation"*, the defocusing rotation of the PSF was proposed and implemented by interference of Laguerre-Gaussian beams [69]. In the subsequent research, the energy efficiency of the method has been significantly improved [70] and its applicability demonstrated in a variety of experiments. The axial localization technique has even become the basis of the three-dimensional superresolution imaging in fluorescence microscopy [74]. In the ongoing research, new methods for generation of the rotating vortex PSF were proposed based on radial or azimuthal phase sampling of the spiral mask [71–73].

In the doctoral thesis, the radial sampling of the spiral phase mask was applied and new technique of the axial localization proposed, in which a self-imaging of nondiffracting vortices was utilized [17]. Although the original idea was presented as an extension of the holographic imaging, the principle of the method was also successfully applied to optical microscopy. By using the vortex self-imaging, all-optical experiments of the axial localization were proposed. As the main advantages of these methods, a significantly extended working range and resistance against aberrations were demonstrated [20].

Under conditions of optical microscopy, the self-imaging of nondiffracting vortices can be implemented by a complex modulation combining both amplitude and spiral phase modulation. In the experiments designed, the spiral phase modulation can be carried out

either in the spatial spectrum of the object or the intermediate image (Fig. 16). With the selection of the geometrical parameters and topological charges of the nondiffracting beams specified in the previous section, a rigid rotation of the DH PSF is achieved in an extended depth of focus. The spiral phase modulation is applied in a laterally bounded area, so that a high-pass filtering may be performed simultaneously. It results in the contrast enhancement of weakly scattering objects that reminds conditions of the dark-field imaging. Additional benefit of the reduced spectral extent is represented by aberration robustness, which was explored both theoretically and experimentally.
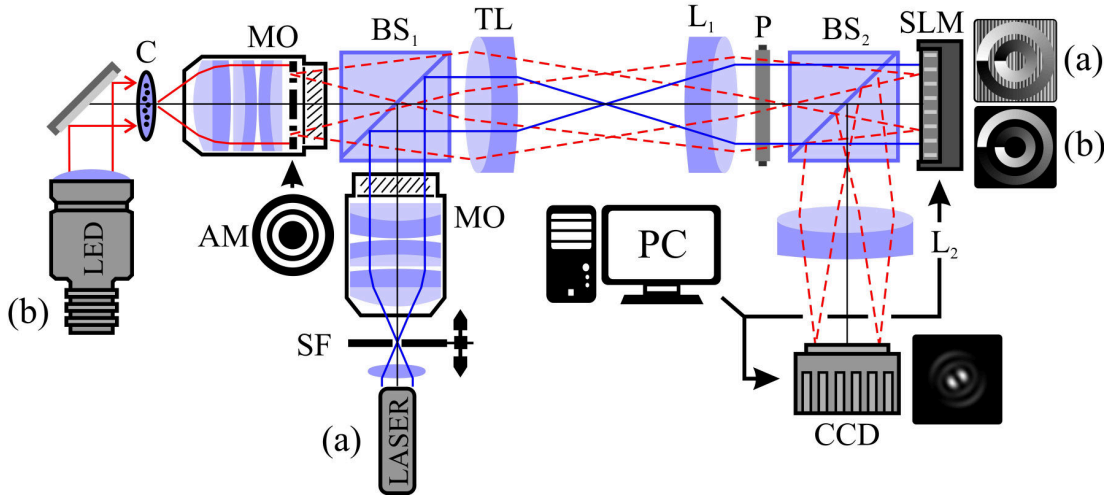


**Figure 16:** All-optical arrangement for the axial localization by vortex self-imaging. (a) Optical path for system adjustment and testing using point source created by a spatial filter SF. (b) Optical path for advanced experiments with polystyrene and fluorescent beads suspended in a glass capillary C. Abbreviations used: MO-microscope objective, AM-amplitude filter, $BS_{1,2}$-beam splitter, P-polarizer, TL-tube lens, $L_{1,2}$-Fourier lenses.

The self-imaging of nondiffracting vortex modes was tested experimentally in the setup shown in Fig. 16. The all-optical system is based on bright-field microscope supplemented by a modular part. The auxiliary module is composed of the 4-f system and the SLM placed at the Fourier plane. The image is formed due to the same spiral modulation that was used in the digital holography to achieve the self-imaging [17,18]. The main difference between both methods consists in performing the spiral modulation. While in the digital holography it was carried out by virtual operations, in all-optical experiment optical waves impinging on an active display of the SLM are modulated. Light coming from the tube lens TL is further transformed by the lens $L_1$ creating the spatial spectrum of the object at the image focal plane. At this plane, the SLM with the transparency given by (19) is placed. In individual zones of the spiral filter displayed on the SLM, a helical phase specified by different topological charges is imposed on passing light. Behind the lens $L_2$, a superposition of nondiffracting vortex modes with the parameters controlled at the separate zones of the mask is created. The rotating PSF then appears due to the self-imaging effect caused by interference of the vortex modes.

Contrary to the previous demonstrations [17], only two modes generated from the mask zones with a varying width were used in the experimental testing. The required complex modulation, including both amplitude and phase modulation, was introduced by two different techniques shown in Figs. 16a,b. In the first approach (Fig. 16a), the phase-

only SLM was used. Since in addition to the spiral phase modulation also the amplitude modulation was necessary, the special CGHs were prepared and displayed on the SLM. Instead of the amplitude attenuation of incident light, a blazed grating was applied in the desired areas of the mask, deflecting light away from the optical path used. Light passing through the areas without grating structure was modulated in phase, captured by the lens $L_2$ and directed towards the CCD. In an alternative approach (Fig. 16b), the complex modulation was introduced in two steps. Using a custom fabricated amplitude filter, the bright nondiffracting modes with $l = 0$ were created at the back focal plane of the MO. Subsequently, the vortex phase was assigned to individual nondiffracting modes by the SLM placed at the plane optically conjugated with the MO pupil. In this case, the SLM was operated in an optimal phase-only regime. In both experimental implementations, the dark-field effect was achieved and working range of the rotating PSF significantly extended, but the energy efficiency was decreased. The energy efficiency can be improved either by extending the width of the annular mask zones or increasing their number. Unfortunately, these changes reduce the benefits of the self-imaging and adversely affect the operating range and resistance to aberrations. The optimization of the experiment then relies on a balance between the energy efficiency and the desired parameters of the axial localization.
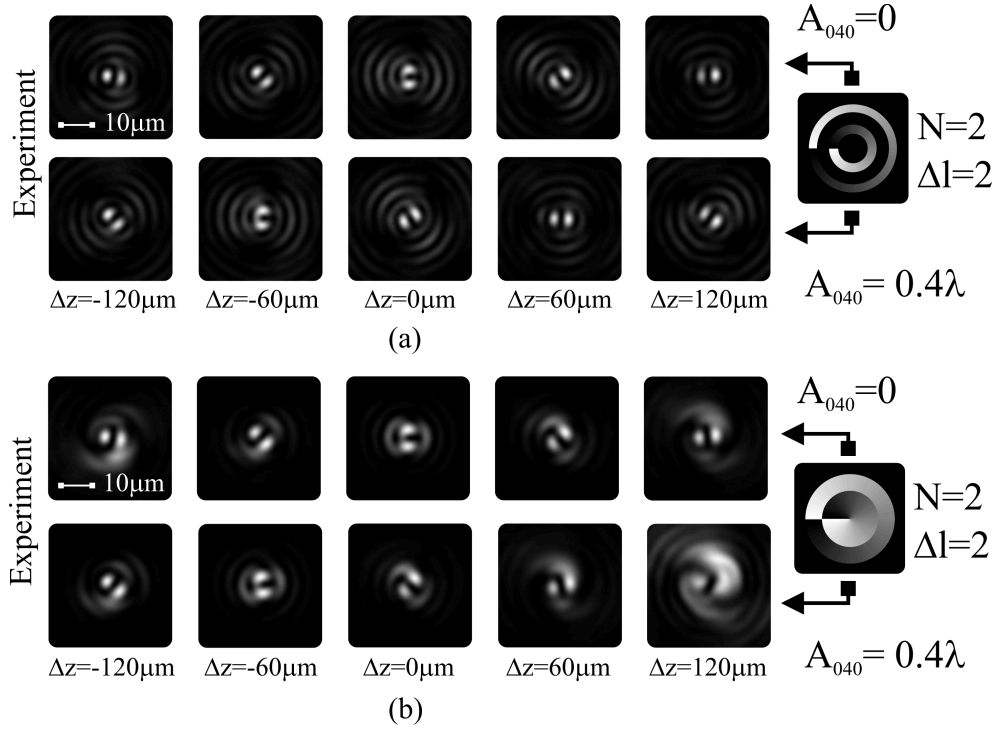


**Figure 17:** Experimental results on all-optical axial localization using two-mode vortex self-imaging. (a) Aberration resistant rotation of the DH PSF realized by the spiral mask with thin annular zones (top row - without aberration, bottom row - spherical aberration $A_{040} = 0.4\lambda$). (b) Aberration deterioration of the DH PSF realized by the spiral mask with two wide zones (top row - without aberration, bottom row - spherical aberration $A_{040} = 0.4\lambda$). In both demonstrations, the object space axial range $\Delta z = \pm 120$ $\mu m$ and the mask parameters $N = 2$ and $\Delta l = 2$ were used.

Extension of the working range and the aberration robustness were tested in the setup shown in Fig. 16a. As a point source, the spatially filtered He-Ne laser was used. Light from the spatial filter SF was collimated by the MO Newport ($NA_0 = 0.4$, $f_0 = 9$ mm) and by the beam splitter $BS_1$ diverted towards the tube lens TL ($f_T = 200$ mm) and the 4-f system composed of the lenses $L_1$ and $L_2$ ($f_1 = 200$ mm, $f_2 = 400$ mm). The phase-only SLM (Hamamatsu X10468-01, 800x600px) was placed at the back focal plane of the lens $L_1$. The spiral mask addressed on the SLM was composed of two thin annular zones with the radii $R_1 = 0.64$ mm and $R_2 = 0.9$ mm, which were modulated by the vortex phase with $l_1 = -1$ and $l_2 = 1$ ($l_0 = -3$, $\Delta l = 2$). To demonstrate the aberration robustness of the axial localization, the third-order spherical aberration $A_{040} = 0.4\lambda$ was added on a defocused wavefront. The aberration was created by the SLM together with the spiral mask, in order to achieve a full control over the wavefront deformation. Results obtained with the thin annular zones ($\Delta R = 0.1$ mm) are presented in Fig. 17a. The rotating DH PSF acquired in the system with well corrected spherical aberration ($A_{040} = 0$) is compared with the case, in which the spherical aberration $A_{040} = 0.4\lambda$ was added by the SLM. In both experiments, the rotation of the DH PSF was monitored within the axial range $\Delta z = \pm 120$ $\mu$m. As is apparent, the shape of the DH PSF is not affected by aberrations and only some additional angular rotation can be observed. Since the rotation remains the same for all depths, aberration effects can be effectively compensated [20]. In Fig. 17b, the annular zones were extended and fully transmitting areas created. It corresponds to a modified polarization encoded corkscrew imaging [73] or optically implemented rotating imaging [17]. When the mask with two fully transmitting zones was used, the self-imaging condition was disrupted and an apparent deformation of the image spot occurred for larger defocusing. It is evident from comparison of the top rows of Figs. 17a and 17b, where the same axial localization range $\Delta z = \pm 120$ $\mu$m was used. As shown in the bottom row of Fig. 17b, the resistance against aberrations was lost in experiment performed with fully transmitting zones of the mask.
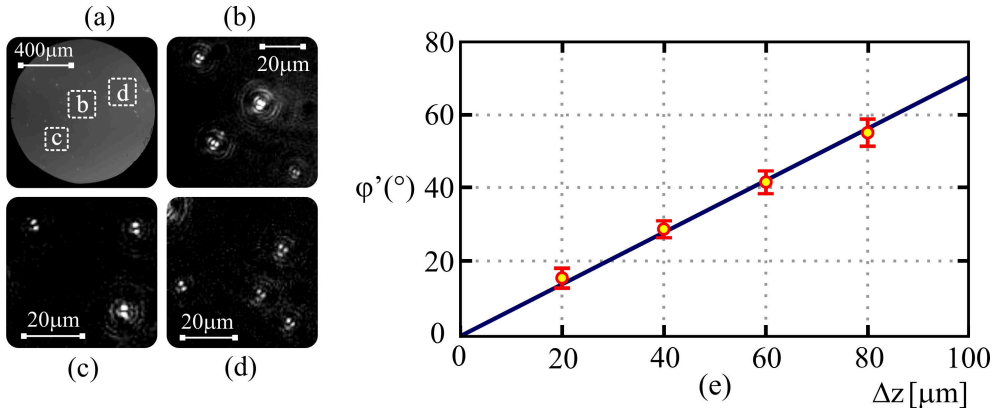


**Figure 18:** Axial localization of polystyrene beads by the rotating DH PSF using two-mode vortex self-imaging. (a) Polystyrene beads (diameter 1 $\mu$m) suspended in a glass capillary tube. (b-d) Angularly rotated images of polystyrene beads in magnified portions of the entire field of view shown in (a). (d) Evaluation of the localization accuracy in the presence of spherical aberration randomly selected from the interval $A_{040} = \in \langle -0.4\lambda, 0.4\lambda \rangle$. The standard deviation at individual positions was determined by processing 40 records made using the spiral mask with two thin annular zones ($N = 2$, $\Delta R = 0.1$ mm) and the topological charges $l_1 = -1$ and $l_2 = 1$ ($l_0 = -3$, $\Delta l = 2$).

A possibility to eliminate the additional image rotation caused by aberrations was further examined using the mask with thin annular zones. In the localization experiments, the spherical aberration randomly selected from the interval $A_{040} \in \langle -0.4\lambda, 0.4\lambda \rangle$ was imposed on the defocused wavefront. Subsequently, the dependence of the rotation angle on the object space defocusing was measured. By processing experimental data, the additional rotations caused by the spherical aberration were eliminated and experimental dependence of the rotation angle on the defocusing compared with a theoretical linear dependence (Fig. 18e). The standard deviations in measured positions were obtained by processing 40 records.

The practical applicability of the method was tested in the experimental configuration shown in Fig. 16b. As the sample, a glass capillary tube with suspended polystyrene beads (diameter 1 $\mu$m) was used. The polystyrene beads moved freely by the Brownian motion and the rotating images were successively recorded on the CCD with a frame frequency 5 Hz. The entire field of view and its magnified portions with the rotating images are shown in Figs. 18a-d.

**Localization microscopy with a spiral wave plate**

Methods of the axial localization are directly applicable to both optical microscopy and digital holography, provided appropriate changes in optical systems or image reconstructions are made. In the optical microscopy, the rotating PSF can be introduced by various methods of spatial light modulation [20,69–73]. Although some advanced applications of these methods were already proposed [73,74], the rotating PSF was generated exclusively by the SLM in all available works, increasing demands on the optical system.
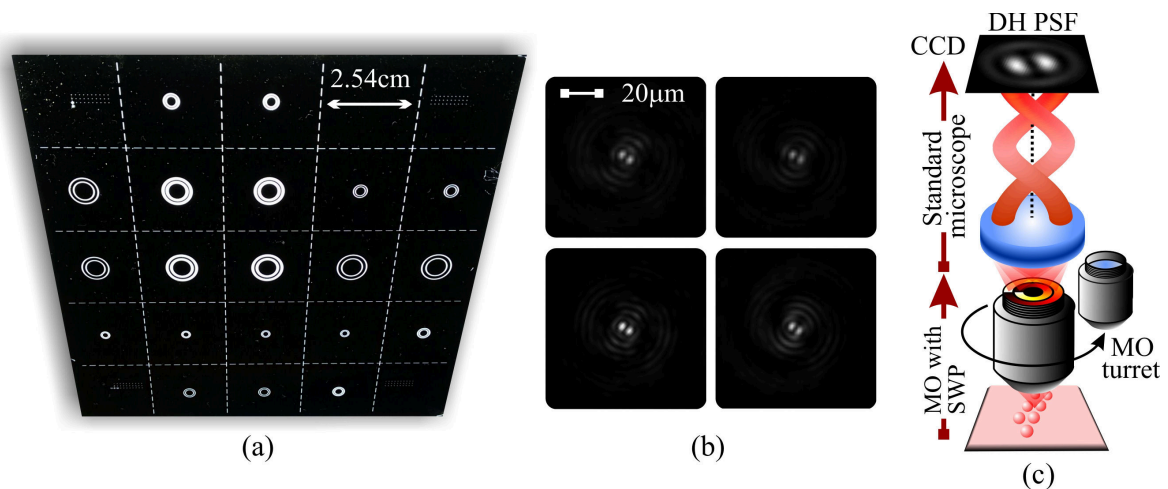


**Figure 19:** Axial localization in standard optical microscope by the SWP replacing operation of the expensive SLM. (a) A snapshot of the lithographic mask fabricated at the ISI Brno. The SWPs with different parameters are regularly spaced over the entire area of the mask. (b) The DH PSFs created by different SWPs from the mask (a). (c) Concept of the rotating imaging in standard microscopy using SWP placed at the exit pupil of the MO.

In the doctoral thesis, the rotating DH PSF has been first created without the use of a SLM, to the best knowledge of the author. In performed experiment, the self-imaging of nondiffracting vortex modes was implemented, using a custom fabricated spiral wave plate

(SWP). The SWP provides simultaneous amplitude and phase modulation and results in a rotating imaging, when employed in the setup similar to Fig. 16. After replacing the SLM by the SWP, system costs are significantly reduced and the localization of particles becomes possible even in standard optical microscope after simple adjustment of the MO. A lithographic mask composed of the SWPs with different parameters is shown in Fig. 19a. The various SWPs were created in subareas of the mask, providing a variability of localization experiments. The individual SWPs were optimized with regard to the operating wavelength, accessible working range and localization accuracy. The lithographic mask was custom fabricated at the ISI Brno. The DH PSFs created by different subareas of the mask are shown in Fig. 19b. In the course of ongoing cooperation with the ISI Brno, the SWPs will be fabricated as compact apodization filters. It will allow an inclusion of the SWP into a back focal plane of the MO, reducing demands on the experimental system. With the modified MO, the rotating DH PSF will be applicable to the standard optical imaging simply by MO turret. Concept of the vortex operation of a standard optical microscope is illustrated in Fig. 19c.

# 6. Outcomes of applied research

In the doctoral thesis, the original imaging concepts of the correlation and holographic microscopy were developed. The proposed methods were examined both theoretically and experimentally. In experiments, up-to-date configurations were used and different adjustments of the systems were assessed under conditions of the potential applications. In experiments carried out both fundamental and technical drawbacks were revealed, that have become a challenge for the further development and enhancement of the techniques being developed. The main achievements can be summarized as follows:

- In the incoherent correlation imaging shown in Fig. 3, fundamental problems restricting the practical usability of the method have been found in experiments performed with the initial setup [84]. In this case, a full overlapping of the signal and reference waves was achieved only for recording of the axial object point. For the off-axis points, the spots of interfering beams were spatially separated on the CCD, so that interference occurred only in a very small field of view. This problem was successfully solved in the setup supported by relay optics [22]. In the modified system, the accessible field of view was significantly enhanced and the optimal resolution retained in the entire recorded area.

- Extremely strong diffractive dispersion preventing utilization of the SLM in broadband imaging was effectively eliminated by an afocal refractive corrector, which was designed, manufactured in Meopta-optika, s.r.o. and tested in the laboratory [23].

- Exploiting the birefringence of liquid crystal molecules, new method of a motionless phase-shifting was proposed and implemented in the polarization adapted Mirau interferometer [21].

- As the main application output benefiting from partial results of the doctoral thesis, a multimodal microscope aided by the SLM technology was designed and realized in the IPE BUT laboratory. The prototype of the microscope has become one of the significant results of the project CDO supported by the TA CR.

## 6.1. Incoherent correlation imaging with extended field of view

In optical microscopy, the field of view is clearly defined by parameters of the MO or field diaphragms, respectively. The situation is more complicated in the incoherent correlation imaging, where the image is not detected directly but reconstructed from point correlation records created by interference of the signal and reference waves. Required interference occurs provided a spatial overlapping of the signal and reference waves at the CCD is achieved. In the previously used setups, a full overlapping was reached only for interfering waves originating from the axial object point. The signal and reference waves obtained by splitting light from off-axis points were spatially separated at the CCD and interference was impossible even in a small portion of the field of view of the MO. Unfavorable spatial separation of the waves was strongly dependent on the parameters of the experiment and has been investigated both theoretically and experimentally. Unfortunately, it was found that the spatial overlapping of waves, and thus also the field of view, were unacceptably reduced just when the system was configured to reach the optimal image resolution. Loss of interference due to the insufficient spatial overlapping of the signal and reference waves

was successfully solved by applying a relay optical system inserted between the MO and the SLM. Using the two-component lens system, the incident light beam was centered on the SLM for any part of the field of view. In this geometry, the optimal modulation of the signal and reference beams has been performed and their spatial overlapping in the entire field of view of the MO intrinsically provided [22]. This significant modification of the setup was used in all subsequent experiments of the incoherent correlation imaging realized in the IPE BUT and UP laboratories and adopted also by other research groups.
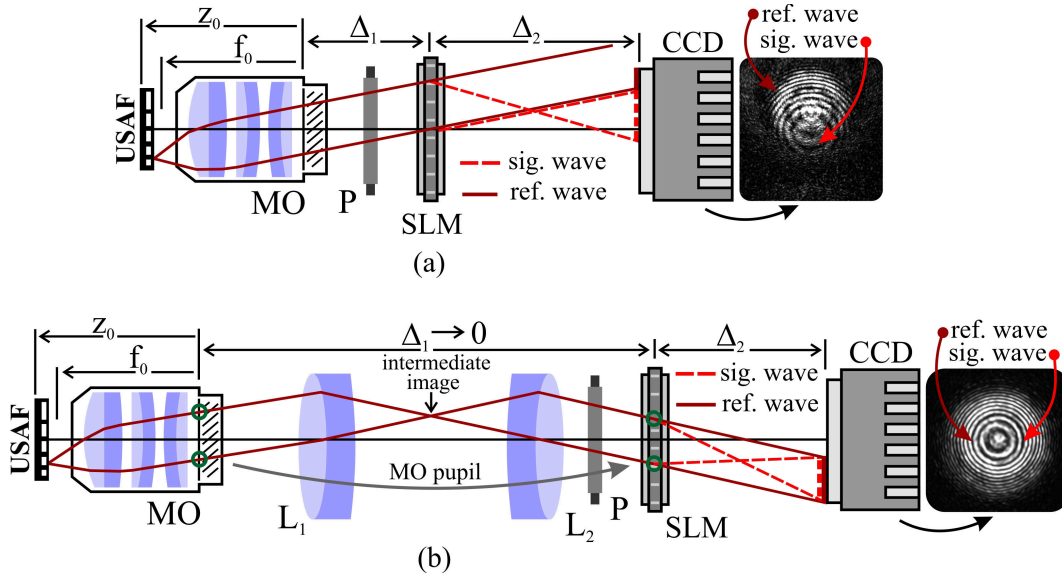


**Figure 20:** Optical arrangements of the incoherent correlation imaging. (a) Original configuration [84] with decreasing overlapping of interfering waves for off-axis points and the strongly reduced accessible field of view. (b) Improved configuration supplemented by the relay optics [22] and providing the perfect overlapping of interfering waves in the entire field of view of the MO.

The previously used system of the incoherent correlation imaging [84] and its modification [22] are compared in Fig. 20, where a plane reference wave is used to simplify demonstration. As is obvious, the paths of rays are completely different in both cases. If the previous experimental configuration Fig. 20a is used, the light beam coming from the off-axis point is laterally shifted at the SLM. Rays of the signal and reference waves created by splitting of the incident beam then have spatially separated paths and the overlapping of their spots on the CCD is not achieved. Since the beam overlapping is continuously reduced with increasing field of view, just only the central part of observed specimen can be recorded successfully. The rays of signal and reference beams illustrated by dashed and solid lines in Fig. 20, respectively, demonstrate a limiting case in which the beam spots are fully separated at the CCD and the point correlation record is not created. If the point object lies closer to the optical axis, the partial overlapping of interfering beams occurs but the point record is corrupted (snapshot in Fig. 20a) and the available resolution deteriorated. As is evident from the ray paths, the spatial separation of the beams at the CCD is a consequence of the lateral displacement of the beam impinging on the SLM. It can be reduced by shortening the distance between the MO and the SLM. The light beam is precisely centered on the SLM provided the condition $\Delta_1 \to 0$ is met, which

requires a close contact of the exit pupil of the MO and the SLM. In experiments carried out with the system Fig. 20a, it is not possible to move the SLM close enough to the MO.

In the modified setup [22], the relay lens system was inserted between the MO and the SLM (Fig. 20b). The lenses $L_1$ and $L_2$ then form a 4-f system adjusted such that the exit pupil of the MO is optically conjugate with the SLM plane. By this way, the unattainable mechanical contact of the MO and the SLM is achieved optically by imaging enabled by the relay lenses. As the ray paths in Fig. 20b show, the input beam is precisely centered on the SLM and the signal and reference beams perfectly overlap on the CCD for all off-axis points of the object. Under these conditions, the hologram recording and image reconstruction in the entire field of view of the MO is possible. In Figs. 20a,b, the transmissive SLM was illustrated to simplify demonstration of the ray paths. In experiments, the reflective SLM with adjacent beamsplitter was used.



(a)          (b)          (c)          (d)
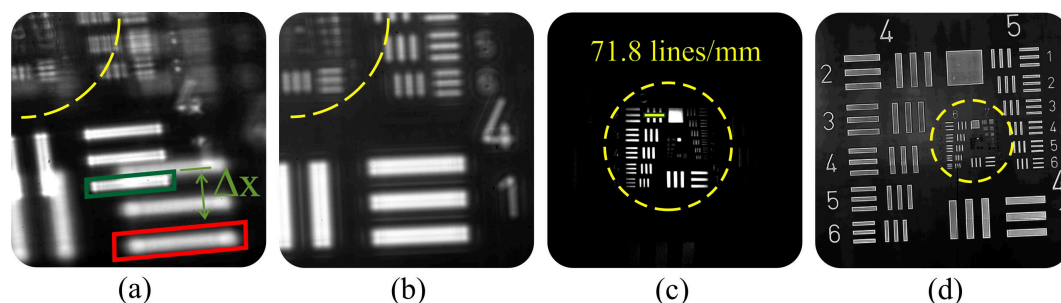
**Figure 21:** The correlation records and the image reconstructions of the USAF resolution target realized in the original setup of the incoherent correlation imaging [84] (a),(c) and the improved system with the relay lenses [22] (b),(d). (a) Corrupted correlation record (system in Fig. 20a) with unacceptable separation $\Delta x$ of signal wave (green box) and reference wave (red box) in peripheral part of the field of view (sufficient overlapping indicated by yellow dashed line). (b) Perfect overlapping of interfering waves in the entire field of view of the MO (system in Fig. 20b). (c) Strongly reduced field of view in the image obtained by the digital reconstruction of the record (a). (d) Full field of view in the image obtained by the digital reconstruction of the record (c). In the reconstructed images (c) and (d), the same areas of the field of view are indicated by the yellow circles.

The proposed configuration [22] was assessed experimentally using the MO Melles Griot ($NA = 0.28$, $f_0 = 20$ mm), the spherical signal and plane reference waves ($f_s = 247.5$ mm, $f_r \rightarrow \infty$) and the separation distance $\Delta_2 = 495$ mm. In experiments without relay lenses, the minimal achievable distance between the MO and the SLM $\Delta_1 = 270$ mm was set. In improved experiments, the 4-f system with two identical relay lenses $L_1$ and $L_2$ ($f = 150$ mm) was applied. In both systems, the holographic records and the image reconstructions were performed to demonstrate progress achieved with the relay optics. Experimental results obtained with the USAF resolution target are shown in Fig. 21. In the records carried out in the original system Fig. 20a, the significant lateral shift between the signal and reference beams was observed ($\Delta x$ in Fig. 21). In accordance with theory, the separation distance $\Delta x$ was increased in the peripheral part of the field of view and sufficient overlapping was achieved only in the circular area denoted by the yellow dashed line. The records of the USAF resolution target shown in Fig. 21b were acquired with the relay lenses so that the perfect correlation overlapping of signal and reference beams was obtained in the entire field of view of the MO. The deteriorated and perfect holographic

records of the USAF resolution target (Figs. 21a,b) were processed numerically and the images were reconstructed. In the setup without relay optics, the image reconstruction was successful in only a small part of the field of view denoted by the yellow dashed line in Figs. 21a,c. The image reconstruction in a significantly enlarged field of view (Fig. 21d) was reached with the record taken using the relay optics (Fig. 21b). Identical parts of the field of view are indicated by the yellow circles in Figs. 21c,d.

## 6.2. Correction of diffractive dispersion in broadband SLM imaging

The SLM is a versatile light shaping device with a multitude of optical applications. However, specific operating conditions have to be respected for an optimal modulation of light. Since the CGHs addressed on the SLM are designed for a single operating wavelength, the narrow spectral bandwidth corresponding to a nearly monochromatic light is required. If the broadband light is used, the operation of the SLM is impaired by the effects caused by both refractive and diffractive dispersion. The dispersion can be monitored in a free-propagation of light transformed by the SLM and its effects depend on the type of phase modulation. The diffractive dispersion prevails over the refractive dispersion of common optical materials and dependence of the refractive index of liquid crystal molecules on the wavelength can be neglected. Problem of the diffractive dispersion was addressed in several previous works and the dispersion effects were successfully compensated for grating patterns with a constant spacing [112,113]. In the doctoral thesis, an attention is focused on the diffractive dispersion accompanying the quadratic phase modulation. The proposed correction technique is important for lens-like SLM applications, including light focusing in both the incoherent correlation imaging and the standard optical imaging with a direct image detection [23].

In the imaging SLM applications, the CGH with the quadratic phase is displayed on the SLM,

$$t(r_m, \lambda_0) \propto \exp\left(i\frac{\pi r_m^2}{\lambda_0 f_0}\right), \tag{23}$$

where $r_m$ is the radial coordinate at the SLM plane and $f_0$ denotes the focal length of the created lens for a design wavelength $\lambda_0$. In real situations, the phase function (23) has to be reduced to the interval $\langle 0, 2\pi \rangle$ due to a limited dynamic range of the SLM. A periodic pattern is created in this procedure so that the SLM operates as a diffractive lens. If the SLM is illuminated by a broadband light with the wavelengths given by the spectral range $\lambda \in \langle \lambda_0 - \Delta\lambda/2, \lambda_0 + \Delta\lambda/2 \rangle$, the complex amplitude of the diffracted monochromatic components has a spatial distribution given by $U'(\mathbf{r}', \lambda) = \mathrm{FrT}_\lambda\{t(r_m, \lambda_0)\}$, where the position vector $\mathbf{r}' \equiv (\mathbf{r}'_\perp, z')$ determines the image space coordinates and FrT denotes the Fresnel transform. The quadratic propagation factor of the Fresnel transform and the phase factor of the lens are mutually fully eliminated just at the distances depending on the wavelength, $z' \equiv z'(\lambda)$. These distances define the planes of perfect focusing and represent the focal lengths of the SLM lens for individual wavelengths,

$$f(\lambda) = z'(\lambda) = \frac{\lambda_0}{\lambda} f_0. \tag{24}$$

The dependence of the focal length $f$ on the wavelength $\lambda$ indicates the chromatic aberration caused by the diffractive dispersion. A change of the optical power $\delta K$ of the SLM
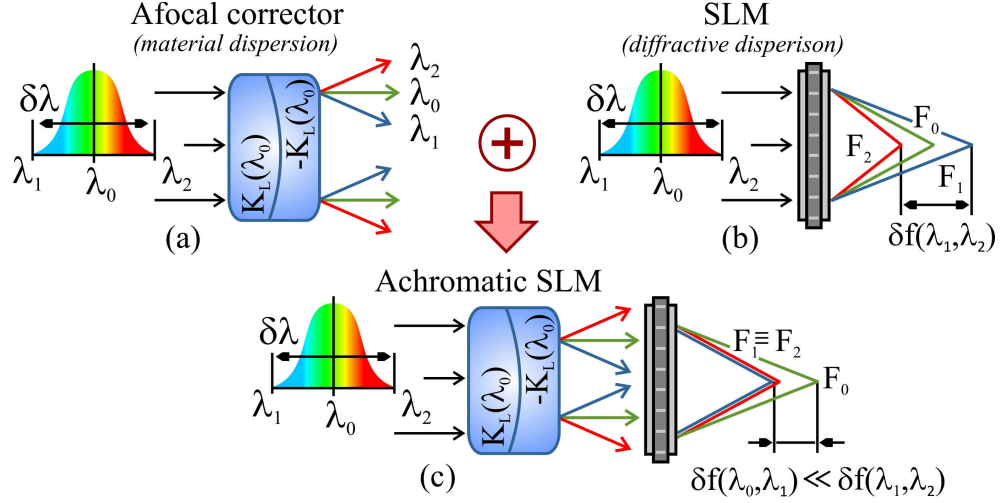
**Figure 22:** The concept of the dispersion compensation of the SLM: (a) material dispersion of the afocal refractive corrector, (b) diffractive dispersion of the SLM and (c) achromatic correction of the SLM [23].

lens in the assumed spectral range can be expressed by the optical power for the central wavelength $K_0$ and the Abbe number $V_D$,

$$\delta K = \frac{K_0}{V_D}, \tag{25}$$

where $V_D = -\lambda_0/\Delta\lambda$. The Abbe number becomes negative for the diffractive dispersion and for the visible spectral range represented by the Fraunhofer lines D, F and C $V_D \approx -3.5$ is obtained. As the value of the Abbe number shows, the diffractive dispersion is extremely strong compared to the material dispersion and their manifestations are reversed. Principle of the proposed achromatic correction of the SLM using afocal refractive system is schematically illustrated in Fig. 22.

The correction is for simplicity discussed for a doublet lens even the system has been realized as more complicated to eliminate the monochromatic aberrations. The corrector was designed as afocal so the performance of the SLM lens was not impaired for the central wavelength $\lambda_0$. For other wavelengths of the spectrum, a non-zero optical power of the corrector was introduced (Fig. 22a) resulting in the refractive chromatic aberration just compensating effects of the diffractive dispersion of the SLM lens. Due to a contradictory effect of the refractive and diffractive dispersion, their mutual compensation is possible, provided the condition of the achromatic imaging is satisfied [23],

$$\frac{1}{V_1} - \frac{1}{V_2} + \frac{1}{\kappa V_D} = 0, \tag{26}$$

where $V_1$ and $V_2$ are the Abbe numbers of the front and rear corrector lenses and $\kappa$ is the ratio of the focal lengths of the SLM lens and the front corrector lens.

Prototype of the achromatic corrector was custom fabricated in the company Meopta-optika, s.r.o. It was designed as a triplet lens providing the achromatic correction of the chromatic focal shift of the SLM lens and an efficient compensation of the monochromatic aberrations. Photograph of the achromatic corrector is shown in Fig. 23 together with the CCD records of a white source acquired with and without corrector. A color fringing
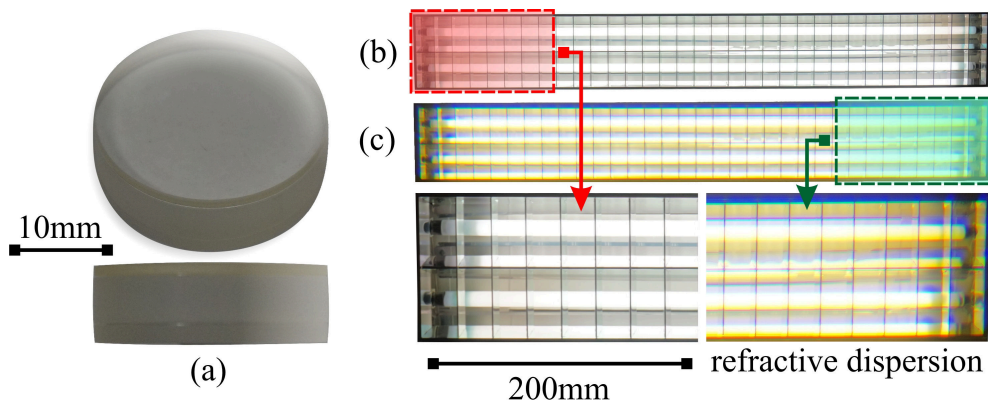
**Figure 23:** Afocal refractive optical system for achromatic correction of diffractive dispersion of the SLM lens. (a) Photograph of the corrector and CCD records of a white light source taken (b) without and (c) with the corrector.
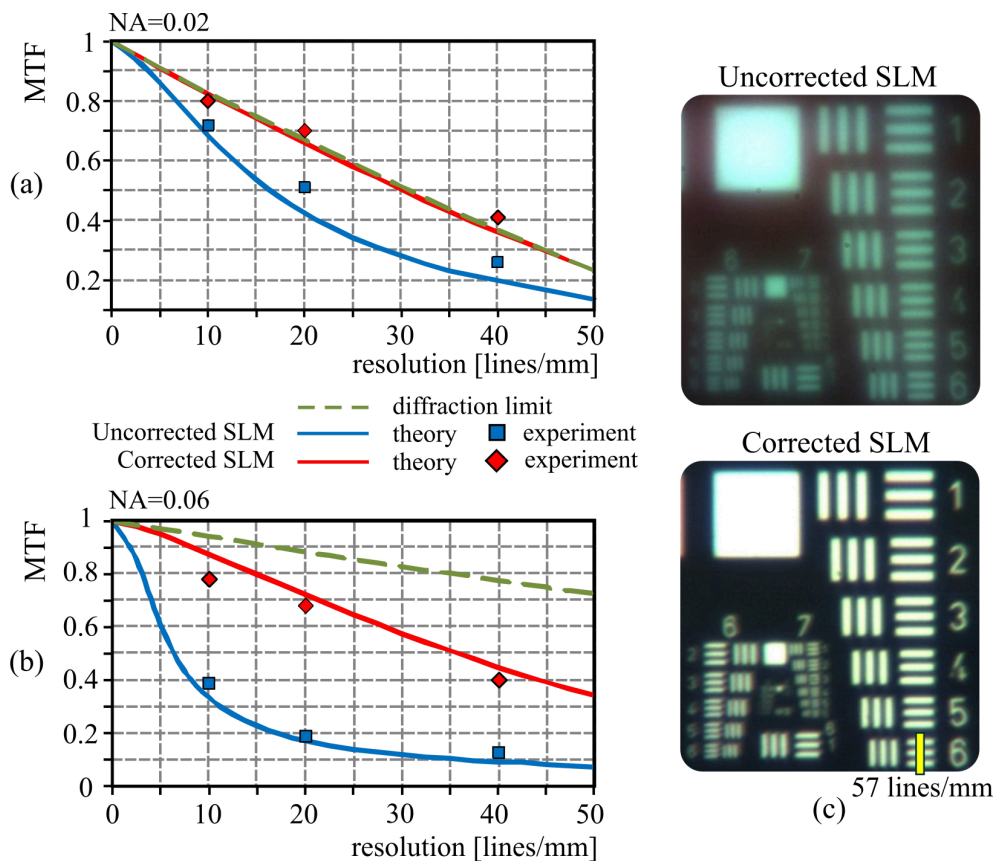


**Figure 24:** Experimental results demonstrating refractive afocal system for achromatic correction of the diffractive SLM lens. Comparison of the calculated and measured MTF (10, 20 and 40 cycles/mm) for the corrected and uncorrected SLM lens with the numerical aperture (a) $NA = 0.02$ and (b) $NA = 0.06$. (c) Snapshots of the USAF resolution target taken in the broadband light ($\lambda_0 = 532$ nm, $\Delta\lambda = 80$ nm): uncorrected SLM lens (top), corrected SLM lens (bottom).

caused by hyperchromatic corrector is evident from Fig. 23c and the snapshot bottom right.

The afocal hyperchromatic corrector was tested experimentally in conjunction with the SLM used as a tube lens in bright-field microscope. Broadband light with the spectral bandwidth $\Delta\lambda = 80$ nm was used to examine the achromatic imaging provided by the system composed of the corrector and the SLM lens (Fig. 24). In order to demonstrate the benefits of the corrector, imaging by the uncorrected SLM lens impaired by a strong diffractive dispersions was also examined. In measurements, the lenses with the numerical aperture $NA = 0.02$ and $NA = 0.06$ were gradually addressed on the SLM. In ray optics measurements, the achromatic correction was verified to be in a good agreement with the theory. The measured secondary spectrum was approximately eight times smaller than the chromatic focal shift of the uncorrected SLM lens [23]. Subsequently, the Modulation Transfer Function (MTF) was measured for both corrected and uncorrected SLM lens. Results of the measurement are demonstrated in Fig. 24a,b and compared with the theoretical MTF calculated by means of the Oslo Premium software. For the low aperture SLM lens with $NA = 0.02$ (Fig. 24a), the diffraction-limited MTF (green dashed line) nearly coincides with the theoretical curve calculated for the achromatic correction (red line). A significant decrease in the MTF calculated for the uncorrected SLM lens is demonstrated by the blue curve. Experimental data obtained for the corrected and uncorrected SLM lens are demonstrated by the red rhombs and blue squares, respectively, and fit well with the related theoretical curves. For numerical aperture $NA = 0.06$ of the SLM lens, the MTF improvement achieved with the corrector is even more pronounced and for the medium spatial frequencies contrast enhancement from 0.2 to 0.7 is reached (Fig. 24b). Experimental data again agree well with the calculations performed for both corrected and uncorrected SLM lens. The significant enhancement of the optical performance achieved by the achromatic correction of the SLM is clearly demonstrated by the snapshots in Fig. 24c, taken without and with the refractive corrector.

For higher numerical aperture $NA = 0.06$, the diffraction limit is not reached even with the achromatic correction (Fig. 24b). The decrease in optical performance is caused by the secondary spectrum, whose influence can be reduced by the apochromatic correction. The theoretical concept of the apochromatic correction of the SLM lens was presented in [23], but its realization was not possible in the visible spectral range due to the lack of suitable optical glasses. The required optical glasses are available for the infrared spectral range, where the apochromatic correction is possible. A refractive afocal system providing apochromatic correction of the diffractive dispersion of the SLM lens was designed for Short Wavelength Infrared Region (SWIR). The original design of the system was protected by the Utility model 28818 granted on November 16, 2015. Applications of Czech and European patents were submitted on March 25, 2015 and March 25, 2016, respectively.

## 6.3. Polarization adapted Mirau interferometry with liquid crystal variable retarder

Digital holography and interferometry are well established techniques with multitude of applications in biophotonics, metrology and industry. The significance of these techniques has been further enhanced in recent years due to an extensive use in holographic microscopy. Preferred common-path holographic configurations provide an optimal space-bandwidth product [75], improved stability and system robustness. However, at least three phase-shifted holograms are required for a faithful image reconstruction. The SLM

is frequently used amongst the common-path techniques, which take the advantage of simultaneous phase-shifting and advanced light shaping. Using the SLM and techniques of the Fourier filtering [78–80] or diffractive beam splitting [83,84], the signal and reference waves can be created and the phase-shifting introduced in a standard configuration of the optical microscope. Neither the spatial filtration nor the diffractive beam splitting provide an independent reference wave unaffected by the observed specimen. In the doctoral thesis, a new phase-shifting technique was proposed, suitable for common-path systems working with unaffected reference wave. The method utilizes a polarization adapted Mirau Interference Objective (MIO) and enables a motionless all-optical phase-shifting [21]. The phase-shifting is based on a liquid crystal light modulation and imposed on the unaffected reference wave by the LCVR. During the experiment, linearly polarized illumination beam is divided into the reference and signal wave, having orthogonal linear polarizations at the output of the MIO. The LCVR is operated as a polarization sensitive device, working with a birefringence of liquid crystals molecules and introducing phase retardance between the output waves. The proposed motionless phase-shifting benefits from the polarization adapted MIO, recently invented in [91,92].
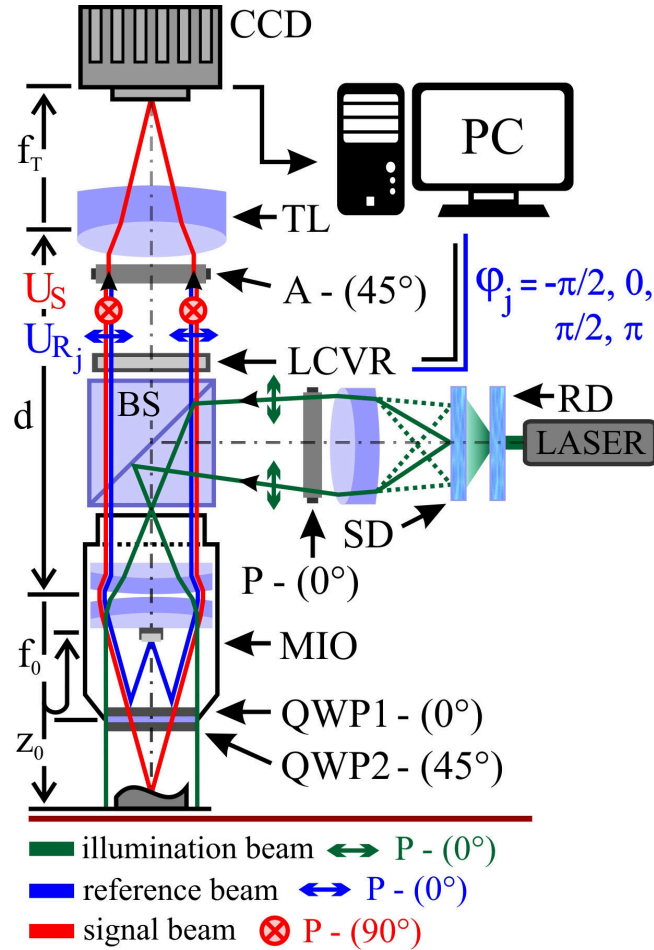


**Figure 25:** Polarization sensitive phase-shifting Mirau interferometer [21]: RD, rotating diffuser; SD, static diffuser; P, linear polarizer; MIO, Mirau interference objective; QWP1 and QWP2, quarter-wave plates; BS, beam splitter; LCVR, liquid crystal variable retarder; A, analyzer; TL, tube lens; CCD, charge coupled device.

The polarization adapted Mirau interferometer working with the motionless all-optical phase-shifting is shown in Fig. 25. In the illumination part, a rotating diffuser RD is placed into the laser beam to reduce the spatial coherence. A static diffuser SD and a polarizer P support the Köhler illumination of the sample by linearly polarized light. The illumination beam is deflected by a beam splitter BS towards the MIO. The MIO is supplemented by a pair of quarter-wave plates, QWP1 and QWP2, placed into the optical paths of the reference and signal wave, respectively. The fast axis of the QWP1 coincides with the polarization direction of the input beam, while the fast axis of the QWP2 is rotated by 45°. After a double passage of the reference wave through the QWP1, the polarization direction is retained. Since the polarization direction of the signal wave is rotated by 90°, after the double passage through the QWP1 and QWP2 and the reflection from the sample, the waves with orthogonal linear polarizations are obtained at the output of the MIO. The orthogonally polarized signal and reference waves then pass through the polarization selective LCVR. The phase-shifting is enabled by anisotropic nematic liquid crystal molecules arranged in uniaxial birefringent layers in the LCVR. With no voltage applied, the liquid crystal molecules lie parallel to glass substrates and maximal retardation between orthogonally polarized waves is achieved. As voltage increases, the orientation of the molecules is changed, causing a reduction in the effective birefringence and phase retardance. In this way, the phase shift between the signal and reference wave can be precisely adjusted. By the analyzer A, the orthogonal linear polarizations are projected into the same direction. It enables interference of the signal and reference waves. By setting analyzer orientation, the intensity of interfering waves can be adjusted to achieve the highest contrast of the interference pattern.

Accuracy of the proposed method is affected by several factors among which phase-shifting errors have the greatest impact. Deviations of the phase-shifting, directly related to LCVR accuracy and throughput stability, were tested both numerically and experimentally. In virtual experiments the signal wave $U_s = A_s \exp(i\Phi_s)$ and reference wave $U_r = A_r \exp(i\Phi_r + i\varphi_j)$ were created and interference patterns $I_j = |U_s + U_r|^2$ obtained. Here, $A_s$, $A_r$ and $\Phi_s$, $\Phi_r$ are the amplitudes and the phases of the signal and reference waves, respectively, and $\varphi_j = (j - 2)\pi/2, j = 1, 2, 3, 4$ denote the constant phase shifts imposed gradually on the reference wave by the LCVR. Applying the four-step phase-shifting, the phase retardance between the signal and reference waves, $\Delta\Phi = \Phi_s - \Phi_r$, was quantitatively reconstructed using the formula

$$\Delta\Phi = \arctan[(I_1 - I_3)/(I_2 - I_4)]. \tag{27}$$

The LCVR errors were simulated by phase reconstructions $\Delta\Phi$, performed while randomly varying throughput of the LCVR and the phase shifts $\varphi_j$ imposed on the reference wave, respectively. Using the experimentally found maximal amplitude deviation $0.05A_r$ and maximal phase ambiguity 0.05 rad, the standard deviation of the reconstructed phase $\sigma = 0.02$ rad was determined from 500 phase reconstructions. It means that inaccuracies of the LCVR allow to obtain a surface profile of the test object with an accuracy better than $\lambda/300$, where $\lambda$ is the wavelength of the used light.

Experimental testing of the polarization adapted MIO was performed in two steps, which were devoted to the phase-shifting reproducibility and accuracy of the phase recovery. To ensure conditions of a high-precision measurement, the setup in Fig. 25 was built at the optical breadboard with a passive vibration isolation and placed on an active damped optical table. To suppress effects of air turbulence and increase a thermal stabil-
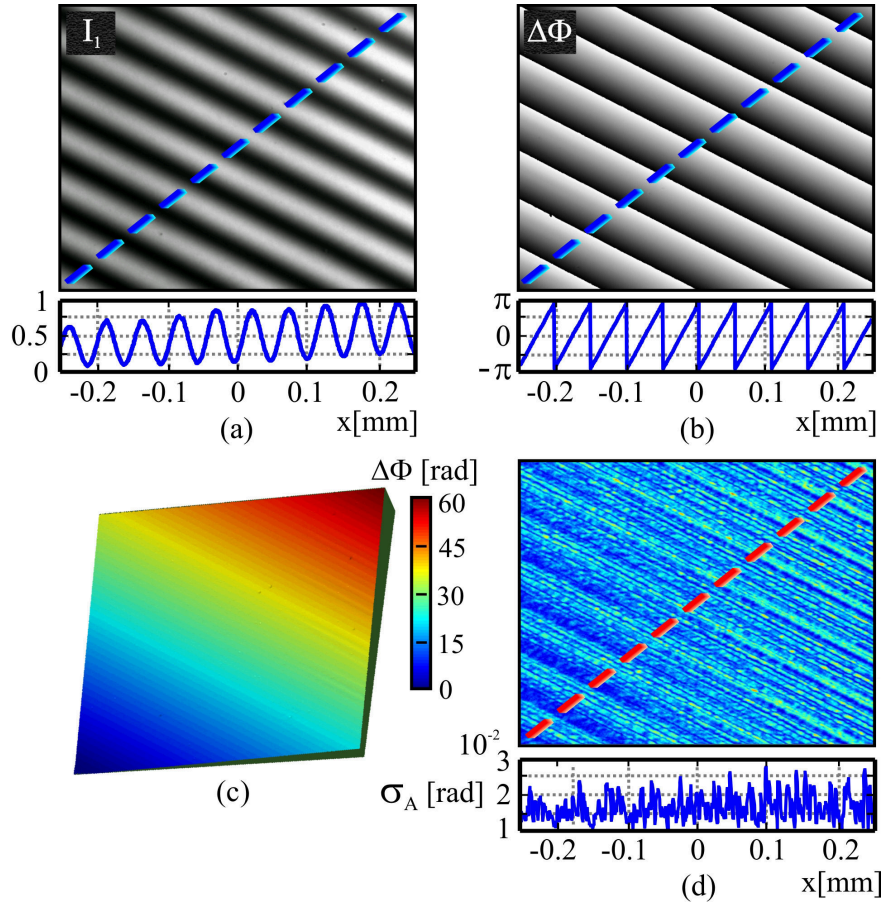
**Figure 26:** Experimental evaluation of the phase-shifting reproducibility performed with a tilted plane mirror [21]: (a) demonstration interferogram $I_1$, (b) wrapped phase, (c) unwrapped phase, (d) standard deviation $\sigma_A$ related to the average phase $\Delta\Phi_A$ (realization of 99 measurements).

ity, the Mirau interferometer was operated in an enclosure system with door assemblies. The polarization version of the MO has been patented [91], but it is still commercially unavailable. Therefore, the standard MIO (Nikon $10 \times /NA = 0.3$) was used and supplemented by the QWP1 providing the required polarization modification. The QWP2 ensuring compensation of optical paths was not mounted to avoid adjustments inside the MIO. For testing of both phase-shifting reproducibility and phase accuracy, a tilted plane mirror introducing a linear phase retardance was used as a sample. In measurements, four interferograms $I_j$ were recorded to apply the phase-shifting procedure. In Fig. 26a, the normalized intensity of the interferogram $I_1$ obtained for $\varphi_1 = -\pi/2$ is shown. The wrapped phase $\Delta\Phi$ and its three dimensional representation after unwrapping are illustrated in Fig. 26b and Fig. 26c, respectively. To obtain statistical data, the measurement was repeated 99 times. From the phase reconstruction carried out in the individual measurements, an average phase $\Delta\Phi_A$ was calculated and used to evaluate the standard deviation $\sigma_A$ over all realizations. The distribution of $\sigma_A$ in the image plane is shown in Fig. 26d. The standard deviation $\sigma_A$ evaluated by the average phase $\Delta\Phi_A$ gives information about the reproducibility of the phase shifts provided by the LCVR. Examining the maxima of $\sigma_A$, accuracy better than $\lambda/250$ was obtained. The absolute accuracy of the proposed technique was assessed using a single phase reconstruction, randomly
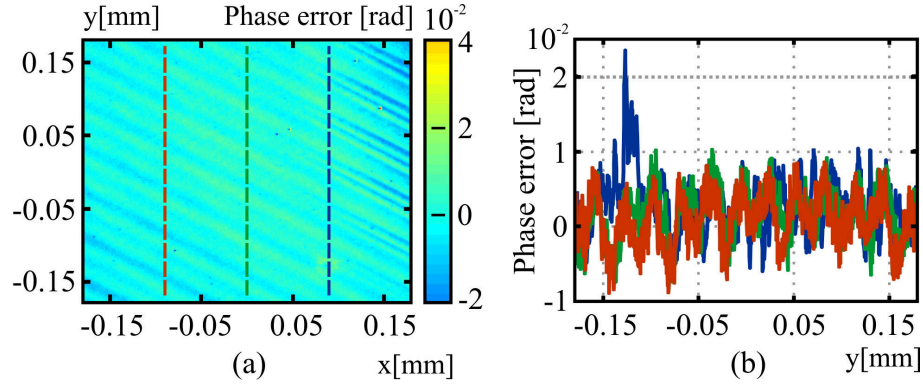
**Figure 27:** Experimental evaluation of the absolute measurement accuracy [21]: (a) the phase errors at individual points of the measured planar surface, (b) the phase errors in indicated sections.

selected from a set of performed measurements. Phase errors at the individual points of the image plane were evaluated with respect to an ideal planar surface, whose inclination was determined by fitting the experimental data (Fig. 27a). Profiles of the phase errors in selected sections are shown in Fig. 27b. The standard deviation was evaluated by
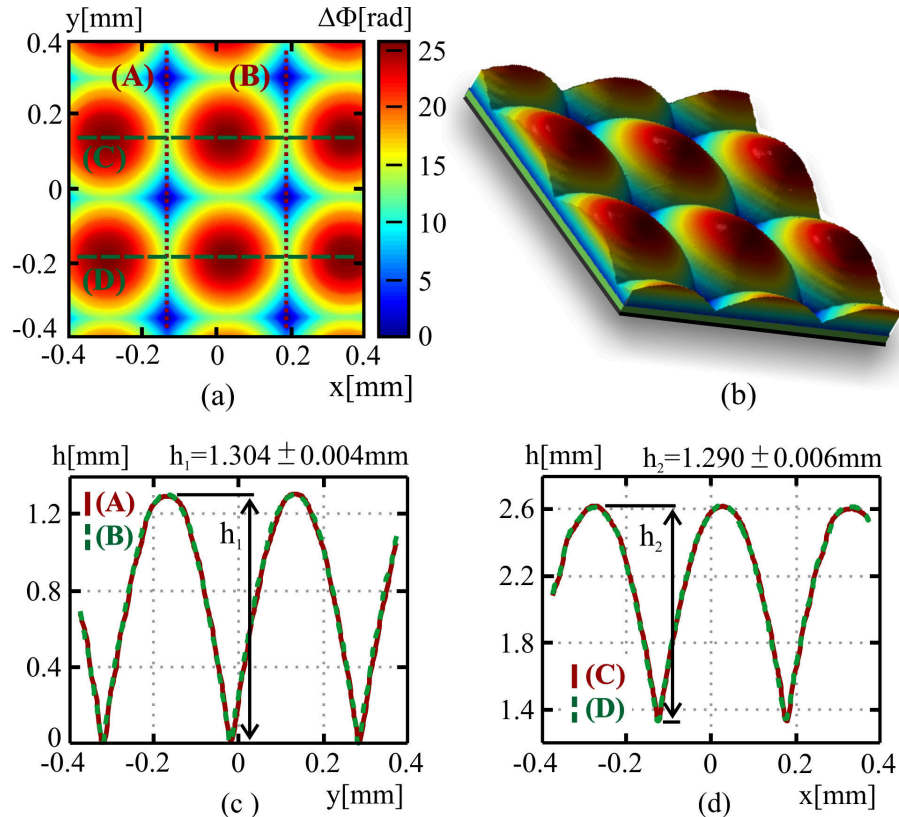


**Figure 28:** Phase reconstruction of the array of microlenses (Thorlabs, MLA 300-14 AR) [21]: (a) unwrapped phase with color representation of the phase levels, (b) 3D illustration of the unwrapped phase, (c) height profiles across the valleys of the microlenses (sections A and B), (d) height profiles across the tops of the microlenses (sections C and D).

processing the phase errors over all pixels of the measured phase surface. Its value was determined as $\sigma = 0.028$ radians, providing the surface profile accuracy of $\lambda/225$ with the peak-to-valley given by $\lambda/43$. The determined accuracy is in a good agreement with the numerical analysis predicting the theoretical precision of $\lambda/300$.

In further experiment, practical applicability of the method was tested and an array of microlenses with parameters provided by the producer was used as a sample (Thorlabs, MLA300-14AR). The experimental results (Fig. 28) were compared with the numerical simulation carried out using the parameters given in the Thorlabs catalog. In the measured array, square plano-convex microlenses with the theoretical focal length $f = 18.6$ mm, the radius of curvature $r = 8.6$ mm and the pitch $p = 300$ $\mu$m were used. By means of $r$ and $p$, the maximal height of the spherical cap along the diagonal of the array was calculated, $h = 2.616$ $\mu$m. The maximal height $h$ is given by the sum of the spherical cap heights $h_1$ and $h_2$ evaluated along the sections A and C in Fig. 28a, $h = h_1 + h_2$. For the theoretical parameters, both heights take the same value, $h_1 = h_2 = 1.308$ $\mu$m. The surface topography obtained by the measurement (Figs. 28a and 28b) was evaluated in sections A, B (Fig. 28c) and C, D (Fig. 28d) taken across the valleys and the tops of the microlenses, respectively. In the statistical assessment of the experimental results, the microlenses available in the field of view of the MIO were used. Evaluating the experimental data, heights of the spherical caps in the sections A, B and C, D were determined as $h_1 = (1.304 \pm 0.004)$ $\mu$m and $h_2 = (1.290 \pm 0.006)$ $\mu$m, respectively. The pitch of the microlenses was measured, $p = (303.6 \pm 0.9)$ $\mu$m. By the best fitting of the experimental data, the radius of curvature of the microlenses $r = 8.68$ mm was determined, which is also close to the value given by the producer.

## 6.4. Multimodal microscope aided by spatial light modulation

In multitude of optical applications, the SLM has been used as a versatile device providing complex and real time shaping of the impinging light. In recent time, a great potential of the SLM aided imaging has been discovered both theoretically and experimentally. In extensive research, the original results have been reached, supporting experiments of optical microscopy, incoherent correlation imaging and digital holographic microscopy. The known methods are based on quite different amplitude, phase and polarization modulation techniques, however their implementation is possible in a unified optical arrangement, provided inventive adjustment of the experimental setup is utilized and variability of the SLM exploited.

In the doctoral thesis, the universal system capable of altering different imaging modes has been developed, which can be advantageously implemented using an add-on module (AOM) connected to a standard optical microscope. The AOM enables unification of the individual imaging modes into the same optical path, resulting in a versatile SLM based multimodal microscope. The designed multimodal microscope combines standard imaging regimes with advanced light shaping techniques and its benefits pave pathways to new applications. The multimodal microscope was accepted as one of the main outputs of the project CDO supported by the TA CR. Utility model of the multimodal microscope will be finalized in 2017.

### 6.4.1. Optical design

Optical design of the multimodal microscope is based on the commercial upright micro-scope Nikon Eclipse E200. Using Nikon accessories, both diascopic and episcopic imaging modes are available. In the diascopic illumination (DI), bright-field imaging was extended by techniques of the Zernike phase contrast and dark-field imaging. For the DI, high-intensity Light Emitting Diode (LED) is utilized radiating in the visible spectral region without infrared radiation. Conditions of the Köhler illumination are ensured using a collector lens supported by fly eye optics and a condenser lens with the numerical aperture $NA = 0.9$. An episcopic illumination (EI) is implemented by a mercury arc lamp placed in
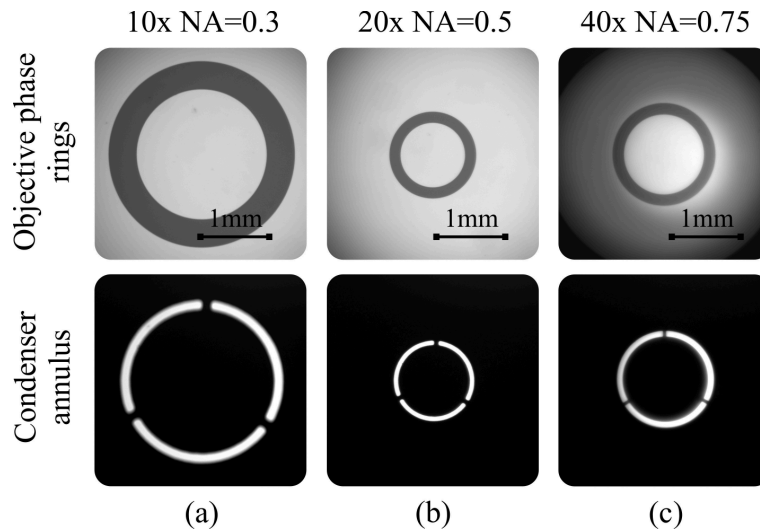


**Figure 29:** Imaging of the phase rings and the condenser annulus on the SLM needed for quantitative phase imaging in the Zernike phase contrast setup. Images corresponding to different types of the MOs: (a) $10 \times /NA = 0.3$, (b) $20 \times /NA = 0.5$ and (c) $40 \times /NA = 0.75$.

the epifluorescence arm. The AOM incorporates amplitude and phase modulation of light and polarization separation of beams required by advanced imaging techniques. It was designed and optimized by the Zemax optical software. Within the AOM, the standard Nikon CFI 60 infinity corrected optics was used. As an optional camera focusing lens, the achromatic doublet Melles Griot was utilized, increasing lateral magnification of the standard microscope Nikon Eclipse E200 by a factor of 1.5.

Conditions needed for an optimal operation of the SLM were carefully considered in the design of the AOM. Connecting the AOM to the optical microscope, the SLM is placed at the Fourier plane, optically conjugate with the condenser diaphragm and the exit pupil of the MO, respectively. It provides a multitude of optical applications including optical filtration, shaping of special beams or advantageous beam splitting. Accessibility of the Fourier plane was tested by optical imaging of the condenser annulus and the phase rings embedded into the condenser and the exit pupil of the MO, respectively, when using setup for the Zernike phase contrast imaging. Images of the phase rings ant the condenser annulus created at the SLM plane are illustrated in Fig. 29a-c for different types of the MOs ($10 \times /NA = 0.3$, $20 \times /NA = 0.5$, $40 \times /NA = 0.75$).

### 6.4.2. Mechanical design

Mechanical construction of the multimodal microscope was designed by Ing. Martin Antoš, Ph.D. Concept of the mechanics was prepared according to the optical design and its requirements were taken into account. In the mechanical construction, commercially available, customized and custom fabricated components were used, providing maximal mounting flexibility of both optical and mechanical elements. It enabled optional adjustment of misaligned parts of the microscope and unification of the optical and mechanical axes. The AOM representing a core of the multimodal microscope is connected to a standard optical microscope via dovetail for a trinocular head. The SLM and CCD are connected to the AOM by two external ports providing a simple positioning and disassembling. For purposes of biological experiments, the microscope is reinforced by a supporting construction, which allows its operation in both upright and inverted regimes. Photographs of multimodal microscope are presented in Figs. 30a-c. Both front and side views (Fig. 30a,b) show DI and EI modules embedded on the body of the microscope Nikon E200. In Fig. 30c, a top view shows the AOM with two external ports equipped by the SLM and CCD, respectively.
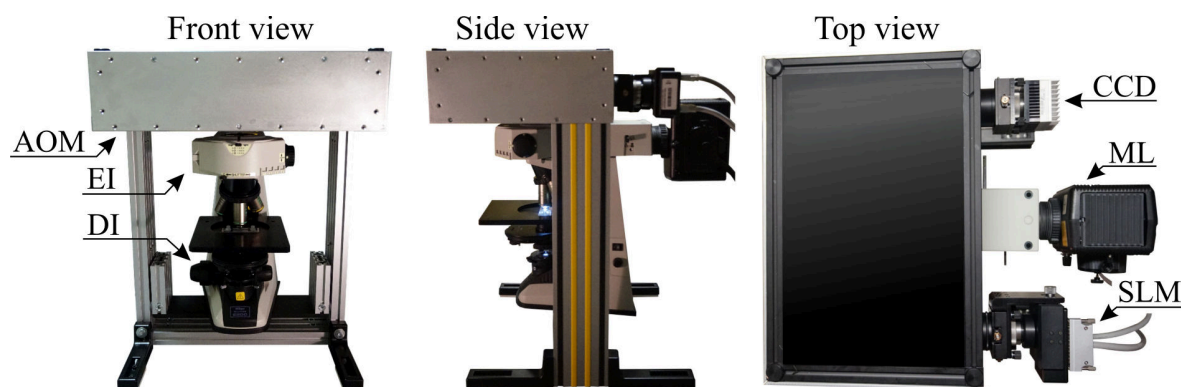


**Figure 30:** Photographs of the multimodal microscope aided by the spatial light modulation: AOM, add-on module; EI, episcopic illumination; DI, diascopic illumination; ML, mercury lamp.
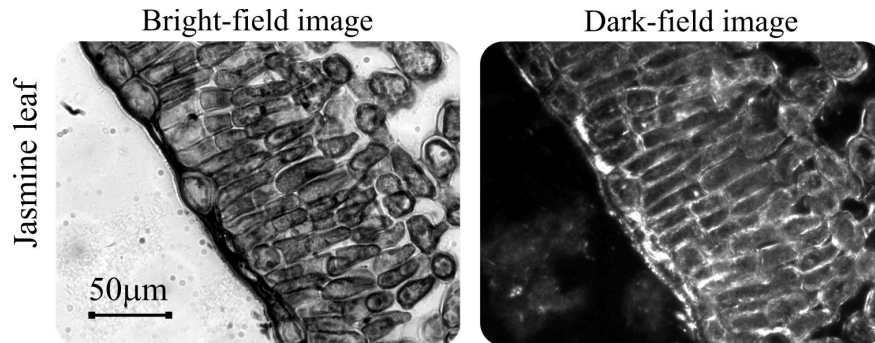
### 6.4.3. Early experimental testing

Although the final completion of the multimodal microscope including control and monitoring functions is scheduled to 2017 within the TA CR project, the system has been functional since 2015. Its operation was examined in the doctoral thesis with the particular attention focused on testing of the compatibility between the AOM and the commercial microscope Nikon Eclipse E200. During performed experiments, both basic and advanced imaging modes were implemented and tested practically. Imaging performance was assessed using different biological specimens and testing objects.

In experiments, the bright-field imaging and Zernike phase contrast and dark-field imaging was implemented with the DI, while epifluorescence imaging was tested using the EI. Results obtained are presented in Figs. 31–33. A comparison of the bright-field and Zernike phase contrast imaging is performed in Figs. 31a,b. Specimens of paramecium were used as a testing sample in Fig. 31a. Images obtained in both bright-field and Zernike phase contrast imaging modes were captured using the MO Nikon $20 \times / NA = 0.5$

Bright-field image    Zernike phase contrast

Paramecium

(a)                   50μm
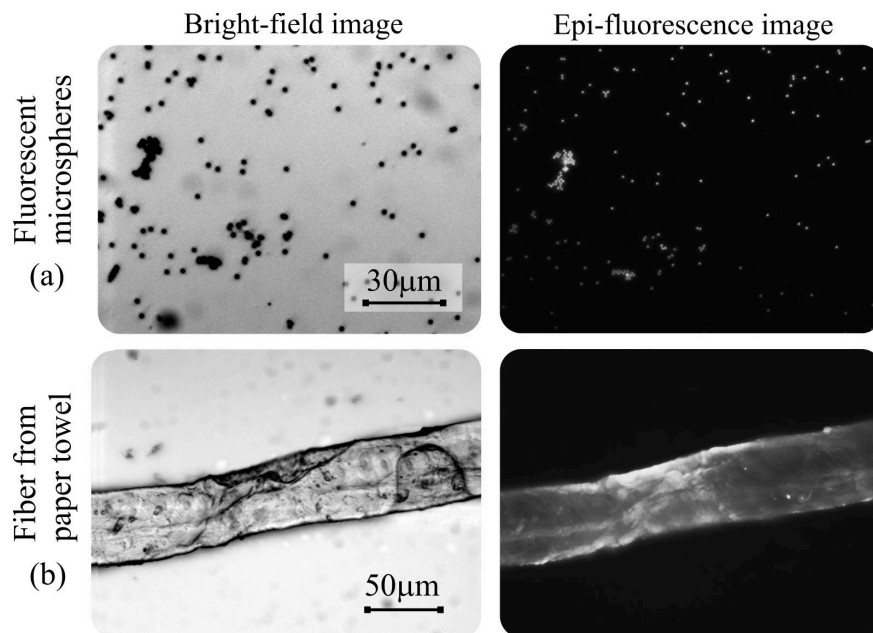
Tobacco leaf

(b)                   300μm
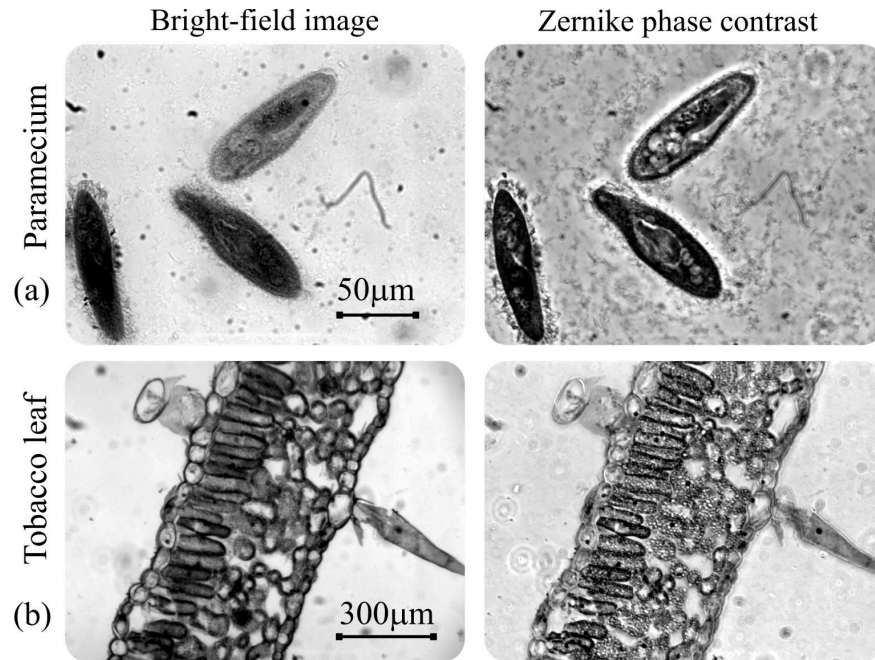
**Figure 31:** Experimental testing of Zernike phase contrast imaging in the multimodal microscope and its comparison with bright-field imaging using (a) paramecium and (b) tobacco leaf as samples.

Bright-field image    Dark-field image

Jasmine leaf

50μm

**Figure 32:** Experimental testing of dark-field imaging in the multimodal microscope and its comparison with bright-field imaging using jasmine leaf as a sample.

($f_0 = 10$ mm). Contrary to the bright-field image, nucleus and vacuoles of paramecium are apparent in the Zernike phase contrast. In Fig. 31b, the MO Nikon $10 \times /NA = 0.3$ ($f_0 = 20$ mm) was utilized and a tobacco leaf used as a sample. Mesophyll cells including their inner structure are observable in the Zernike phase contrast. Both dark-field and epifluorescence imaging was tested utilizing the MO Nikon $20\times$. During the dark-field imaging, a jasmine leaf was used as a sample and its amplitude transitions were successfully enhanced (Fig. 32). In the epifluorescence experiment, fluorescent microspheres (Invitrogen 1 $\mu$m in diameter) were utilized, providing a calibration of imaging system (Fig. 33a). In further experiment, cellulose molecules in fiber from a paper towel were excited and fluorescence image recorded (Fig. 33b).

In advanced experiments, the imaging performance of the multimodal microscope was assessed, using the SLM based methods. During the advanced experimental testing, the methods examined throughout the doctoral thesis were implemented. Beyond the

**Figure 33:** Experimental testing of epifluorescence imaging in the multimodal microscope and its comparison with bright-field imaging using (a) fluorescence microspheres and (b) fiber from paper towel as samples.
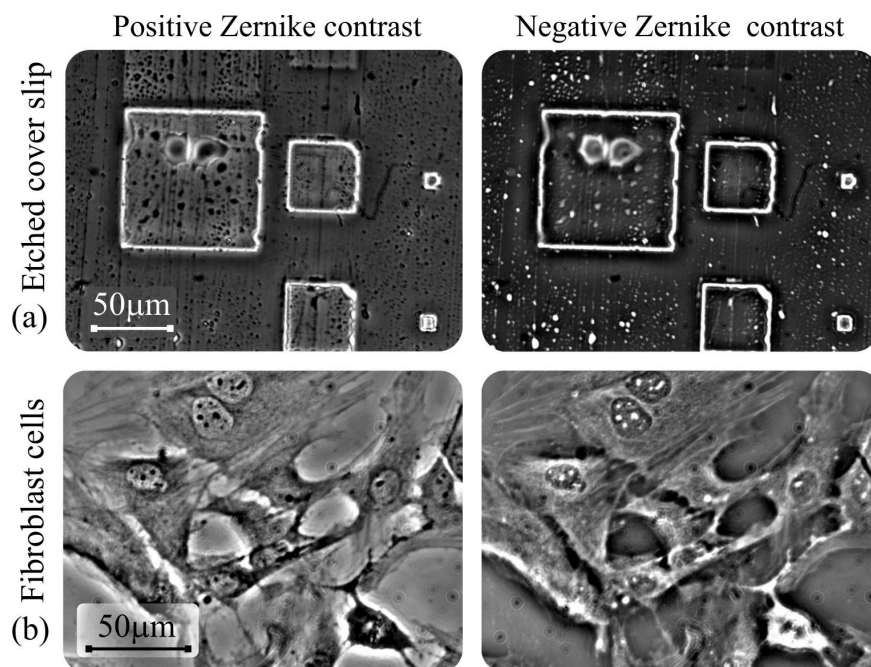


**Figure 34:** Experimental testing of the SLM based positive and negative Zernike phase contrast imaging using etched microscope glass slide and fibroblast cells as samples.

originally proposed methods, also some previously presented experiments on the SLM imaging were successfully reproduced. In particular, adjustable Zernike phase contrast imaging, with potential applicability to the quantitative phase imaging, was implemented [78]. In this imaging modality, the MO phase ring and the condenser annulus (Fig. 29) are projected on the SLM, where the light unaffected by the specimen can be phase-shifted additionally. It provides Zernike images with adjustable phase contrast. The

positive and negative Zernike phase contrast implemented by the SLM is demonstrated in Figs. 34a,b, where images of etched microscope glass slide (Fig. 34a) and fibroblast cells (Fig. 34b) were recorded. Combining benefits of the adjustable Zernike phase contrast and phase-shifting holography, the quantitative phase imaging is possible [78]. During the experimental testing of the quantitative phase imaging, the MO Nikon 20× was utilized and a phase diffraction grating used as a sample. The phase shifted Zernike images of the grating and its quantitative phase reconstruction are presented in Figs. 35a,b. The quantitative phase reconstruction was obtained by processing individual records according to (27). In Fig. 35c, both enlarged subarea of the quantitative phase reconstruction and phase profile perpendicular to grating grooves are shown. Evaluating measured data, the height of grating grooves $h = (335 \pm 7)$ nm was reconstructed. In order to assess obtained results, a reference measurement was performed applying technique of the CCHM [7–10]. During the measurement, the holographic microscope Q-Phase was used. Holographic microscope Q-Phase, developed at the IPE BUT, is currently produced by Tescan Orsay holding, a.s. [114]. Deploying the reference technique, the similar height of grating grooves $h = (324 \pm 6)$ nm was obtained.
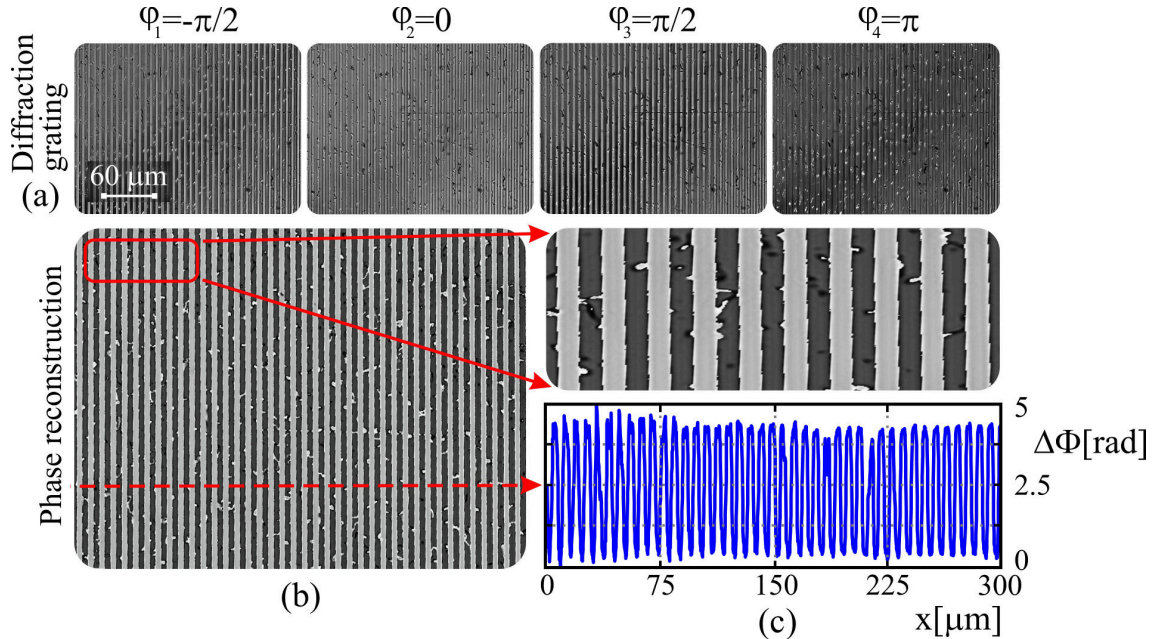


**Figure 35:** Demonstration of quantitative phase imaging in the multimodal microscope. (a) Zernike phase contrast images of diffraction grating with phase shifts $\varphi_j = (j - 2)\pi/2, j = 1, 2, 3, 4$ imposed on light unaffected by the sample. (b) Quantitative phase reconstruction. (c) Enlarged subarea and cross section of quantitative phase reconstruction.

# 7. Conclusion

The doctoral thesis deals with the modern optical imaging methods based on advanced techniques of light shaping and digital signal processing. Throughout the doctoral thesis, principles of optical microscopy, digital holography and incoherent correlation imaging have been systematically studied and the imaging performance of the developed methods enhanced in experiments aided by modern SLM technologies and recent discoveries of singular optics. The research outcomes, presented in both scientific and applied parts of the doctoral thesis, were published in prestigious peer-reviewed journals and contributed to the current state of the art in monitored areas of optics. The results achieved enriched theoretical and experimental know-how available at the IPE BUT and created background for ongoing research activities.

The doctoral thesis is based on theoretical concepts arising from a systematic study of the latest discoveries in the relevant areas of optics, especially in singular, nondiffracting, digital and Fourier optics. The main conceptual aim of the doctoral thesis was to incorporate nontraditional states of light and special optical phenomena into imaging sciences, where they were previously rarely used. The main attention was focused on vortex and nondiffracting light fields and unique self-imaging effects arising from their interference. The theoretical results were validated in experiments carried out using the SLM as a basic experimental tool. The experiments were designed with regard to envisaged applications and their results were used for optimization, enhancement and usability evaluation of the developed methods. The overall significance and impact of the results of the doctoral thesis may be summarized as follows:

- Principles and experiments of the SLM aided imaging were reviewed and original concepts enriching the imaging sciences proposed. In this way, a comprehensive study on novel imaging technologies at the IPE BUT was created.

- Through the results of the doctoral thesis new research program was outlined and adopted at IPE BUT, which was successfully incorporated into the projects of basic and applied research supported by the GA CR and TA CR.

- Research within the doctoral thesis and the project funding provided theoretical and experimental background at the IPE BUT, enabling cutting-edge experiments on the SLM aided imaging.

- The particular results of the doctoral thesis were exploited in the design of the multimodal microscope, in which specific imaging modes have been incorporated including fluorescence correlation imaging, spiral imaging, Zernike phase contrast imaging, quantitative phase reconstruction and three-dimensional localization and tracking of microobjects. Utility model of the multimodal microscope was intended as one of the objectives of the TA CR project.

The doctoral thesis is divided into three distinctive parts. In the introductory part, its contents is discussed in the context of relevant areas of optics. Modern imaging methods, mainly based on light shaping techniques, principles of holography and digital data processing, are summarized in a detailed review, revealing attractive areas of further research promising for original results. Subsequently, wider circumstances of the research are discussed with emphasis on the theoretical background and experimental facilities available.

The main results of the doctoral thesis, consisting of outcomes of both basic and applied research, are presented in the separate parts.

Activities of basic research are presented in scientific part of the doctoral thesis. The main effort was focused on methods of the correlation and holographic imaging combining the spatial light modulation with the digital processing of acquired data. The incoherent correlation imaging was described in fundamental models working with spatially incoherent monochromatic light [13] and broadband light [14]. In general models of the broadband correlation imaging, effects of reduced temporal coherence were examined, resulting in the concept of coherence induced aperture [14,15]. Analyzing the coherence aperture, new experimental configurations were found, optimizing the incoherent correlation imaging for broadband light. In experiments of broadband imaging, the problems caused by a very strong diffractive dispersion of the SLM were revealed, which initiated further research focused on the compensation of undesirable chromatic aberrations [23]. A significant part of the research has been devoted to light vortices and especially their use in advanced imaging methods. Vortex interference effects previously utilized in the spiral microscopy were successfully deployed in methods of the incoherent correlation imaging, digital holography and optical microscopy. By using optically and digitally implemented vortex fields, the anisotropic edge contrast enhancement of three-dimensional samples was achieved in the correlation imaging working with incoherent light [16]. In advanced experiments of the incoherent correlation imaging and digital holography, nondiffracting vortex beams were utilized for the DH PSF engineering and the precise axial localization of microscopic objects [17,18]. Research of rotating self-imaging effects caused by interference of light vortices resulted into the experiments providing a robust aberration resistant axial localization. It was successfully implemented in optical microscopy aided by the SLM [19,20]. Techniques of localization and tracking of microobjects were further developed in experiments, where light vortices were generated by special spiral masks mounted in the microscope objective. In these experiments, the expensive SLM was omitted and localization of particles was possible in the standard configuration of the optical microscope, while improving energy efficiency. The spiral wave plates providing a complex amplitude-phase modulation were custom fabricated at the ISI Brno and tested experimentally at the IPE BUT laboratory.

Outcomes of applied research are presented in the part of the doctoral thesis devoted to design and technical improvement of developed experiments and optical systems. In the framework of applied research, new experimental configurations were proposed and implementation of the spatial light modulation was optimized. Relay optical system was deployed in the correlation experiments, where both the achievable field of view and the image resolution were significantly improved [22]. In broadband light imaging applications, diffractive dispersion of the SLM was effectively reduced using the afocal refractive corrector [23]. Its operational principle emerged from the results of the doctoral thesis and was optimized in continuing cooperation with the optical designers from the UP. The original design of the corrector has been protected by the utility model and also the Czech and European patents have been submitted in 2015 and 2016, respectively. New phase-shifting technique was demonstrated in the polarization adapted Mirau interferometry working with the birefringent computer driven LCVR. Theoretical and experimental know-how acquired in the doctoral thesis resulted in the design of the SLM based multimodal microscope. Within the multimodal microscope, basic imaging regimes and

advanced methods of the SLM aided imaging were successfully tested at the IPE BUT laboratory.

# Abbreviations

**AOM** Add-On Module 54

**CCD** Charge-Coupled Device 16

**CCHM** Coherence Controlled Holographic Microscopy 1

**CDO** Center of Digital Optics 1

**CGH** Computer Generated Hologram 8

**CR** Correlation Record 29

**DH PSF** Double-Helix Point Spread Function 11

**DI** Diascopic Illumination 55

**EI** Episcopic Illumination 55

**GA CR** Grant Agency of the Czech Republic 1

**IF** Impact Factor 4

**IPE BUT** Institute of Physical Engineering Brno University of Technology 1

**ISI Brno** Institute of Scientific Instruments Brno 4

**iSLIM** instantaneous Spatial Light Interference Microscopy 11

**LCVR** Liquid Crystal Variable Retarder 4

**LED** Light Emitting Diode 55

**MIO** Mirau Interference Objective 50

**MMDM** Micromachined Membrane Deformable Mirror 7

**MO** Microscope Objective 16

**MTF** Modulation Transfer Function 49

**PDM** Piezoelectric Deformable Mirror 7

**PSF** Point Spread Function 3

**QWP** Quarter-Wave Plate 50

**SCR** Spiral Correlation Record 29

**SLIM** Spatial Light Interference Microscopy 11

**SLM** Spatial Light Modulator 1

**STED** Stimulated Emission Depletion 10

**SWIR** Short Wavelength Infrared Region 49

**SWP** Spiral Wave Plate 42

**TA CR** Technology Agency of the Czech Republic 1

**UP** Palacky University 1

# References

[1] DURNIN, J. *Exact solutions for nondiffracting beams. I. The scalar theory.* J. Opt. Soc. Am. A **4**, 651–654, (1987).

[2] MONTGOMERY, W. D. *Self–Imaging Objects of Infinite Aperture.* J. Opt. Soc. Am. **57**, 772–775, (1967).

[3] PATORSKI, K. *The self–imaging phenomenon and its applications.* Progress in Optics **27**, E. Wolf, ed., North–Holland, Amsterdam, (1990).

[4] SOSKIN, M. S.; VASNETSOV, M.V. *Singular Optics.* Progress in Optics **42**, 219–276, (2001).

[5] BOUCHAL, P. *Bachelor thesis: Fresnelova nekoherentní korelační holografie (FINCH).* Brno: Brno University of Technology, Faculty of Mechanical Engineering, 1–41, (2010).

[6] BOUCHAL, P. *Diploma thesis: Fresnelova nekoherentní korelační holografie (FINCH).* Brno: Brno University of Technology, Faculty of Mechanical Engineering, 1–63, (2012).

[7] CHMELÍK, R.; SLABÝ, T.; KOLMAN, P.; DOSTÁL, Z.; ANTOŠ, M. *Interferometric system with spatial carrier frequency capable of imaging in polychromatic radiation.* Brno: Brno University of Technology, U.S. Patent 8526003 B2, (2013).

[8] KOLMAN, P.; CHMELÍK, R. *Coherence-controlled holographic microscope.* Opt. Exp. **18**, 21990–22003, (2010).

[9] SLABÝ, T.; KOLMAN, P.; DOSTÁL, Z.; ANTOŠ, M.; LOŠŤÁK, M.; CHMELÍK, R. *Off-axis setup taking full advantage of incoherent illumination in coherence-controlled holographic microscope.* Opt. Exp. **21**, 14747–14762, (2013).

[10] LOŠŤÁK, M.; CHMELÍK, R.; SLABÁ, M.; SLABÝ, T. *Coherence-controlled holographic microscopy in diffuse media.* Opt. Exp, **22**, 4180–4195, (2014).

[11] BOUCHAL, P.; BOUCHAL, Z.; CHMELÍK, R. *Jednocestná nekoherentní korelační mikroskopie: metody, aplikace a výzkum v Centru digitální optiky TA ČR.* Jemná mechanika a optika, č. 6–7, 184–186, (2014).

[12] BOUCHAL, Z.; BOUCHAL, P. *Optické víry aneb jak roztočit světlo.* Československý časopis pro fyziku, **65**, 351–354, (2016).

[13] BOUCHAL, P.; KAPITÁN, J.; CHMELÍK, R.; BOUCHAL, Z. *Point spread function and two–point resolution in Fresnel incoherent correlation holography.* Opt. Exp. **19**, 15603–15620, (2011).

[14] BOUCHAL, P.; BOUCHAL, Z. *Concept of coherence aperture and pathways toward white light high–resolution correlation imaging.* New. J. Phys. **15**, 1–18, (2013).

[15] BOUCHAL, P.; BOUCHAL, Z.; CHMELÍK, R. *Resolution Limits in Broadband Incoherent Correlation Imaging.* Digital Holography and 3D Imaging, OSA Technical Digest (online), paper DW2A.17, (2013).

[16] BOUCHAL, P.; BOUCHAL, Z. *Selective edge enhancement in three–dimensional vortex imaging with incoherent light.* Opt. Lett. **37**, 2949–2951, (2012).

[17] BOUCHAL, P.; BOUCHAL, Z.; CHMELÍK, R. *Incoherent digital holography with axial localization by the rotating point spread function.* Imaging and Applied Optics, OSA Technical Digest (online), paper DM2B.4, (2014).

[18] BOUCHAL, P.; BOUCHAL, Z. *Non–iterative holographic axial localization using complex amplitude of diffraction–free vortices.* Opt. Exp. **22**, 30200–30216, (2014).

[19] BARÁNEK, M.; BOUCHAL, P.; BOUCHAL, Z. *Self-imaging of optical vortices for 3D localization and wavefront assessment.* Digital Holography and Three-Dimensional Imaging, OSA Technical Digest (online), paper DW2A. 12, (2015).

[20] BARÁNEK, M.; BOUCHAL, P.; ŠILER, M.; BOUCHAL, Z. *Aberration resistant axial localization using a self–imaging of vortices.* Opt. Exp. **23**, 15316–15331, (2015).

[21] BOUCHAL, P.; ČELECHOVSKÝ, R.; BOUCHAL, Z. *Polarization sensitive phase-shifting Mirau interferometry using a liquid crystal variable retarder.* Opt. Lett. **40**, 4567–4570, (2015).

[22] BOUCHAL, P.; BOUCHAL, Z. *Wide–field common–path incoherent correlation microscopy with a perfect overlapping of interfering beams.* JEOS:RP. **8**, 1–8, (2013).

[23] BOUCHAL, Z.; CHLUP, V.; ČELECHOVSKÝ, R.; BOUCHAL, P.; NISTOR, C. *Achromatic correction of diffractive dispersion in white light SLM imaging.* Opt. Exp **22**, 12046–12059, (2014).

[24] BOUCHAL, P.; BOUCHAL, Z.; ČELECHOVSKÝ, R.; BARÁNEK, M. *Svazek1: Využití prostorového modulátoru světla v optickém zobrazení.* Research report, Center of Digital Optics TA CR, 1–60, (2013).

[25] CHLUP, V.; BOUCHAL, Z.; BOUCHAL, P. *Afokální optický systém pro korekci barevné vady difraktivních zobrazovacích prvků.* Utility model 28818, Office of industrial property, Czech Republic (2016), Application of Czech and European patent (submitted in 2015 and 2016).

[26] Department of Optics, Palacky University Olomouc. Source: *http://www.ldo.optol.cz/cs/* [online]. 25.8.2015 (cited 2015–08–25).

[27] Flexible Optical B.V. OKO Tech. Source: *http://www.okotech.com/pdm* [online]. 13.9.2015 (cited 2015–09–13).

[28] Flexible Optical B.V. OKO Tech. Source: *http://www.okotech.com/mmdm* [online]. 13.9.2015 (cited 2015–09–13).

[29] Thorlabs Inc. Source: *http://www.thorlabs.de/NewGroupPage9.cfm?ObjectGroup_ID=6339* [online]. 27.8.2015 (cited 2015–08–27).

[30] Flexible Optical B.V. OKO Tech. Source: *http://www.okotech.com/lc* [online]. 13.4.2015 (cited 2015–04–13).

[31] HOLOEYE Photonis AG. Source: *http://holoeye.com/spatial–light–modulators/* [online]. 13.4.2015 (cited 2015–04–13).

[32] Hamamatsu Photonics. Source: *http://www.hamamatsu.com/jp/en/4015.html* [online]. 13.4.2015 (cited 2015–04–13).

[33] ARCoptix. FT IR Spectrometers & Liquid Crystal Elements. Source:*http://www.arcoptix.com/variable_phase_retarder* [online]. 13.4.2015 (cited 2015–04–13).

[34] NEIL, M.; JUSKAITIS, R.; WILSON, T. *Method of obtaining optical sectioning by using structured light in a conventional microscope.* Opt. Lett. **22**, 1905–1907, (1997).

[35] NEIL, M.; SQUIRE, A.; JUSIKAITIS, R.; BASTIAENS, P.; WILSON, T. *Wide-field optically sectioning fluorescence microscopy with laser illumination.* Journal of Microscopy, **197**, 1–4, (2000).

[36] BOZINOVIC, N.; VENTALON, C.; FORD, T.; MERTZ, J. *Fluorescence endomicroscopy with structured illumination.* Opt. Exp. **16**, 8016–8025, (2008).

[37] HUISKEN, J.; SWOGER, J.; DEL BENE, F.; WITTBRODT, J.; STELYER, H. *Optical sectioning deep inside live embryos by selective plane illumination microscopy.* Science, **305**, 1007–1009, (2004).

[38] FAHRBACH, F. O.; ROHRBACH, A. *A line scanned light-sheet microscope with phase shaped self-reconstructing beams.* Opt. Exp. **18**, 24229–24244, (2010).

[39] FAHRBACH, F. O.; SIMON, P.; ROHRBACH A. *Microscopy with self-reconstructing beams.* Nat. Photonics **4**, 780–785, (2010).

[40] PLANCHON T. A.; GAO, L.; MILKIE, D. E.; DAVIDSON, M. W.; GALBRAITH, J. A.; GALBRAITH, C. G.; BETZIG, E. *Rapid three-dimensional isotropic imaging of living cells using Bessel beam plane illumination.* Nat. Methods **8**, 417–423, (2011).

[41] VETTENBURG, T.; DALGARNO, H.; NYLK, J.; COLL-LLADÓ, C.; FERRIER, D.; ČIŽMÁR, T.; GUNN-MOORE, F.; DHOLAKIA, K. *Light–sheet microscopy using an Airy beam.* Nature Methods **11**, 541–544, (2014).

[42] DALGARNO, H.; ČIŽMÁR, T.; VETTENBURG, T.; NYLK, J.; GUNN–MOORE, F.; DHOLAKIA, K. *Wavefront corrected light sheet microscopy in turbid media.* Appl. Phys. Lett. **100**, 191108, (2012).

[43] GUSTAFSSON, M. *Surpassing the lateral resolution limit by a factor of two using structured illumination microscopy.* Journal of Microscopy **198**, 82–87, (2000).

[44] FIOLKA, R.; BECK, M.; STEMMER, A. *Structured illumination in total internal reflection fluorescence microscopy using a spatial light modulator.* Opt. Lett. **33**, 1629–1631, (2008).

[45] LIISA, M.; HIRVONEN, M.; WICKER, K.; MANDULA, O.; HEINTZMANN, R. *Structured illumination microscopy of a living cell.* Eur. Biophys. J. **38**, 807–812, (2009).

[46] HELL, S.; WICHMANN, J. *Breaking the diffraction resolution limit by stimulated emission: Stimulated–emission–depletion fluorescence microscopy.* Opt. Lett. **19**, 780–782, (1994).

[47] RUST, M.; BATES. M; ZHUANG, X. *Sub–diffraction–limit imaging by stochastic optical reconstruction microscopy (STORM).* Nature Methods **10**, 793–796, (2006).

[48] BETZIG, E.; PATTERSON, G. H.; SOUGRAT, R.; LINDWASSER, O. W.; OLENYCH, S.; BONIFACINO, J. S.; DAVIDSON, M. W.; LIPPINCOTT–SCHWARTZ, J.; HESS, H. F. *Imaging Intracellular Fluorescent Proteins at Nanometer Resolution.* Science **313**, 1642–1645, (2006).

[49] About Nobelprize.org., Nobel Media AB 2014. Source: *http://www.nobelprize.org/nobel_organizations/nobelmedia/nobelprize_org/* [online] 1.9.2015 (cited 2015–09–01).

[50] GOULD, T.; BURKE, D.; BEWERSDORF, J.; BOOTH, M. *Adaptive optics enables 3D STED microscopy in aberrating specimens.*, Opt. Exp. **20**, 20998–21009, (2012).

[51] MICÓ, V.; ZALEVSKY, Z.; GARCÍA, J. *Superresolved common–path phase–shifting digital inline holographic microscopy using a spatial light modulator.*, Opt. Lett. **37**, 4988–4990, (2012).

[52] GAO, P.; PEDRINI, G.; OSTEN, W. *Structured illumination for resolution enhancement and autofocusing in digital holographic microscopy.* Opt. Lett. **38**, 1328–1330, (2013).

[53] HUSSAIN, A.; MARTÍNEZ, J.; CAMPOS, J. *Holographic super-resolution using spatial light modulator.* JEOS:RP. **8**, 1–6, (2013).

[54] ASHKIN, A.; DZIEDZIC, J.; BJORKHOLM, J.; CHU, S. *Observation of a single–beam gradient force optical trap for dielectric particles.* Opt. Lett. **11**, 288–290, (1986).

[55] CURTIS, J.; KOSS, B.; GRIER, D. *Dynamic holographic optical tweezers.* Opt. Commun. **207**, 169–175, (2002).

[56] ČIŽMÁR, T.; KOLLÁROVÁ, V; TSAMPOULA, F.; GUNN-MOORE, F.; SIBBETT, W.; BOUCHAL, Z.; DHOLAKIA, K. *Generation of multiple Bessel beams for a biophotonics workstation.* Opt. Exp. **16**, 14024–14035, (2008).

[57] ČIŽMÁR, T.; KOLLÁROVÁ, V.; BOUCHAL, Z.; ZEMÁNEK, P. *Sub–micron particle organization by self–imaging of non–diffracting beams.* New. J. Phys. **8**, 1–24, (2006).

[58] GARCES-CHAVEZ, V.; MELVILLE, H.; SIBBETT, W.; DHOLAKIA, K. *Simultaneous micromanipulation in multiple planes using a self-reconstructing light beam.* Nature **419**, 145–147, (2002).

[59] WARBE, M.; MAIER, S.; HAIST, T.; OSTEN, W. *Combination of scene–based and stochastic measurement for wide–field aberration correction in microscopic imaging.* Appl. Opt. **49**, 5474–5479, (2010).

[60] ZWICK, S.; WARBER, M.; GORSKI, W.; HAIST, T.; OSTEN, W. *Flexible Adaptive Phase Contrast Methods Using a Spatial Light Modulator.* DGaO Proc., 1614–8436, (2009).

[61] MAURER, C.; JESACHER, A.; BERNET, S.; MARTE, M. *What spatial light modulators can do for optical microscopy.* Laser Photonics Rev. **5**, 81–101, (2011).

[62] LEE, M. P.; GIBSON, G. M.; BOWMAN, R.; BERNET, S.; MARTE, M.; PHILLIPS, D. B.; PADGETT, M. J. *A multi-modal stereo microscope based on a spatial light modulator.* Opt. Exp. **21**, 16541–16551, (2013).

[63] FÜRHAPTER, S.; JESACHER, A.; BERNET, S.; MARTE, M. *Spiral phase contrast imaging in microscopy.* Opt. Exp. **13**, 689–694, (2005).

[64] SHARMA, M.; JOSEPH, J.; SENTHILKUMARAN, P. *Selective edge enhancement using anisotropic vortex filter.* Appl. Opt. **50**, 5279–5286, (2011).

[65] SITU, G.; PEDRINI, G.; OSTEN, W. *Spiral phase filtering and orientation–selective edge detection/enhancement.* J. Opt. Soc. Am. A **26**, 1788–1797, (2009).

[66] JESACHER, A.; FÜRHAPTER, S.; BERNET, S.; MARTE, M. *Shadow Effects in Spiral Phase Contrast Microscopy.* Phys. Rev. Lett. **94**, 233902, (2005).

[67] BERNET, S.; JESACHER, A.; FÜRHAPTER, S.; MAURER, C.; MARTE, M. *Quantitative imaging of complex samples by spiral phase contrast microscope.* Opt. Exp. **14**, 3792–3805, (2006).

[68] SNOEYINK, C. *Imaging performance of Bessel beam microscopy.* Opt. Lett. **38**, 2550–2553, (2013).

[69] GREENGARD, A.; SCHECHNER, Y.; PIESTUN, R. *Depth from diffracted rotation.* Opt. Lett. **31**, 181–183, (2006).

[70] PAVANI, S.; PIESTUN, R. *High–efficiency rotating point spread functions.* Opt. Exp. **16**, 3484–3489, (2008).

[71] BARÁNEK, M.; BOUCHAL, Z. *Rotating vortex imaging implemented by a quantized spiral phase modulation.* JEOS–RP **8**, 1–8, (2013).

[72] PRASAD, S. *Rotating point spread function via pupil-phase engineering.* Opt. Lett. **38**, 585–587, (2013).

[73] ROIDER, C.; JESACHER, A.; BERNET, S.; MARTE, M. *Axial super–localisation using rotating point spread functions shaped by polarisation–dependent phase modulation.* Opt. Exp. **22**, 4029–4037, (2014).

[74] LEE, H.; SAHL, S.; LEW, M.; MOERNER, W. *The double–helix microscope super–resolves extended biological structures by localizing single blinking molecules in three dimensions with nanoscale precision.* Appl. Phys. Lett. **100**, 153701, (2012).

[75] XU, L.; PENG, X.; GUO, Z.; MIAO, J.; ASUNDI, A. *Imaging analysis of digital holography.* Opt. Express **13**, 2444–2452, (2005).

[76] YAMAGUCHI, I.; ZHANG, T. *Phase–shifting digital holography.* Opt. Lett. **22**, 1268–1270, (1997).

[77] YAMAUCHI, M.; ELJU, T. *Phase modulation capability of thin twisted nematic liquid crystal panels at double-pass configurations.* Opt. Review **2**, 24–27, (1995).

[78] WANG, Z.; MILLET, L.; MIR, M.; DING, H.; UNARUNOTAI, S.; ROGERS, J.; GILLETE, M.; POPESCU, G. *Spatial light interference microscopy (SLIM).* Opt. Exp. **19**, 1016–1026, (2011).

[79] DING, H.; POPESCU, G. *Instantaneous spatial light interference microscopy.* Opt. Exp. **18**, 1569–1575, (2010).

[80] MICÓ, V.; GARCÍA, J.; ZALEVSKY, Z.; JAVIDI, B. *Phase–shifting Gabor holography.* Opt. Lett. **34**, 1492–1494, (2009).

[81] MEDECKI, H.; TEJNIL, E.; GOLDBERG, K.; BOKOR, J. *Phase–shifting point diffraction interferometer.* Opt. Lett. **21**, 1526–1528, (1996).

[82] BAKER, K.; STAPPAERTS, E. *A single–shot pixellated phase–shifting interferometer utilizing a liquid–crystal spatial light modulator.* Opt. Lett. **31**, 733–735, (2006).

[83] MICÓ, V.; GARCÍA, J. *Common–path phase–shifting lensless holographic microscopy.* Opt. Lett. **35**, 3919–3921, (2010).

[84] ROSEN, J.; BROOKER, G. *Digital spatially incoherent Fresnel holography.* Opt. Lett. **32**, 912–914, (2007).

[85] BROOKER, G.; SIEGEL, N.; WANG, V.; ROSEN, J. *Optimal resolution in Fresnel incoherent correlation holographic fluorescence microscopy.* Opt. Exp. **19**, 5047–5062, (2011).

[86] ROSEN, J.; BROOKER, G. *Fluorescence incoherent color holography.* Opt. Exp. **15**, 2244–2250, (2007).

[87] ROSEN, J.; SIEGEL, N.; BROOKER, G. *Theoretical and experimental demonstration of resolution beyond the Rayleigh limit by FINCH fluorescence microscopic imaging.* Opt. Exp. **19**, 26249–26268, (2011).

[88] KATZ, B.; ROSEN, J.; KELNER, R.; BROOKER, G. *Enhanced resolution and throughput of Fresnel incoherent correlation holography (FINCH) using dual diffractive lenses on a spatial light modulator (SLM).* Opt. Exp. **20**, 9109–9121, (2012).

[89] LAI, X.; ZHAO, Y.; LV, X.; ZHOU, Z.; ZENG, S. *Fluorescence holography with improved signal to noise ratio by near image plane recording.* Opt. Lett. **37**, 2445–2447, (2012).

[90] JAING CH. CH; SHIE, Y. L.; TANG, Ch. J.; LIOU, Y. Y.; CHANG, CH.M.; YANG, CH. R. *Determination of displacement with a piezoelectric transducer using phase-shift algorithms.* Opt. Review **16**, 170–172, (2009).

[91] SCHMIT, J.; HARIHARAN, P. *Polarization mirau interference microscope.* U.S. Patent 8072610 B1 (2011).

[92] TAPILUOW, A. M.; CHEN, L. CH.; JEN, Y. J.; LIN, S. T.; YEH, S.L. *Orthogonal polarization Mirau interferometer using reflective-type waveplate.* Opt. Lett. 38, 2502–2504, (2013).

[93] BITOU, Y. *Digital phase-shifting interferometer with an electrically addressed liquid-crystal spatial light modulator.* Opt. Lett. **28**, 1576–1578, (2003).

[94] SCHILLING, B. W; POON, T. C.; INDEBETOUW, G.; STORRIE, B.; SHINODA, K.; SUZUKI, Y.; WU, M. H. *Three-dimensional holographic fluorescence microscopy.* Opt. Lett. **22**, 1506–1508, (1997).

[95] SHAKED, N. T.; KATZ, B.; ROSEN, J. *Review of three-dimensional holographic imaging by multiple-viewpoint-projection based methods.* Appl. Opt. **48**, 120–136, (2009).

[96] KATZ, B.; WULICH, D.; ROSEN, J. *Optimal noise suppression in Fresnel incoherent correlation holography (FINCH) configured for maximum imaging resolution.* Appl. Opt. **49**, 5757–5763, (2010).

[97] LAI, X.; ZENG, S.; LV, X.; YUAN, J.; FU, L. *Violation of the Lagrange invariant in an optical imaging system.* Opt. Lett. **38**, 1896–1898, (2013).

[98] ROSEN, J.; KELNER, R. *Modified Lagrange invariants and their role in determining transverse and axial imaging resolutions of self-interference incoherent holographic systems.* Opt. Exp. **22**, 29048–29066, (2014).

[99] DING, Z.; REN, H.; ZHAO, Y.; NELSON, J. S.; CHEN, Z. *High-resolution optical coherence tomography over a large depth range with an axicon lens.* Opt. Lett. **27**, 243–245, (2002).

[100] FORTIN, M.; PICHÉ, M.; BORRA, E. *Optical tests with Bessel beam interferometry.* Opt. Exp. **12**, 5887–5895, (2004).

[101] BITEEN, J.; GOLEY, E.; SHAPIRO, L.; MOERNER, W. E. *Three-Dimensional Super-Resolution Imaging of the Midplane Protein FtsZ in Live Caulobacter crescentus Cells Using Astigmatism.* ChemPhysChem. **13**, 1007–1012, (2012).

[102] SHENG, J.; MALKIEL, E.; KATZ, J. *Using digital holographic microscopy for simultaneous measurements of 3D near wall velocity and wall shear stress in a turbulent boundary layer.* Experiments in Fluids **45**, 1023, (2008).

[103] KAO, H.; VERKMAN, A. *Tracking of single fluorescent particles in three dimensions: use of cylindrical optics to encode particle position.* Biophys. J. **67**, 1291–1300, (1994).

[104] HOLTZER, L.; MECKEL, T.; SCHMIDT, T. *Nanometric three-dimensional tracking of individual quantum dots in cells.* Appl. Phys. Lett. **90**, 053902, (2007).

[105] YU, X.; HONG, J.; LIU, Ch.; KIM, M. *Review of digital holographic microscopy for three–dimensional profiling and tracking.* Opt. Eng. **53**, 1–21, (2014).

[106] CHOI, Y.; LEE, S. *Three-dimensional volumetric measurement of red blood cell motion using digital holographic microscopy.* Appl. Opt. **48**, 2983–2990, (2009).

[107] DUBOIS, F.; SCHOCKAERT, C.; CALLENS, N.; YOURASSOWSKY C. *Focus plane detection criteria in digital holography microscopy by amplitude analysis.* Opt. Exp. **14**, 5895–5908, (2006).

[108] LATYCHEVSKAIA, T.; GEHRI, F.; FINK, H. *Depth-resolved holographic reconstructions by three-dimensional deconvolution.* Opt. Exp. **18**, 22527–22544, (2010).

[109] GIRE, J.; DENIS, L.; FOURNIER, C.; THIEBAUT, E.; SOULEZ, F.; DUCOTTET, C. *Digital holography of particles: benefits of the "inverse problem" approach".* Meas. Sci. Technol. **19**, 074005, (2008).

[110] SOULEZ F.; DENIS, L.; FOURNIE, C.; THIEBAUT, E.; GOEPFERT, C. *Inverse problem approach for particle digital holography: accurate location based on local optimisation.* J. Opt. Soc. Am. A, **24**, 1164–1171, (2007).

[111] GHOSH, S.; PREZA, CH. *Characterization of a three–dimensional double–helix point spread function for fluorescence microscopy in the presence of spherical aberration.* J. Biomed. Opt. **18**, 1–11, (2013).

[112] BERNET, S.; JESACHER, A.; FÜRHAPTER, S.; MAURER, C.; Marte, M. *Quantitative imaging of complex samples by spiral phase contrast microscopy.* Opt. Exp. **14**, 3792–3805, (2006).

[113] STEIGER, R.; BERNET, S.; MARTE, M. *SLM–based off–axis Fourier filtering in microscopy with white light illumination.* Opt. Exp. **20**, 15377–15384, (2012).

[114] TESCAN ORSAY HOLDING, a.s. Source: *http://www.tescan.com/en/products/q-phase/q-phase* [online]. 25.12.2015 (cited 2015–12–25).